

FLORIDA STATE UNIVERSITY  
COLLEGE OF ARTS AND SCIENCES

A DALITZ PLOT ANALYSIS AND  
EXTRACTION OF  
SPIN DENSITY MATRIX ELEMENTS  
FOR THE  $\omega \rightarrow 3\pi$  DECAY

By

CHRISTOPHER ZEOLI

A Dissertation submitted to the  
Department of Physics  
in partial fulfillment of the  
requirements for the degree of  
Doctor of Philosophy

2016

Christopher Zeoli defended this dissertation on Oct 18, 2016.  
The members of the supervisory committee were:

Volker Credé  
Professor Directing Dissertation

Philip Sura  
University Representative

Paul Eugenio  
Committee Member

Winston Roberts  
Committee Member

Todd Adams  
Committee Member

The Graduate School has verified and approved the above-named committee members, and certifies that the dissertation has been approved in accordance with university requirements.

# ACKNOWLEDGMENTS

As with most if not all good things I have earned in my life, I would be neither where I am nor who I am today were it not for the value and humor taken and invested in me by a great number of talented, generous, and kind individuals along the way. Through my military service with a tour overseas to the completion of my coursework, projects, and degrees to date, my non-traditional journey has often challenged and tried my perseverance. Without regret, however, my experience overall has been fulfilling and fruitful. It is with great pleasure and honor that I may use this opportunity to share my gratitude for those who encouraged, supported, helped, pushed, and cheered for me along the way in my successful pursuit of a Physics PhD.

I would like to thank my wife Kari Lynn who has been by my side through thick and thin, endless days and sleepless nights, as I hammered out this dissertation and gave its successful defense. Your unwavering love, support, patience, and forgiveness has set the highest of standards to which I may never match, yet I look forward to trying. I love you and thank you.

Thank you also to my two sets of parents, both Paul and Mary as well as Margie and Bill, who raised me to view the world as my oyster: to grab life by the horns when able and to seek serenity and peace of mind in nature's beauty and grandeur when not. Thank you to my third set of parents, my in-laws, Buddy and Lynn, for their gracious love and generous support of both Kari and I both before and after we became newlyweds. Thank you also to my brothers and sisters, grandma Betty, extended family, friends, and those who have passed (the siblings for which are too great in number all by themselves to mention by name here). Each and all of you have been a blessing for which I am eternally grateful.

My major professor Dr. Volker Credé has been a strong source of encouragement, clarity of reasoning, and motivation throughout my research. He has been gracious in both time and commitment to my development in both the areas of scientific research and computation. Thank you for making me part of your team. Also, I appreciate the time, discussions, and assistance from each and all of my other committee members. Thank you Drs. Paul Eugenio, Winston Roberts, Todd Adams, and Philip Sura.

A special thank you to Nabuo Sato who during his graduate studies here at Florida State University spent a great deal of time teaching me many of the computational basics which I have

relied heavily upon every since. Thank you to my colleague Priyashree Roy for often lending her ear and being a constant source of encouragement to the daily ups and downs of research. Thank you to my colleague Zulkaida Akbar for the many discussions we had regarding data reconstruction, event selection, and kinematic fitting and cuts used to prepare our data for my analysis. Lastly, thank you to all of the graduate students and researchers, many of whom I have cited in this dissertation, for your work and dissertations previous to mine on the CLAS-g12 and CLAS-g8b experiments.

# TABLE OF CONTENTS

List of Tables . . . . .	vii
List of Figures . . . . .	viii
Abstract . . . . .	xiv
<b>1 Introduction</b>	<b>1</b>
1.1 Summary . . . . .	1
1.2 The Standard Model . . . . .	2
1.3 Confinement and Quantum Chromodynamics . . . . .	5
1.4 Symmetries, Groups, and Spectroscopic Notation . . . . .	9
1.5 Resonance Decays and Analysis Motivation . . . . .	13
1.6 Partial Wave Analysis . . . . .	13
1.7 The Dalitz Plot Distribution . . . . .	14
1.8 The Experiment and Data . . . . .	20
<b>2 The CLAS-g12 Experiment</b>	<b>23</b>
2.1 The Experiment Facilities . . . . .	23
2.2 The Accelerator . . . . .	24
2.3 Photon Tagging System . . . . .	26
2.4 The Detector . . . . .	28
2.4.1 Target . . . . .	28
2.4.2 Start Counter . . . . .	30
2.4.3 Drift Chambers . . . . .	30
2.4.4 Toroidal Magnet . . . . .	31
2.4.5 Time of Flight Counter . . . . .	32
2.4.6 The ST and TOF . . . . .	33
2.4.7 The CC and EC . . . . .	33
2.4.8 Run Conditions . . . . .	34
<b>3 The CLAS-g12 Data &amp; Event Reconstruction</b>	<b>35</b>
3.1 The Data Acquisition System & Triggers . . . . .	35
3.2 Track and Event Vertex Reconstruction . . . . .	36
3.3 Particle Identification . . . . .	37
<b>4 Event Selection, Kinematic Fitting, Cuts, &amp; The Q-Value Method</b>	<b>38</b>
4.1 Final-State Event Selection . . . . .	38
4.2 Kinematic Fitting . . . . .	38
4.3 Photon Selection and Kinematic Cuts . . . . .	40
4.4 The Q-Value Method . . . . .	42
4.5 Detector Efficiency Simulation and Data Acceptance Correction . . . . .	45

<b>5</b>	<b>Partial Wave Analysis</b>	<b>48</b>
5.1	The Intensity Distribution . . . . .	49
5.1.1	Rest Frame Helicity States . . . . .	50
5.1.2	The Decay Amplitude . . . . .	54
5.1.3	The Production Amplitude . . . . .	55
5.1.4	The Full Intensity and SDMEs . . . . .	57
5.2	Schilling's Equation and Spin Density Matrix Elements . . . . .	60
5.3	The Differential Production Cross Section . . . . .	63
5.4	The Decay Model . . . . .	65
<b>6</b>	<b>Fit Procedure and Results</b>	<b>71</b>
6.1	Fit Framework . . . . .	71
6.1.1	Setting Up AmpTools . . . . .	71
6.1.2	Framework Additions . . . . .	75
6.2	Fit Method . . . . .	77
6.2.1	Fit Quality and Fitter Consistency Checks . . . . .	79
6.3	Fit Functions . . . . .	80
6.4	Results . . . . .	82
6.4.1	CLAS-g12 SDMEs . . . . .	84
6.4.2	CLAS-g8b SDMEs . . . . .	90
6.4.3	CLAS-g12 JPAC $\omega \rightarrow 3\pi$ Decay Parameter . . . . .	90
6.4.4	CLAS-g8b JPAC $\omega \rightarrow 3\pi$ Decay Parameter . . . . .	108
<b>7</b>	<b>Conclusion</b>	<b>120</b>
7.1	Conclusion . . . . .	120
7.2	Future Prospects . . . . .	122
	References . . . . .	123
	Biographical Sketch . . . . .	128

# LIST OF TABLES

1.1	Meson Spectroscopic Notation, $I^G J^{PC}$ . . . . .	12
1.2	Spectroscopic notation values for $\gamma p \rightarrow p \omega \rightarrow p 3\pi$ . . . . .	12
1.3	CLAS-g12 and CLAS-g8b data sample event counts . . . . .	22
2.1	Run conditions for the CLAS-g12 and CLAS-g8b experiments . . . . .	34

# LIST OF FIGURES

1.1	The Standard Model of Particle Physics (Image Source: [16]) . . . . .	3
1.2	Hadrons, quark composite baryons and mesons, respectively represented with colorless color-charge combinations (Image Source: [22]) . . . . .	5
1.3	The strong coupling constant, $\alpha_s(Q)$ , as a function of momentum transfer, $Q^2$ , with the scaling parameter, $\Lambda_{QCD} = M_z$ , chosen as the Z boson mass [24] . . . . .	7
1.4	A Dalitz plot expressed in terms of final state particle-pair masses and with illustrated kinematic boundaries [8] . . . . .	16
1.5	A symmetric representation of the Dalitz plot expressed either in (dimensionless) $x$ and $y$ or polar $r$ and $\theta$ variables (Image Source: [36]) . . . . .	16
1.6	Predicted Dalitz plot vanishing regions from the Zemach formalism [38] . . . . .	19
1.7	A Dalitz plot expressed in terms of dimensionless $x$ and $y$ variables using CLAS-g12 (signal) data for $W$ : [1770 – 2840] MeV . . . . .	19
1.8	The (background separated) $\omega$ mass, $M_\omega$ , distribution from CLAS-g12 data for $W$ : [1770 – 2840] MeV . . . . .	21
1.9	The (background separated) $\omega$ mass, $M_\omega$ , distribution from CLAS-g8b data for $W$ : [1770 – 2340] MeV . . . . .	21
2.1	An aerial view of CEBAF and its detector halls (2014) [39] . . . . .	24
2.2	A schematic diagram of CEBAF and its detector halls post the 12 GeV upgrades [41] . . . . .	24
2.3	A 5 cell cryostat cavity [43] . . . . .	25
2.4	A schematic illustration of the RF controlled induced dipole across a 5 cell cryostat cavity [44] . . . . .	25
2.5	A schematic diagram of Hall B with the Photon Tagging System (upper-left) shown upstream from the target and center of CLAS [45] . . . . .	27
2.6	A schematic diagram of CLAS Photon Tagging System [46] . . . . .	27
2.7	A schematic diagram of the CLAS detector [39] . . . . .	29
2.8	A 2D cross section sketch of the CLAS detector [46] . . . . .	29
2.9	Schematic diagram of the CLAS-g12 (g8b, g11a) target [48] . . . . .	30
2.10	Schematic diagram of the CLAS start counter [49] . . . . .	30

2.11	A schematic cross section diagram of the field and sense wires within a drift chamber [46]	31
2.12	The CLAS toroidal magnet during the assembly of CLAS [51]	32
4.1	Helicity and Adair frame comparison	43
5.1	Schematic diagram of the Euler angles (Image Source: [64])	52
5.2	g11, g12 $\gamma p \rightarrow p\omega$ Differential Cross Sections, $E_\gamma \in [1.55 - 2.55]$ MeV, Refs. [1, 7]	64
5.3	Isobar decomposition [3]	66
5.4	Crossed channel rescattering effects [3]	66
5.5	A reduced Dalitz plot distribution, $DP(x, y)/\phi$ , comparison between the CLAS-g12 acceptance corrected (signal) data versus JPAC modelled distributions for various chosen JPAC $\omega \rightarrow 3\pi$ decay parameter values. The decay distribution factor $\phi$ , given in Eqn. 5.71, is divided out for the purpose of visualizing the effects of the JPAC distribution alone. The JPAC $\omega \rightarrow 3\pi$ decay parameter was expected to be about +8, i.e. $a_{JPAC}^{\omega \rightarrow 3\pi} \sim +8$ [65]	70
6.1	A schema of my partial-wave analysis framework	72
6.2	g12, g11a SDME comparison for $W : [1900 - 1910]$ MeV and $\cos(\theta_{cm}^\omega) : [-1.0 - 1.0]$ at widths of 0.1	85
6.3	g12, g11a SDME comparison for $W : [2000 - 2010]$ MeV and $\cos(\theta_{cm}^\omega) : [-1.0 - 1.0]$ at widths of 0.1	85
6.4	g12, g11a SDME comparison for $W : [2100 - 2110]$ MeV and $\cos(\theta_{cm}^\omega) : [-1.0 - 1.0]$ at widths of 0.1	86
6.5	g12, g11a SDME comparison for $W : [2200 - 2210]$ MeV and $\cos(\theta_{cm}^\omega) : [-1.0 - 1.0]$ at widths of 0.1	86
6.6	g12, g11a SDME comparison for $W : [2300 - 2310]$ MeV and $\cos(\theta_{cm}^\omega) : [-1.0 - 1.0]$ at widths of 0.1	87
6.7	g12, g11a SDME comparison for $W : [2400 - 2410]$ MeV and $\cos(\theta_{cm}^\omega) : [-1.0 - 1.0]$ at widths of 0.1	87
6.8	g12, g11a SDME comparison for $W : [2500 - 2510]$ MeV and $\cos(\theta_{cm}^\omega) : [-1.0 - 1.0]$ at widths of 0.1	88
6.9	g12, g11a SDME comparison for $W : [2620 - 2630]$ MeV and $\cos(\theta_{cm}^\omega) : [-1.0 - 1.0]$ at widths of 0.1	88
6.10	g12, g11a SDME comparison for $W : [2700 - 2710]$ MeV and $\cos(\theta_{cm}^\omega) : [-1.0 - 1.0]$ at widths of 0.1	89

6.11	g12, g11a SDME comparison for $W : [2800 - 2810]$ MeV and $\cos(\theta_{cm}^\omega) : [-1.0 - 1.0]$ at widths of 0.1 . . . . .	89
6.12	g8b, g11a SDME comparison for $W : [1900 - 1950]$ MeV and $\cos(\theta_{cm}^\omega) : [-1.0 - 1.0]$ at widths of 0.1 . . . . .	91
6.13	g8b, g11a SDME comparison for $W : [2000 - 2050]$ MeV and $\cos(\theta_{cm}^\omega) : [-1.0 - 1.0]$ at widths of 0.1 . . . . .	91
6.14	g8b, g11a SDME comparison for $W : [2100 - 2150]$ MeV and $\cos(\theta_{cm}^\omega) : [-1.0 - 1.0]$ at widths of 0.1 . . . . .	92
6.15	g8b, g11a SDME comparison for $W : [2200 - 2250]$ MeV and $\cos(\theta_{cm}^\omega) : [-1.0 - 1.0]$ at widths of 0.1 . . . . .	92
6.16	JPAC $\omega \rightarrow 3\pi$ decay parameter, $a_{JPAC}^{\omega \rightarrow 3\pi}$ , fitted to CLAS-g12 data for $W : [1770 - 2840]$ MeV at widths of 10 MeV. The boundary factor used was $\lambda$ , Eqn. 4.6 . . . . .	95
6.17	JPAC $\omega \rightarrow 3\pi$ decay parameter, $a_{JPAC}^{\omega \rightarrow 3\pi}$ , fitted to CLAS-g12 data for $W : [2000 - 2500]$ MeV at widths of 10 MeV. The boundary factor used was $\lambda$ , Eqn. 4.6 . . . . .	95
6.18	JPAC $\omega \rightarrow 3\pi$ decay parameter, $a_{JPAC}^{\omega \rightarrow 3\pi}$ , fitted to CLAS-g12 data for $W : [1770 - 2840]$ MeV at widths of 10 MeV. The boundary factor used was $\phi_{physical}$ , Eqn. 6.13 . . . . .	96
6.19	JPAC $\omega \rightarrow 3\pi$ decay parameter, $a_{JPAC}^{\omega \rightarrow 3\pi}$ , fitted to CLAS-g12 data for $W : [2000 - 2500]$ MeV at widths of 10 MeV. The boundary factor used was $\phi_{physical}$ , Eqn. 6.13 . . . . .	96
6.20	JPAC $\omega \rightarrow 3\pi$ decay parameter, $a_{JPAC}^{\omega \rightarrow 3\pi}$ , fitted to CLAS-g12 data for $E_\gamma : [1700 - 1800]$ MeV and $t : [0.100 - 3.100]$ GeV <sup>2</sup> at widths of 0.100 GeV <sup>2</sup> . The boundary factor used was $\lambda$ , Eqn. 4.6 . . . . .	97
6.21	JPAC $\omega \rightarrow 3\pi$ decay parameter, $a_{JPAC}^{\omega \rightarrow 3\pi}$ , fitted to CLAS-g12 data for $E_\gamma : [1900 - 2000]$ MeV and $t : [0.100 - 3.100]$ GeV <sup>2</sup> at widths of 0.100 GeV <sup>2</sup> . The boundary factor used was $\lambda$ , Eqn. 4.6 . . . . .	97
6.22	JPAC $\omega \rightarrow 3\pi$ decay parameter, $a_{JPAC}^{\omega \rightarrow 3\pi}$ , fitted to CLAS-g12 data for $E_\gamma : [2100 - 2200]$ MeV and $t : [0.100 - 3.100]$ GeV <sup>2</sup> at widths of 0.100 GeV <sup>2</sup> . The boundary factor used was $\lambda$ , Eqn. 4.6 . . . . .	98
6.23	JPAC $\omega \rightarrow 3\pi$ decay parameter, $a_{JPAC}^{\omega \rightarrow 3\pi}$ , fitted to CLAS-g12 data for $E_\gamma : [2300 - 2400]$ MeV and $t : [0.100 - 3.100]$ GeV <sup>2</sup> at widths of 0.100 GeV <sup>2</sup> . The boundary factor used was $\lambda$ , Eqn. 4.6 . . . . .	98
6.24	JPAC $\omega \rightarrow 3\pi$ decay parameter, $a_{JPAC}^{\omega \rightarrow 3\pi}$ , fitted to CLAS-g12 data for $W : [2000 - 2100]$ MeV and $M_\omega : [740 - 820]$ MeV at widths of 10 MeV. The boundary factor used was $\phi_{physical}$ , Eqn. 6.13 . . . . .	99

6.25	JPAC $\omega \rightarrow 3\pi$ decay parameter, $a_{JPAC}^{\omega \rightarrow 3\pi}$ , fitted to CLAS-g12 data for $W : [2000 - 2100]$ MeV and $M_\omega : [740 - 820]$ MeV at widths of 5 MeV. The boundary factor used was $\phi_{physical}$ , Eqn. 6.13 . . . . .	99
6.26	JPAC $\omega \rightarrow 3\pi$ decay parameter, $a_{JPAC}^{\omega \rightarrow 3\pi}$ , fitted to CLAS-g12 data for $W : [2100 - 2200]$ MeV and $M_\omega : [740 - 820]$ MeV at widths of 10 MeV. The boundary factor used was $\phi_{physical}$ , Eqn. 6.13 . . . . .	100
6.27	JPAC $\omega \rightarrow 3\pi$ decay parameter, $a_{JPAC}^{\omega \rightarrow 3\pi}$ , fitted to CLAS-g12 data for $W : [2100 - 2200]$ MeV and $M_\omega : [740 - 820]$ MeV at widths of 5 MeV. The boundary factor used was $\phi_{physical}$ , Eqn. 6.13 . . . . .	100
6.28	JPAC $\omega \rightarrow 3\pi$ decay parameter, $a_{JPAC}^{\omega \rightarrow 3\pi}$ , fitted to CLAS-g12 data for $W : [2200 - 2300]$ MeV and $M_\omega : [740 - 820]$ MeV at widths of 10 MeV. The boundary factor used was $\phi_{physical}$ , Eqn. 6.13 . . . . .	101
6.29	JPAC $\omega \rightarrow 3\pi$ decay parameter, $a_{JPAC}^{\omega \rightarrow 3\pi}$ , fitted to CLAS-g12 data for $W : [2200 - 2300]$ MeV and $M_\omega : [740 - 820]$ MeV at widths of 5 MeV. The boundary factor used was $\phi_{physical}$ , Eqn. 6.13 . . . . .	101
6.30	JPAC $\omega \rightarrow 3\pi$ decay parameter, $a_{JPAC}^{\omega \rightarrow 3\pi}$ , fitted to CLAS-g12 data for $W : [2300 - 2400]$ MeV and $M_\omega : [740 - 820]$ MeV at widths of 10 MeV. The boundary factor used was $\phi_{physical}$ , Eqn. 6.13 . . . . .	102
6.31	JPAC $\omega \rightarrow 3\pi$ decay parameter, $a_{JPAC}^{\omega \rightarrow 3\pi}$ , fitted to CLAS-g12 data for $W : [2300 - 2400]$ MeV and $M_\omega : [740 - 820]$ MeV at widths of 5 MeV. The boundary factor used was $\phi_{physical}$ , Eqn. 6.13 . . . . .	102
6.32	JPAC $\omega \rightarrow 3\pi$ decay parameter, $a_{JPAC}^{\omega \rightarrow 3\pi}$ , fitted to CLAS-g12 data for $W : [2400 - 2500]$ MeV and $M_\omega : [740 - 820]$ MeV at widths of 10 MeV. The boundary factor used was $\phi_{physical}$ , Eqn. 6.13 . . . . .	103
6.33	JPAC $\omega \rightarrow 3\pi$ decay parameter, $a_{JPAC}^{\omega \rightarrow 3\pi}$ , fitted to CLAS-g12 data for $W : [2400 - 2500]$ MeV and $M_\omega : [740 - 820]$ MeV at widths of 5 MeV. The boundary factor used was $\phi_{physical}$ , Eqn. 6.13 . . . . .	103
6.34	JPAC $\omega \rightarrow 3\pi$ decay parameter, $a_{JPAC}^{\omega \rightarrow 3\pi}$ , fitted to CLAS-g12 data for $W : [2000 - 2500]$ MeV at widths of 10 MeV with no cuts about $M_\omega$ . The boundary factor used was $\phi_{physical}$ , Eqn. 6.13 . . . . .	104
6.35	JPAC $\omega \rightarrow 3\pi$ decay parameter, $a_{JPAC}^{\omega \rightarrow 3\pi}$ , fitted to CLAS-g12 data for $W : [2000 - 2500]$ MeV at widths of 10 MeV, $M_\omega \pm 40$ MeV. The boundary factor used was $\phi_{physical}$ , Eqn. 6.13 . . . . .	104
6.36	JPAC $\omega \rightarrow 3\pi$ decay parameter, $a_{JPAC}^{\omega \rightarrow 3\pi}$ , fitted to CLAS-g12 data for $W : [2000 - 2500]$ MeV at widths of 10 MeV, $M_\omega \pm 30$ MeV. The boundary factor used was $\phi_{physical}$ , Eqn. 6.13 . . . . .	105

6.37	JPAC $\omega \rightarrow 3\pi$ decay parameter, $a_{JPAC}^{\omega \rightarrow 3\pi}$ , fitted to CLAS-g12 data for $W : [2000 - 2500]$ MeV at widths of 10 MeV, $M_\omega \pm 20$ MeV. The boundary factor used was $\phi_{physical}$ , Eqn. 6.13 . . . . .	105
6.38	JPAC $\omega \rightarrow 3\pi$ decay parameter, $a_{JPAC}^{\omega \rightarrow 3\pi}$ , fitted to CLAS-g12 data for $W : [2000 - 2500]$ MeV at widths of 10 MeV, $M_\omega \pm 15$ MeV. The boundary factor used was $\phi_{physical}$ , Eqn. 6.13 . . . . .	106
6.39	JPAC $\omega \rightarrow 3\pi$ decay parameter, $a_{JPAC}^{\omega \rightarrow 3\pi}$ , fitted to CLAS-g12 data for $W : [2000 - 2500]$ MeV at widths of 10 MeV, $M_\omega \pm 10$ MeV. The boundary factor used was $\phi_{physical}$ , Eqn. 6.13 . . . . .	106
6.40	JPAC $\omega \rightarrow 3\pi$ decay parameter, $a_{JPAC}^{\omega \rightarrow 3\pi}$ , fitted to CLAS-g12 data for $W : [2000 - 2500]$ MeV at widths of 10 MeV, $M_\omega \pm 5.0$ MeV. The boundary factor used was $\phi_{physical}$ , Eqn. 6.13 . . . . .	107
6.41	JPAC $\omega \rightarrow 3\pi$ decay parameter, $a_{JPAC}^{\omega \rightarrow 3\pi}$ , fitted to CLAS-g12 data for $W : [2000 - 2500]$ MeV at widths of 10 MeV, $M_\omega \pm 2.0$ MeV. The boundary factor used was $\phi_{physical}$ , Eqn. 6.13 . . . . .	107
6.42	JPAC $\omega \rightarrow 3\pi$ decay parameter, $a_{JPAC}^{\omega \rightarrow 3\pi}$ , fitted to CLAS-g8b data for $W : [1770 - 2340]$ MeV at widths of 10 MeV. The boundary factor used was $\phi_{physical}$ , Eqn. 6.13 . . . . .	110
6.43	JPAC $\omega \rightarrow 3\pi$ decay parameter, $a_{JPAC}^{\omega \rightarrow 3\pi}$ , fitted to CLAS-g8b data for $W : [1900 - 2340]$ MeV at widths of 10 MeV. The boundary factor used was $\phi_{physical}$ , Eqn. 6.13 . . . . .	110
6.44	JPAC $\omega \rightarrow 3\pi$ decay parameter, $a_{JPAC}^{\omega \rightarrow 3\pi}$ , fitted to CLAS-g8b data for $E_\gamma : [1700 - 1800]$ MeV and $t : [0.100 - 3.100]$ GeV <sup>2</sup> at widths of 0.100 GeV <sup>2</sup> . The boundary factor used was $\lambda$ , Eqn. 4.6 . . . . .	111
6.45	JPAC $\omega \rightarrow 3\pi$ decay parameter, $a_{JPAC}^{\omega \rightarrow 3\pi}$ , fitted to CLAS-g8b data for $E_\gamma : [1900 - 2000]$ MeV and $t : [0.100 - 3.100]$ GeV <sup>2</sup> at widths of 0.100 GeV <sup>2</sup> . The boundary factor used was $\lambda$ , Eqn. 4.6 . . . . .	111
6.46	JPAC $\omega \rightarrow 3\pi$ decay parameter, $a_{JPAC}^{\omega \rightarrow 3\pi}$ , fitted to CLAS-g8b data for $E_\gamma : [2100 - 2200]$ MeV and $t : [0.100 - 3.100]$ GeV <sup>2</sup> at widths of 0.100 GeV <sup>2</sup> . The boundary factor used was $\lambda$ , Eqn. 4.6 . . . . .	112
6.47	JPAC $\omega \rightarrow 3\pi$ decay parameter, $a_{JPAC}^{\omega \rightarrow 3\pi}$ , fitted to CLAS-g8b data for $E_\gamma : [2300 - 2400]$ MeV and $t : [0.100 - 3.100]$ GeV <sup>2</sup> at widths of 0.100 GeV <sup>2</sup> . The boundary factor used was $\lambda$ , Eqn. 4.6 . . . . .	112
6.48	JPAC $\omega \rightarrow 3\pi$ decay parameter, $a_{JPAC}^{\omega \rightarrow 3\pi}$ , fitted to CLAS-g8b data for $W : [2000 - 2100]$ MeV and $M_\omega : [740 - 820]$ MeV at widths of 10 MeV. The boundary factor used was $\phi_{physical}$ , Eqn. 6.13 . . . . .	113

6.49	JPAC $\omega \rightarrow 3\pi$ decay parameter, $a_{JPAC}^{\omega \rightarrow 3\pi}$ , fitted to CLAS-g8b data for $W : [2000 - 2100]$ MeV and $M_\omega : [740 - 820]$ MeV at widths of 5 MeV. The boundary factor used was $\phi_{physical}$ , Eqn. 6.13 . . . . .	113
6.50	JPAC $\omega \rightarrow 3\pi$ decay parameter, $a_{JPAC}^{\omega \rightarrow 3\pi}$ , fitted to CLAS-g8b data for $W : [2100 - 2200]$ MeV and $M_\omega : [740 - 820]$ MeV at widths of 10 MeV. The boundary factor used was $\phi_{physical}$ , Eqn. 6.13 . . . . .	114
6.51	JPAC $\omega \rightarrow 3\pi$ decay parameter, $a_{JPAC}^{\omega \rightarrow 3\pi}$ , fitted to CLAS-g8b data for $W : [2100 - 2200]$ MeV and $M_\omega : [740 - 820]$ MeV at widths of 5 MeV. The boundary factor used was $\phi_{physical}$ , Eqn. 6.13 . . . . .	114
6.52	JPAC $\omega \rightarrow 3\pi$ decay parameter, $a_{JPAC}^{\omega \rightarrow 3\pi}$ , fitted to CLAS-g8b data for $W : [2200 - 2300]$ MeV and $M_\omega : [740 - 820]$ MeV at widths of 10 MeV. The boundary factor used was $\phi_{physical}$ , Eqn. 6.13 . . . . .	115
6.53	JPAC $\omega \rightarrow 3\pi$ decay parameter, $a_{JPAC}^{\omega \rightarrow 3\pi}$ , fitted to CLAS-g8b data for $W : [2200 - 2300]$ MeV and $M_\omega : [740 - 820]$ MeV at widths of 5 MeV. The boundary factor used was $\phi_{physical}$ , Eqn. 6.13 . . . . .	115
6.54	JPAC $\omega \rightarrow 3\pi$ decay parameter, $a_{JPAC}^{\omega \rightarrow 3\pi}$ , fitted to CLAS-g8b data for $W : [1900 - 2340]$ MeV at widths of 10 MeV. The boundary factor used was $\phi_{physical}$ , Eqn. 6.13 . . . . .	116
6.55	JPAC $\omega \rightarrow 3\pi$ decay parameter, $a_{JPAC}^{\omega \rightarrow 3\pi}$ , fitted to CLAS-g8b data for $W : [1900 - 2340]$ MeV at widths of 10 MeV, $M_\omega \pm 40$ MeV. The boundary factor used was $\phi_{physical}$ , Eqn. 6.13 . . . . .	116
6.56	JPAC $\omega \rightarrow 3\pi$ decay parameter, $a_{JPAC}^{\omega \rightarrow 3\pi}$ , fitted to CLAS-g8b data for $W : [1900 - 2340]$ MeV at widths of 10 MeV, $M_\omega \pm 30$ MeV. The boundary factor used was $\phi_{physical}$ , Eqn. 6.13 . . . . .	117
6.57	JPAC $\omega \rightarrow 3\pi$ decay parameter, $a_{JPAC}^{\omega \rightarrow 3\pi}$ , fitted to CLAS-g8b data for $W : [1900 - 2340]$ MeV at widths of 10 MeV, $M_\omega \pm 20$ MeV. The boundary factor used was $\phi_{physical}$ , Eqn. 6.13 . . . . .	117
6.58	JPAC $\omega \rightarrow 3\pi$ decay parameter, $a_{JPAC}^{\omega \rightarrow 3\pi}$ , fitted to CLAS-g8b data for $W : [1900 - 2340]$ MeV at widths of 10 MeV, $M_\omega \pm 15$ MeV. The boundary factor used was $\phi_{physical}$ , Eqn. 6.13 . . . . .	118
6.59	JPAC $\omega \rightarrow 3\pi$ decay parameter, $a_{JPAC}^{\omega \rightarrow 3\pi}$ , fitted to CLAS-g8b data for $W : [1900 - 2340]$ MeV at widths of 10 MeV, $M_\omega \pm 10$ MeV. The boundary factor used was $\phi_{physical}$ , Eqn. 6.13 . . . . .	118
6.60	JPAC $\omega \rightarrow 3\pi$ decay parameter, $a_{JPAC}^{\omega \rightarrow 3\pi}$ , fitted to CLAS-g8b data for $W : [1900 - 2340]$ MeV at widths of 10 MeV, $M_\omega \pm 5$ MeV. The boundary factor used was $\phi_{physical}$ , Eqn. 6.13 . . . . .	119

# ABSTRACT

At the Continuous Electron Beam Accelerator Facility (CEBAF) at Jefferson National Laboratory (JLab),  $\omega$  vector mesons were photo-produced off a fixed, liquid-hydrogen target,  $\gamma p \rightarrow p\omega$ , during the 2005 and 2008 summer run-periods. With  $\omega \rightarrow \pi^+\pi^-\pi^0$  having the dominant branching ratio of 89%, the nearly  $4\pi$  CEBAF Large Acceptance Spectrometer (CLAS) was used to obtain a high statistics event sample of the reaction  $\gamma p \rightarrow p\omega \rightarrow p\pi^+\pi^-\{\pi^0\}$  where the undetected neutrals,  $\{\pi^0\}$ , were kinematically fitted. The energy-tagged photon beam was obtained from the electron beam through Bremsstrahlung radiation within a photon tagging system. Following reconstruction and refinement of the selected event data samples, the Experimental Hadronic Nuclear Group at Florida State University (FSU) has been working to extract the respective differential production cross sections.

With the data available and the differential cross section expected, I set out in close cooperation with the Joint Physics Analysis Center (JPAC) at JLab to conduct a Dalitz plot analysis of the  $\omega \rightarrow 3\pi$  strong decay. In particular, first-time preliminary fits of an isobar based, JPAC decay amplitude model were made using real event data. The model accounts for both elastic ( $\pi\pi - \pi\pi$ ) and inelastic (e.g.  $K\bar{K} - \pi\pi$ ) three-body re-scattering effects through the use of analytic and sub-energy unitarity methods.

The fits were performed using the unbinned, event-based Minimum Extended Log Likelihood Method (LLM) which is based on the Maximum Likelihood Method (MLM). The automated data and partial-wave analysis framework I have established utilizes the latest AmpTools partial-wave fitting package developed at Indiana University. Also, in lieu of the CLAS-g12 differential cross-section measurements and  $\omega$  Spin-Density-Matrix-Elements (SDMEs), those obtained from the CLAS-g11a experiment were used for some integrated fits. Consequently, results were restricted to the incoming photon energy range available during the CLAS-g11a run-period. SDME results for the CLAS-g12 and CLAS-g8b data sets are independently compared against those previously extracted and published by the CLAS-g11a group. Preliminary results are reported for the JPAC  $\omega \rightarrow 3\pi$  decay parameter which accounts for the unknown inelastic contributions.

# CHAPTER 1

## INTRODUCTION

### 1.1 Summary

At the Continuous Electron Beam Accelerator Facility (CEBAF) at Jefferson National Laboratory (JLab),  $\omega$  vector mesons were photo-produced off a fixed, liquid-hydrogen target,  $\gamma p \rightarrow p\omega$ , during the 2005 and 2008 summer run-periods. With  $\omega \rightarrow \pi^+\pi^-\pi^0$  having the dominant branching ratio of 89%, the nearly 4 $\pi$  CEBAF Large Acceptance Spectrometer (CLAS) was used to obtain a high statistics event sample of the reaction  $\gamma p \rightarrow p\omega \rightarrow p\pi^+\pi^-\{\pi^0\}$  where the undetected neutrals,  $\{\pi^0\}$ , were kinematically fitted. The energy-tagged photon beam was obtained from the electron beam through Bremsstrahlung radiation within a photon tagging system.

Track and event reconstruction were made possible by the collective measurements obtained from the beam timing, photon tagging system, and CLAS responses. Following particle identification, event selection, and kinematic fitting, the data sample was further refined through kinematic cuts, signal-background separation, and detector efficiency simulation. The Experimental Hadronic Nuclear Group at Florida State University (FSU) extracted the differential cross sections respective to each data set both of which are being refined at present [1].

In close cooperation with the Joint Physics Analysis Center (JPAC) at JLab, I conducted a Dalitz plot analysis of the  $\omega \rightarrow 3\pi$  strong decay. Together the Schilling equation [2] and JPAC  $\omega \rightarrow 3\pi$  decay amplitude [3] account for the decay distribution. The dispersive, isobar based JPAC model accounts for both elastic ( $\pi\pi - \pi\pi$ ) and inelastic (e.g.  $K\bar{K} - \pi\pi$ ) three-body re-scattering effects through the use of analytic and sub-energy unitarity methods. Spin density matrix elements (SDMEs) for the former distribution were extracted. First time fits of the JPAC decay parameter which accounts for the unknown inelastic contributions were investigated.

The partial-wave analysis framework I established utilizes the AmpTools (v0.9.2) [4] event-based fitting framework developed at Indiana University. The employed log-likelihood method is based on the unbinned, event-based, extended maximum likelihood method [5], and the fitter is based on the TMinuit class of ROOT [6]. This method depends upon the full (production and decay)

intensity function. In lieu of the CLAS-g12 differential cross-section measurements and  $\omega$  SDMEs, those obtained from the CLAS-g11a experiment [7] were used along with the CLAS-g12 and CLAS-g8b data. A detailed account of the framework, methods, and results are presented herein. The accessible framework is current and ready for future partial-wave analyses.

## 1.2 The Standard Model

The experimental and theoretical framework which describes the fundamental constituents of matter is referred to as the Standard Model of Particle Physics (SM) [8]. As described by the Standard Model, matter is comprised of fundamental constituents, namely structure particles called quarks and leptons (and their respective anti-particles) as well as force carrier particles which mediate the interactions between these structure particles. The interaction mediators are their own anti-particles save the charged “weak” bosons,  $W^\pm$ , which are respectively the anti-particles of one another. Lastly, mathematical descriptions of the fundamental interactions governing the SM particles are given in terms of so-called gauge-invariant renormalizable quantum field theories: Quantum Electrodynamics (QED), Electroweak Theory (EWT), and Quantum Chromodynamics (QCD). More formally, the mathematical framework of the SM is expressed through the coupling of EWT with QCD, where EWT is QED inclusive.

The integrity of the SM’s core-features such as the fundamental particle classification schemes and their theoretical interaction underpinnings remain very much the same today as they did when originally formulated. Perhaps, the pinnacle establishment period of the SM arrived around the early-to-mid-1970s. In particular, experimental confirmation [9, 10, 11] of quarks lent credence to the independently formulated constituent quark models (CQMs) originally proposed by Murray Gell-Mann [12] and George Zweig [13]. The CQMs then theorized the quarks to be the valence constituents of protons and neutrons and later more generally of hadrons. Not long thereafter, Quantum Chromodynamics, the renormalizable quantum field theory which describes the strong interactions in terms of both the color charged constituent quarks and the color-anticolor charged gluonic force-mediators, took the place of the CQMs in the SM [14, 15].

While most of us are commonly familiar with the building blocks of atomic nuclei, i.e. protons and neutrons (nucleons), the advent and advancement of particle colliders over the last half-century brought forth the discovery of a whole host of hadron-species as well as the observation of many of

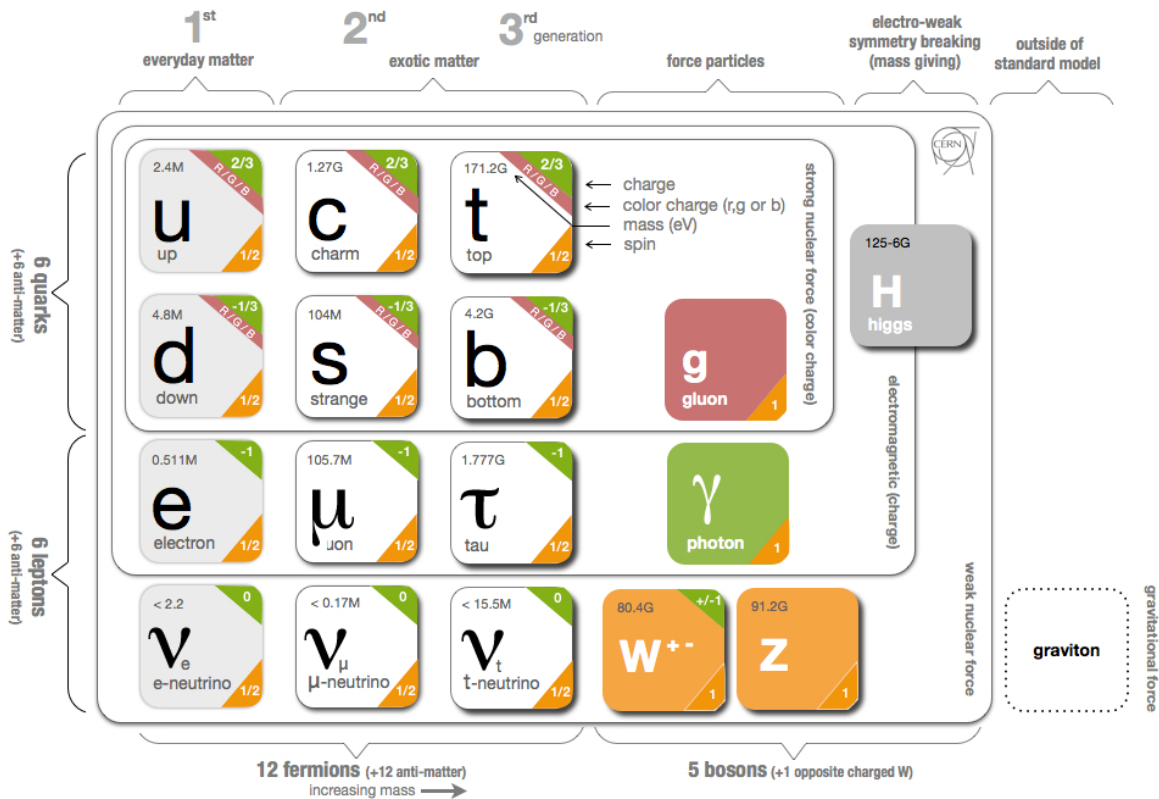


Figure 1.1: The Standard Model of Particle Physics (Image Source: [16])

their higher-energy (excited) or so-called resonant states. Over the last several decades, much work has gone towards mapping out the “spectrum” of hadronic resonances as well as searching for new and/or exotic hadronic species, e.g. the heavier quark excited bound states. It has been through the observation and analysis of the production and decay of these resonances that nuclear and particle physicists came to assemble and formulate the SM and particularly how today’s “hadronic” nuclear physicists continue to verify and test it for new physics beyond the Standard Model.

Figure 1.1 shows the current classification scheme of these fundamental particles. There are six “flavors” of quarks. They are organized into pairs corresponding to closeness in mass. These pairs span three generations of increasing mass. Each generation contains one quark with  $+2/3$  and the other with  $-1/3$  fractional electric charge. The quarks (antiquarks) carry one of three color (anti-color) charges, i.e. red, green, or blue (anti-red, anti-green, or anti-blue). Also, there are six

flavors of leptons. They are paired up based on the same so-called lepton flavor (e.g. electron and electron neutrino). The pairs span three generations according to increasing mass. The neutrinos (anti-neutrinos) are electric charge neutral and the remaining leptons (anti-leptons) have  $-1$  ( $+1$ ) electric charge.

The force carrier particles, referred to as gauge bosons, are classified according to the manner in which they mediate particle interactions. The gauge boson responsible for mediating the electromagnetic (EM) interaction is the photon,  $\gamma$ , which is massless. The weak gauge bosons along with the photon together mediate the electroweak (EW) interaction. These  $W^\pm$  and  $Z^0$  gauge bosons have mass, and they mediate the weak-decay of the heavier generation quarks and charged leptons into the more stable lower mass generations. In particular, the charged  $W^\pm$  bosons mediate charged current (CC) decays, e.g. a beta decay ( $n \rightarrow p + W^- \rightarrow p + e^- + \bar{\nu}_e$ ), whereas the neutral  $Z^0$  boson mediates neutral current (NC) decays, e.g. a Z-boson emission from an electron ( $e^- \rightarrow e^- + Z^0$ ).

The gauge bosons which mediate the strong interaction are the gluons which are massless. There are eight gluons corresponding to the unique color-anticolor charge combinations. These gluons are responsible for binding the color charged quarks together into states referred to generally as hadrons, the composite protons and neutrons for example. Since the gluons carry color charge, they may strongly interact amongst themselves as well. Finally, the Higgs boson is formulated as contributing the mass to the quarks and leptons through so-called Yukawa couplings, and it is “gauge-group related” with three other scalar particles which are responsible for giving mass to the weak gauge bosons [17, 18, 19, 20].

Furthermore, all SM particles are classified in terms of their statistical behavior which corresponds to their intrinsic spin characteristic, as fractional or integer (including zero) spin particles respectively obey Fermi-Dirac or Bose-Einstein wave-function statistics, i.e. anti-commutation and commutation relations respectively. Quarks and leptons are spin-1/2 particles and are collectively referred to as fermions, whereas the force carrier particles are referred to as bosons since they have integer-1 or 0 intrinsic spin. The theorized graviton is suspected to have spin-2 but its existence has not been confirmed by experiment and thus has not been subsumed into the SM. This statistical classification based on intrinsic spin extends to composite particle states as well, namely the hadron spectra of bound quark states (see Section 1.4).

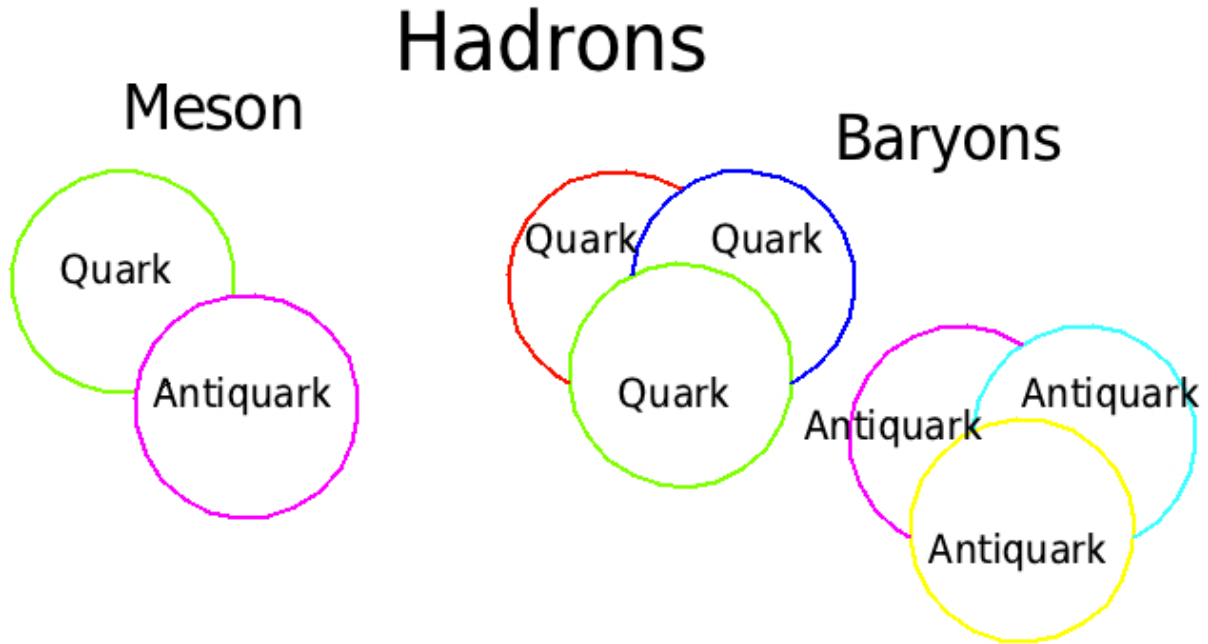


Figure 1.2: Hadrons, quark composite baryons and mesons, respectively represented with colorless color-charge combinations (Image Source: [22])

### 1.3 Confinement and Quantum Chromodynamics

Single quarks have never been observed in Nature to exist by themselves outside of the bound states of quark-antiquark pairs or quark-quark-quark triplets (or antiquark-antiquark-antiquark triplets). These bound states, respectively referred to as mesons and baryons (antibaryons), are collectively referred to as hadrons. In terms of color charge, hadrons form “color neutral” states, see Fig. 1.2. The quark-antiquark constituents of a meson must be a color-anticolor state, and the three-quark constituents of a baryon must be a red-blue-green (“white”) state. Antibaryons must be of antired-antiblue-antigreen states. This phenomenon is referred to generally as quark confinement. Understanding confinement and its underlying connection in Quantum Chromodynamics (QCD) is among the biggest “hot” topics in physics, particularly nuclear and hadronic nuclear physics.

Like Quantum Electrodynamics (QED) which describes the interactions between electrically charged particles and photons, Quantum Chromodynamics (QCD) describes the interactions between color charged particles and gluons. However in QCD, the gluons which mediate the interactions between the quarks contain color charge as well. As a consequence, the mathematical (group)

algebra which is used to describe electromagnetic charged interactions becomes considerably more complicated for the case of color charged interactions, so-called Abelian versus Non-Abelian group algebra, respectively [21].

As with classical fields and their corresponding interaction dynamics, quantum fields and their corresponding interactions may be written in terms of a governing Lagrangian. The gauge-invariant QCD Lagrangian (Lagrangian density) is given by

$$\mathcal{L}_{QCD} = \bar{q}_i(i\mathcal{D}_{ij} - m\delta_{ij})q_j - \frac{1}{4}G_{\mu\nu}^a G^{a,\mu\nu}, \quad (1.1)$$

where the antiquark,  $\bar{q}$ , and quark,  $q$ , are the Dirac spinors of the antifundamental and fundamental representations, respectively. There is an implicit sum over the quark color indices,  $i, j$ . The slash notation represents a Lorentz index contraction between a partial derivative or a gauge-field with the so-called Dirac gamma matrices, e.g.  $\mathcal{A}^a = A_\mu^a \gamma^\mu$ . The covariant derivative is given by

$$\mathcal{D} = \mathcal{D} - ig_s \mathcal{A}^a t^a, \quad (1.2)$$

where  $g_s$  is the strong coupling constant,  $\mathcal{A}^a$  are the eight ( $a = 1, \dots, 8$ ) gauge fields of the adjoint representation, and  $t^a \equiv \lambda^a/2$  are the eight generators spanning the color gauge group space. The  $\lambda^a$  are the so-called Gell-Mann matrices of the fundamental SU(3) representation. Also, the gluonic field strength tensors are given by

$$G_{\mu\nu}^a = [D_\mu, D_\nu]^a = \partial_\mu A_\nu^a - \partial_\nu A_\mu^a - gf^{abc} A_\mu^b A_\nu^c \quad (1.3)$$

where there is a sum over the gauge group index  $a$ . Lastly, the group generators are related to the structure constants  $f^{abc}$  via the following the commutation relation

$$[t^b, t^c] = if^{abc} t^a. \quad (1.4)$$

Note, the commutation relation of the SU(3) color group generators represents the Non-Abelian nature of QCD. Were the structure constants  $f^{abc}$  to be equal to zero, the self-interaction of the gluons would vanish, i.e. the triple- and quadruple-gluon vertices would be non-existent. In such a case, QCD would be reduced to the likeness of the Abelian gauge group representation and behavior of QED.

Furthermore in terms of QCD, two peculiar phenomena occur at two different energy regimes, namely asymptotic freedom at high energies and confinement at low energies. The two phenomena

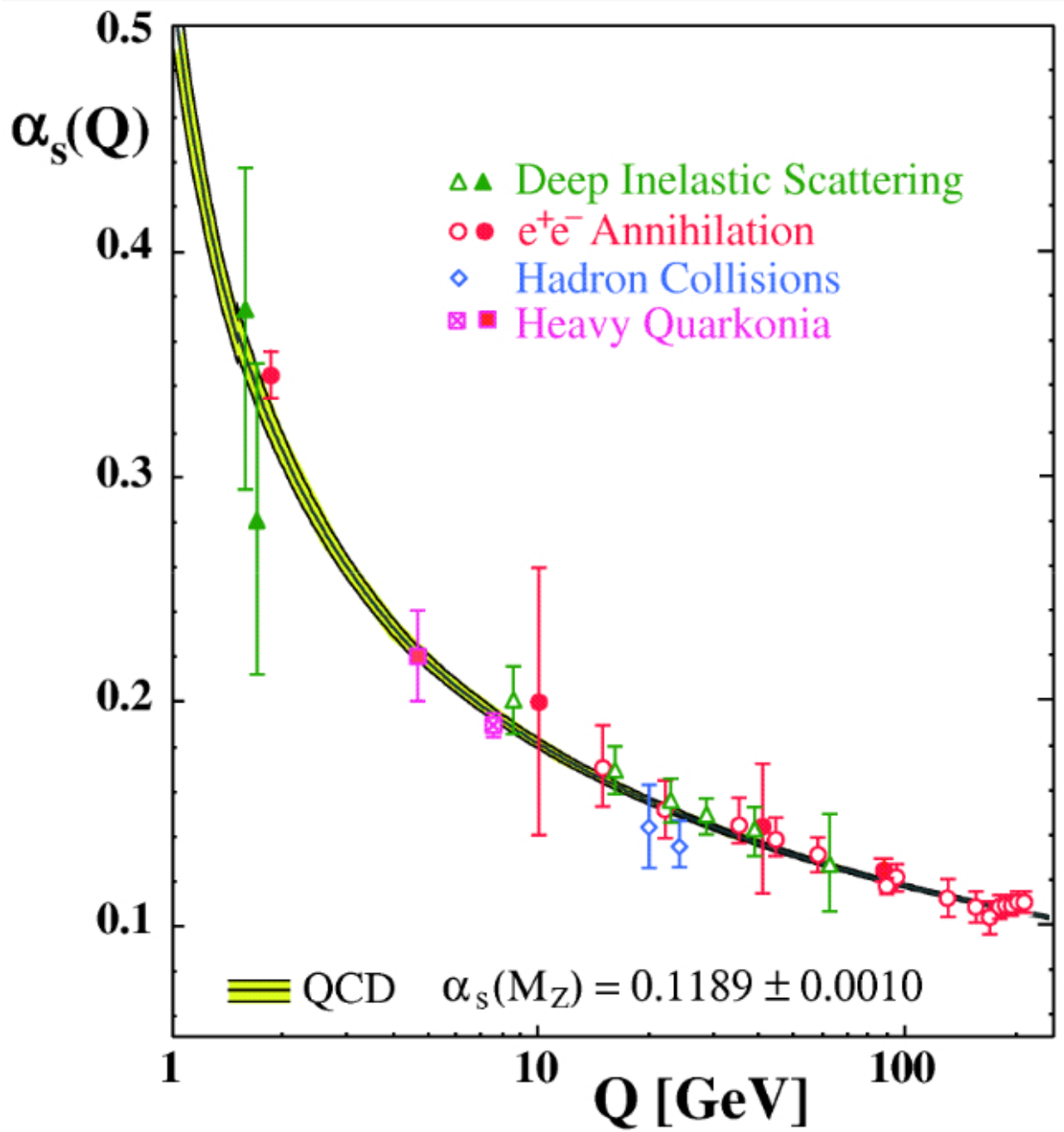


Figure 1.3: The strong coupling constant,  $\alpha_s(Q)$ , as a function of momentum transfer,  $Q^2$ , with the scaling parameter,  $\Lambda_{QCD} = M_Z$ , chosen as the Z boson mass [24]

can be investigated in terms of the strength of the strong coupling constant,  $\alpha_s \equiv g_s^2/4\pi$ , which depends widely upon the four-momentum transfer,  $Q^2$ , of the interaction [23]. Following Fig. 1.3, for high momentum transfer, large  $Q^2$  or  $Q$ ,  $\alpha_s$  decreases; whereas, for low momentum transfer, low  $Q^2$  or  $Q$ ,  $\alpha_s$  increases. The former is referred to as asymptotic freedom, and it allows for the use of perturbation theory when calculating high-energy (short distance) QCD interactions [25]. On the other hand, the latter leads to the non-perturbative low energy (large distance) QCD regime, which make calculations of QCD interactions extraordinarily difficult if not entirely intractable. For example, here, any number of the coupling proportional terms spanning a perturbative expansion of the strong interaction wave-function could add sizable contributes, i.e. perturbation theory fails. Moreover, while confinement has not yet been analytically proved [26], the Non-Abelian nature of QCD does more or less describe a picture consistent with experiment regarding the screened behavior of strong interactions in the low energy regime.

For a simple illustration of the interesting and unique issue at hand with QCD and the apparent quark confinement, consider the meson. If only the electromagnetic (EM) interaction between the quark and antiquark were at play, the two electrically charged particles could inevitably be separated. This is because with sufficient application of an external force, the coulomb force between the two charged particles decreases with increased separation distance. This is not the case in QCD. Instead, as the separation distance between the colored quark and anti-colored antiquark increases, the gluonic field energy between the two increases until enough energy is present to produce another quark-antiquark pair. This effect is referred to as hadronization. At high momentum transfer regions, high energy collisions, heavy hadronization occurs, often referred to as a quark and gluon “soup”. The resulting short-distance bound quark states become asymptotically weaker through increased momentum transfer collisions. This behavior of the strong interaction is referred to as the asymptotic freedom of QCD. Consequently, the decrease in the strong coupling constant at high momentum transfer allows for perturbative expansions of the strong interaction amplitudes in the high energy regime. For the low energy regime, non-perturbative methods are the only means by which solutions to the strong interactions may be obtained.

## 1.4 Symmetries, Groups, and Spectroscopic Notation

The particle groupings illustrated by the SM classification scheme of Fig. 1.1 are predominantly based on experimentally observed intrinsic properties (observables) of the fundamental particles. The remaining classifications are based on quantum field theories consistent with the experimentally observed interaction dynamics of the particles. These intrinsic properties as well as the dynamical properties alike arise from so-called symmetries which in turn correspond to conserved quantities [27]. In this section, it is the aim to introduce some additional symmetries specific to quantities conserved by the strong interactions. These observables are common to hadron spectroscopy, and some particular to meson spectroscopy. Moreover, these additional quantum numbers are used both for further particle classification as well as identifying conservation constraints which limit the number of possible hadron collision or decay transition states. Lastly, symmetries may be of either the continuous or discrete type. The continuous types tend to be additive. For example, the total angular momentum of a hadron is the vector sum of the constituent quark spins and their relative orbital angular momentum. The discrete symmetries discussed here are all multiplicative.

Conserved dynamic quantities such as energy, linear momentum, angular momentum, charge, and current are associated with so-called continuous symmetries. Symmetries of the continuous type are represented mathematically by continuous unitary “group” objects called Lie groups. For example, the conservation of electric charge in electromagnetism is expressed by the “local” field transformation represented by the  $U(1)$  unitary group. Also, the gauge groups of the electroweak, and strong interactions are represented by particular  $SU(2) \otimes U(1)$ , and  $SU(3)$  groups respectively. The special unitary  $SU(N)$  groups of degree  $N$  are represented by  $N \times N$  unitary matrices. Also, they have  $N^2 - 1$  so-called generators associated with the symmetries of the space. For example, under the  $SU(3)$  color group representations, the colored-quarks and anti-colored antiquarks reside in the so-called irreducible fundamental,  $\mathbf{3}$ , and anti-fundamental,  $\bar{\mathbf{3}}$ , representations, respectively. The gluon fields carry both a color and anti-color assignment. They reside in the equivalent irreducible adjoint representation of  $SU(3)$  color group; as such, there are  $3^2 - 1 = 8$  generators of the  $SU(3)$  color group which correspond to the 8 possible gluon field types.

Similar to that of the dynamically conserved quantities such as total angular momentum,  $J$ , and orbital angular momentum,  $L$ , as well as the intrinsically conserved quantity called spin (no classical analogue but akin to the spin of a top),  $S$ , there exists an additional quantity represented

by the SU(2) symmetry group which is solely conserved through strong interactions of hadrons. Like spin, this internal symmetry is used to further group hadrons into common wave-state multiplets (e.g. singlets, doublets, triplets, etc.) corresponding to the shared symmetry. However, unlike spin, this symmetry is an approximate one. Isospin refers to the invariance of a particle or set of particles of similar mass and different electric charge with respect to the strong interaction. For example, the up and down quarks are isospin partners each said to have an isospin  $I_{u,d} = 1/2$ . They are similar in mass and their electric charge differs but they are affected in the same manner in terms of the strong interactions. Due to the mass difference of the pair, presumed to be due to the electromagnetic interaction, this symmetry is said to be an approximate one. Also, since isospin partners are independent of electric charge, the individual charged member states share the same isospin quantum number. At the hadronic level, the proton and neutron are isospin partners ( $I = 1/2$ ) with similar mass and differing electric charge. The  $\pi$  and  $\rho$  mesons respectively span an isospin space of  $I = 1$ . In terms of Cartesian coordinates, the proton and neutron have z-component isospin states of  $I_z = +1/2, -1/2$ , respectively. The  $\pi^+(\rho^+)$ ,  $\pi^0(\rho^0)$ ,  $\pi^-(\rho^-)$ , particles correspond with the z-component isospin states  $I_z = +1, 0, -1$ , respectively.

For hadron spectroscopy, some additionally useful quantum numbers conserved by the strong interactions are those associated with so-called discrete symmetries. These discrete symmetries are: Parity, particle-antiparticle conjugation, and G-Parity where G-Parity is of specific use in meson spectroscopy only. These finite groups each operate on two respective states sharing the same eigenbasis which correspond to two eigenvalues,  $\pm 1$ .

Parity is conserved in electromagnetic and strong interactions but violated in weak interactions. In one dimension, it is an operation which flips the coordinate axes. In three dimensions, this is an operation which inverts or flips the three spatial axes of a coordinate system. This can also be done by the flip of one axis followed by a rotation of 180 degrees about the flipped axis. In terms of an image, parity inversion is what relates an image to its mirror image. In general terms of basic physical quantities and their respective mathematical forms, parity inverts coordinates and momentum (vectors) but does not affect time (scalars), angular momentum (axial- or pseudo-vectors), or spin.

The parity of a wave function is said to be even (odd) when the wave function is symmetric (antisymmetric) upon a parity transformation. In terms of a single particle state, the eigenvalue of

its intrinsic parity is either  $\pm 1$ . The vacuum state has a parity of  $+1$  by definition; it is its own mirror image and should not flip upon a parity transformation. The parity of the proton is conventionally taken as  $+1$ . Moreover, conservation of energy dictates that particle and antiparticles be equally produced from the vacuum state. Thus, considering the production of a proton-antiproton pair, the relative parity of the antiproton must be  $-1$ . This is the general rule for all fermion and antifermion pairs, with for example electrons and anti-electrons (positrons) having intrinsic relative parities conventionally taken as  $+1$  and  $-1$ , respectively. In addition, the parity of a boson and its antiboson are taken to be the same. For example, the  $\pi^+$  meson and its antiparticle,  $\pi^-$ , each have a parity of  $-1$ . The field of a photon is represented by a vector and therefore its parity eigenvalue is  $-1$ .

Following the convention of the proton (anti-proton), its constituent quarks (antiquarks), have positive (negative) parity. The general rule is that all quarks (antiquarks) have positive (negative) parity. In terms of hadrons, the overall intrinsic parity is given multiplicatively (unlike addition for charge) from the intrinsic parity of the constituent quarks. Furthermore, the parity for a two particle system is given by the multiplication of the intrinsic parities times an orbital angular momentum parity dependence, namely

$$P_{12} = P_1 P_2 (-1)^l \quad (\text{two particles}) \quad (1.5)$$

$$P_{m,m} = (\pm 1)^2 (-1)^l = (-1)^l \quad (\text{equal parity meson pair}) \quad (1.6)$$

$$P_{f,\bar{f}} = (+1)(-1)(-1)^l = (-1)^{l+1} \quad (\text{fermion-antifermion pair}). \quad (1.7)$$

Particle-antiparticle Conjugation (C), also called charge-conjugation and C-Parity, is an operation which changes a particle into its anti-particle. Electromagnetic and strong interactions conserve this quantity while the weak interaction does not. Only neutral bosons (e.g. photons, neutral mesons, meson-antimeson pairs, fermion-antifermion pairs) are eigenstates of this operation with corresponding eigenvalues given below,

$$C_\gamma = (-1) \quad (\text{photon}) \quad (1.8)$$

$$C_{\gamma^n} = (-1)^n \quad (\text{n photons}) \quad (1.9)$$

$$C_{\pi^0} = C_{\gamma^2} = (-1)^2 = +1 \quad (\text{neutral pion, } \pi_0) \quad (1.10)$$

$$C_{m,\bar{m}} = (-1)^{l+s} \quad (\text{c.m. meson-antimeson pair}) \quad (1.11)$$

$$C_{f,\bar{f}} = (-1)^{l+s} \quad (\text{c.m. fermion-antifermion pair}), \quad (1.12)$$

Table 1.1: Meson Spectroscopic Notation,  $I^G J^{PC}$

J	Total Angular Momentum - $\vec{J} = \vec{L} + \vec{S}$
L	Orbital Angular Momentum, S - Spin
P	Parity - coordinate inversion
C	Particle-Antiparticle Conjugation - particle-antiparticle swap
I	Isospin - charge-multiplet states of “same” (similar mass, same spin) particle
G	G-Parity - y-component isospin inversion & particle-antiparticle swap

Table 1.2: Spectroscopic notation values for  $\gamma p \rightarrow p \omega \rightarrow p 3\pi$

$\gamma$	$0, 1(1^{--})$
$p$	$\frac{1}{2}(\frac{1}{2}^+)$
$\omega(782)$	$0^-(1^{--})$
$\pi^\pm$	$1^-(0^-)$
$\pi^0$	$1^-(0^{-+})$

where the  $(-1)^s$  accounts for the spin exchange, e.g. a factor arising from the exchange of spin among symmetric (even) and antisymmetric (odd) spin wavefunction.

While this symmetry under particle-antiparticle conjugation is rather limited as it only applies to neutral bosons, its application is extended to apply to the charged (non-strange non-baryonic) states as well. G-Parity is the application of particle-antiparticle conjugation ( $C$ ) followed by a  $180^\circ$  rotation about the y-component of isospin space,  $I_y$ , namely  $G \equiv exp(i\pi I_y)C$ . G-Parity involves isospin which makes it an approximate invariant of strong interactions but which is not an invariant of the electroweak interaction. The quantum numbers used in the study of hadrons, particularly mesons (G-Parity inclusive), are listed in Table 1.1, and the values used in my analysis of the  $\omega \rightarrow 3\pi$  decay (for the overall production and decay products,  $\gamma p \rightarrow p\omega \rightarrow p\pi^+\pi^-\{\pi^0\}$ ) are given in Table 1.2.

## 1.5 Resonance Decays and Analysis Motivation

Hadron spectroscopy involves the identification of hadronic resonances in terms of their respective masses, widths, and conserved quantum numbers. These properties are determined for a given resonance through measurements involving consideration of both initial and final state particle properties as well as partial wave studies with respect to its modelled production and decay mechanisms. The production and decay mechanisms of a resonance also each provide unique information about its internal dynamics.

A matter of seminal importance in hadronic physics is to understand the decay mechanism underlying three-body decays such as those found for the  $\omega$ ,  $\phi$ , and  $\eta$  resonance decays. Each of these vector meson resonances have a decay channel to the three-pion final state, e.g.  $\omega \rightarrow 3\pi$ . Several other meson resonances have been discovered through three-pion production [8]. Dispersive methods for modelling such relativistic three-body decays have been used in the past [28, 29] and have regained popularity again [30, 31].

The aforementioned three-body vector meson decays serve as base level testing grounds for these dispersive treatments. Several dispersive treatments can now be found in particular for the  $\omega \rightarrow 3\pi$  decay [32, 33, 3]. The  $\omega, \phi \rightarrow 3\pi$  decays may each and collectively reveal insights about vector meson formation and decay characteristics restricted by unitarity and long-range interactions [3]. The  $\eta \rightarrow 3\pi$  decay is of interest because it is sensitive to isospin breaking originating due to the mass difference between the up and down quarks. There is an ongoing decay analysis being performed by the University of Bonn group for the three-body decay of the D meson,  $D \rightarrow K\pi\pi$ , which uses a similar formalism to that used in the analysis presented herein [34]. These are the points of motivation for my analysis, a Dalitz plot analysis of the  $\omega \rightarrow 3\pi$  decay.

## 1.6 Partial Wave Analysis

In conjunction with my Dalitz plot analysis, I have performed event-based fitting of intensity functions using the log likelihood method. The intensity functions I fit are proportional to the squared decay amplitude which may also be referred to as the decay intensity or decay probability density. Given a kinematic event, this is simply a measure of probability that the decay occurred. Moreover, the event-based log likelihood method is based on the maximum likelihood method whereby the product of individual event probabilities is maximized upon convergence of the fit.

Additionally, within the decay intensity, the angle dependencies of the decay were isolated into a factor called the angular decay distribution (ADD) [2]. The remaining angle-independent factor of the decay intensity is proportional to the decay width and may be referred to as the square of the reduced decay amplitude. The angular decay distribution (ADD) depends upon the decay angles of the  $\omega$  resonance in its rest-frame along with so-called Spin-Density-Matrix-Elements (SDMEs) for the resonance. In turn, these SDMEs depend upon the incoming photon (beam) polarization and the squared production amplitude. In fact, the measurements of the differential production cross section which is proportional to the squared production amplitude, were crucial for my unbinned, event-based fits of the ADD.

Additionally, Fortran code for the (reduced) decay amplitude which was based on an isobar model and the use of sub-energy unitarity was provided by the Joint Physics Analysis Center (JPAC) at Jefferson Laboratory (JLab). Note, sub-energy is simply a reference to the energy of the isobars or any two of the final decay particles subsequent to the decay of the resonance. This amplitude not only accounts for three-body, re-scattering effects but also for the analytic changes caused by the opening of inelastic channels [3]. Also of importance is that while this reduced decay amplitude has been compared with that of similar models, [33, 35], this was the first time it had been fitted to real data.

## 1.7 The Dalitz Plot Distribution

Averaging over the spins of the initial state, the partial decay width for a three-body decay is given by

$$d\Gamma = \frac{1}{(2\pi)^3} \frac{1}{8M} \overline{|\mathcal{M}|^2} dE_1 dE_2. \quad (1.13)$$

By defining  $p_{ij} = p_i + p_j$  for the 4-momentum of a particle-pair, its squared invariant mass is given by

$$m_{ij}^2 = (p_i + p_j)^2 = (P - p_k)^2 = M^2 + m_k^2 - 2ME_k \quad (1.14)$$

and the decay width may be expressed as

$$d\Gamma = \frac{1}{(2\pi)^3} \frac{1}{32M^3} \overline{|\mathcal{M}|^2} dm_{12}^2 dm_{23}^2 \quad (1.15)$$

where the phase space has taken the standard form used in the Dalitz plot, see Fig. 1.4.

The boundaries of the phase space are dictated by the conservation of the 4-momenta of the three final state particles as well as the overall center of momentum for the decay system. One may obtain  $(m_{ij}^2)_{min}$  and  $(m_{ij}^2)_{max}$  from Eqn. 1.14 by considering the following:

$$\begin{aligned}
(m_{ij}^2)_{min} &= (p_i + p_j)^2 \\
&= (E_i + E_j)^2 - (\vec{p}_i + \vec{p}_j)^2 \\
&\stackrel{\vec{p}_i = -\vec{p}_j}{=} \left( \sqrt{m_i^2 + |\vec{p}_i|^2} + \sqrt{m_j^2 - |\vec{p}_i|^2} \right)^2 \geq (m_i + m_j)^2
\end{aligned} \tag{1.16}$$

$$\begin{aligned}
(m_{12}^2)_{max} &= M^2 + m_k^2 - 2ME_k \\
&\stackrel{p_k \rightarrow 0}{=} M^2 + m_k^2 - 2Mm_k = (M - m_k)^2
\end{aligned} \tag{1.17}$$

where the relative momenta are considered in the rest frame of the  $ij$ -particle-pair for  $(m_{12}^2)_{min}$  and  $p_k = 0$  is considered in the rest frame of the decaying resonance for  $(m_{12}^2)_{max}$ . For a constant (non-constant) squared decay amplitude,  $|\mathcal{M}|^2$ , the observed phase space would be flat (non-flat). Thus, a flat phase space indicates an absence of physics dynamics.

Furthermore, for three-body decays with final state particles of similar masses, another representation of the Dalitz plot may be made by plotting the phase space in terms of dimensionless Lorentz invariant variables,  $x = \sqrt{3}(T_j - T_i)/Q$  and  $y = 3T_k/Q - 1$  where  $T$  and  $Q$  respectively represent the individual and total kinetic energy of the final state particles, see points O and P of Fig. 1.5. This representation takes advantage of a geometric proof that the altitude length of an equilateral triangle is equal to the sum of the distances from any interior point to the sides of the triangle [37], i.e.  $Q = T_i + T_j + T_k$ . The radius of a circle inscribed within an equilateral triangle is equal to  $1/3^{\text{rd}}$  the altitude length of the triangle, hence the radius in the figure has a length of  $Q/3$ . The Dalitz plot boundary deviates from the circular shape in the figure due to the physical constraint of conservation of energy-momentum of the decaying resonance. The Cartesian  $x$  and  $y$  variables as well as the polar  $r$  and  $\theta$  variables simply relate the origin,  $O$ , to the point of interest,  $P$ , of the Dalitz plot distribution.

Following the non-relativistic Zemach formalism [38] for obtaining the three-body  $3\pi$  decay amplitudes in terms of relevant quantum numbers, the Dalitz plot distribution for the  $\omega \rightarrow \pi^+\pi^-\pi^0$  and its distinguishing characteristics, notably the vanishing regions, can be readily understood.

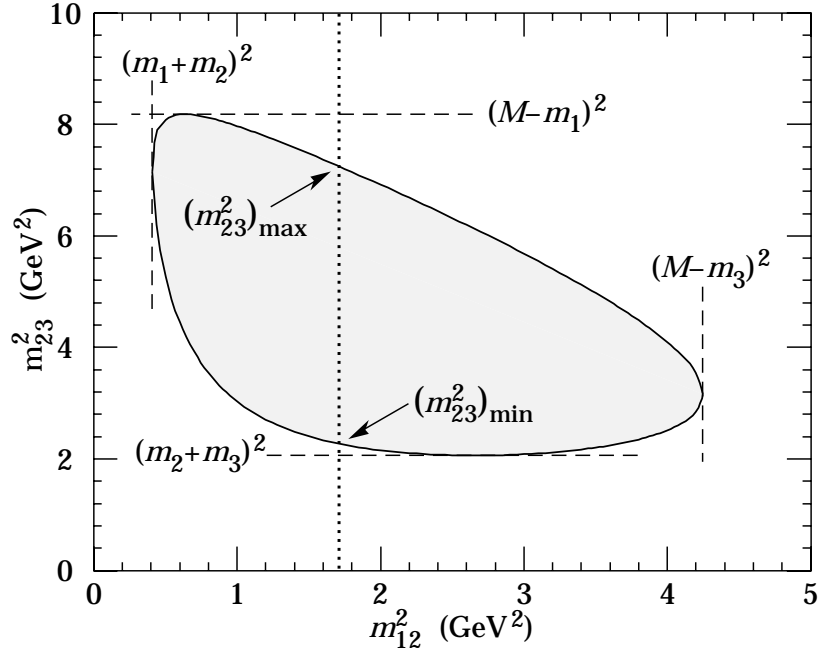


Figure 1.4: A Dalitz plot expressed in terms of final state particle-pair masses and with illustrated kinematic boundaries [8]

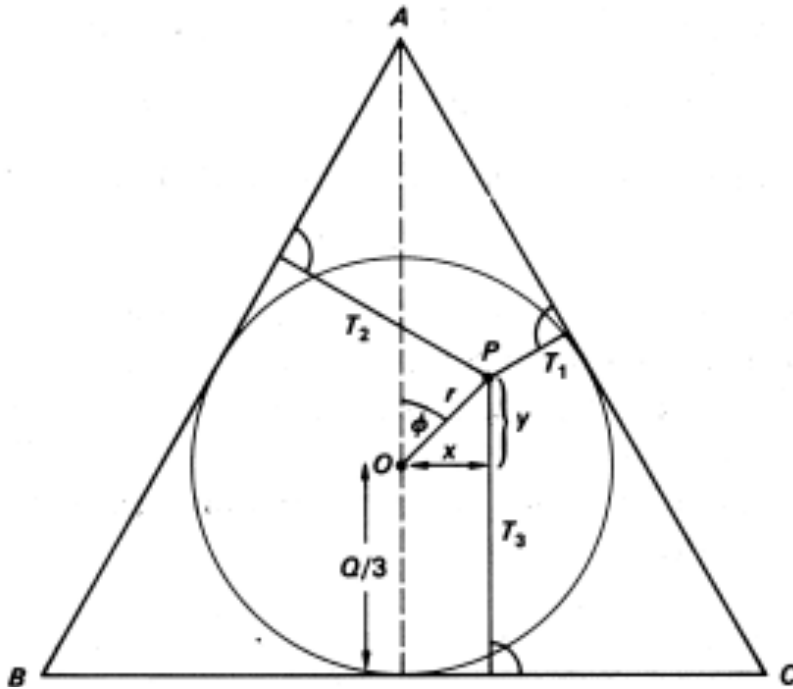


Figure 1.5: A symmetric representation of the Dalitz plot expressed either in (dimensionless)  $x$  and  $y$  or polar  $r$  and  $\theta$  variables (Image Source: [36])

Note, while the overall decay amplitude used in my analysis was constructed in the relativistic covariant tensor formalism, it is argued [63] that the non-relativistic and relativistic amplitudes (at least for the  $\omega \rightarrow 3\pi$  decay) are equivalent in the rest frame of the decaying  $\omega$  resonance. Since the ansatz construction of the overall decay amplitude is quite similar in each case, the adequate non-relativistic treatment offers a simpler means for introducing and motivating the ideas behind such construction. One starts off then with the construction of a general decay amplitude for a vector meson decay to three pseudoscalar pions following the non-relativistic Zemach formalism. The decay amplitude is in general specified by isospin, total angular momentum, parity, and Bose statistics. It is constructed in the rest frame of the decaying resonance. The general non-relativistic decay amplitude is then given by the following sum of products:

$$M = \sum M^I M^{JP} M^F \quad (1.18)$$

which carry the isospin  $I$  dependence, total angular momentum  $J$  and parity  $P$  dependence, and the form factor (e.g. Breit-Wigner, Phase Shift) energy-momentum dependence respectively. Additionally, the conservation of energy-momentum in the resonance rest frame gives the constraints

$$E_1 + E_2 + E_3 = M_V, \quad \vec{p}_1 + \vec{p}_2 + \vec{p}_3 = 0. \quad (1.19)$$

For the case of the  $\omega$  vector meson ( $I_\omega = 0$ ) decaying to the three pseudoscalar pions (each  $I_\pi = 1$ ) (neutral mode  $\pi^+\pi^0\pi^-$  only),  $M_I$  may only be given by coupling an axial vector to a vector,

$$M_I = (\vec{I}_{\pi^+} \times \vec{I}_{\pi^-}) \cdot \vec{I}_{\pi^0} = i, \quad (1.20)$$

where the pion iso-vectors were conventionally given by

$$\begin{aligned} \vec{I}_{\pi^+} &= -\frac{1}{\sqrt{2}}(1, i, 0), \\ \vec{I}_{\pi^-} &= \frac{1}{\sqrt{2}}(1, -i, 0), \\ \vec{I}_{\pi^0} &= (0, 0, 1). \end{aligned} \quad (1.21)$$

In general, we may express all three dipion (isobar) combinations with the third pion, i.e.  $\vec{I}(\omega) = \vec{I}(3\pi) = \vec{I}_{12}(\pi_1\pi_2) \otimes \vec{I}_3(\pi_3)$ , through the totally anti-symmetric Levi-Civita as,

$$\sum_{ijk} M_{ijk}^I = \epsilon_{ijk} I_{\pi_i} I_{\pi_j} I_{\pi_k} \quad (1.22)$$

where isospin conservation dictates that  $I_{12} = 1$  and  $I_3 = 1$  to get  $I_{total} = 0$ .

Also,  $M_{JP}$  for  $J > 0$  are to be constructed from combinations of the resonance final state decay particle momenta. Thus,  $M_{JP}$  for  $\omega \rightarrow 3\pi$  ( $J_\omega^P = 1^-$  and  $J_\pi^P = 0^-$  respectively), is simply represented in terms of a pseudovector,  $\vec{q}$ , constructed from the pion momenta,  $\vec{p}_1, \vec{p}_2, \vec{p}_3$ , namely

$$\vec{q} = \vec{p}_1 \times \vec{p}_2 = \vec{p}_2 \times \vec{p}_3 = \vec{p}_3 \times \vec{p}_1. \quad (1.23)$$

In general, we may again express all three dipion (isobar) combinations with the third pion, i.e.  $\vec{J}(\omega) = \vec{L}(3\pi) = \vec{l}_{12}(\pi_1\pi_2) \otimes \vec{l}_3(\pi_3)$ , through the totally anti-symmetric Levi-Civita as,

$$\sum_{ijk} M_{ijk}^{JP} = \epsilon_{ijk} p_{\pi_i} p_{\pi_j} p_{\pi_k} \quad (1.24)$$

where spin-parity conservation dictates that  $J^P = 1^-$ . With  $\mathcal{M}_{decay} \propto \vec{q}$  for  $I = 0$  and  $J^P = 1^-$ , one may predict as Zemach did the vanishing region of the Dalitz plot. In particular, when two pions are back-to-back or collinear (see Fig. 1.4),  $\vec{q}$  and hence  $\mathcal{M}_{decay}$  vanish. Comparing the vanishing regions of our CLAS-g12 signal data Dalitz plot, Fig. 1.7, with those predicted by the non-relativistic Zemach formalism, Fig. 1.6, for the quantum numbers  $I = 0$  and  $J^P = 1^-$ , one observes good agreement.

In addition, with the system parity relation given by

$$P = (-1)^3 (-1)^{l_{12}} (-1)^{l_3} = (-1)^{l_{12}+l_3+1}, \quad (1.25)$$

the sum of dipion orbital angular momentum,  $l_{12}$ , and relative third pion orbital angular momentum,  $l_3$ , must be even (i.e.  $l_{12} + l_3 = 0, 2, \dots$ ). Consequently and important to note, spin-parity conservation and Bose Symmetry for the  $\omega \rightarrow 3\pi$  decay dictate that a partial wave expansion sum over total angular momentum  $J$  may take on integer values only, i.e.  $J_\omega = 1, 3, \dots$ . Due to Bose symmetry,  $l_{12} = \text{odd}$ ; therefore given  $l_{12} + l_3 = \text{even}$ ,  $l_3 = \text{odd}$  as well. Moreover, with  $\vec{J}_\omega = \vec{l}_{12} + \vec{l}_3$ , the quantum number  $J_\omega = 1$  may be obtained when  $l_{12} = l_3 = \text{odd}$ . This may be observed by noting the consequence of this condition for the last two terms in the following series given by the addition of angular momentum theorem,

$$J_\omega = l_{3\pi} = l_1 + l_2, l_1 + l_2 - 1, \dots, |l_1 - l_2| + 1, |l_1 - l_2| \quad (1.26)$$

where  $J_{3\pi} = L_{3\pi}$  as  $S_{3\pi} = 0$  for our spinless 3-pion final state. Thus, for example, when  $l_{12} = l_3 = 1$ , vector addition gives us the set  $J_\omega = \{2, 1, 0\}$ , and we may have  $J_\omega = 1$ . Also, for  $l_{12} = l_3 = 3$ , one

Spin	I=0	I=1 (except $3\pi^0$ )	I=2		I=1 ( $3\pi^0$ only) and I=3
			$\pi^+ \pi^- \pi^0$	other modes	
$0^-$					
$1^+$					
$2^-$					
$3^+$					
$1^-$					
$2^+$					
$3^-$					

Figure 1.6: Predicted Dalitz plot vanishing regions from the Zemach formalism [38]

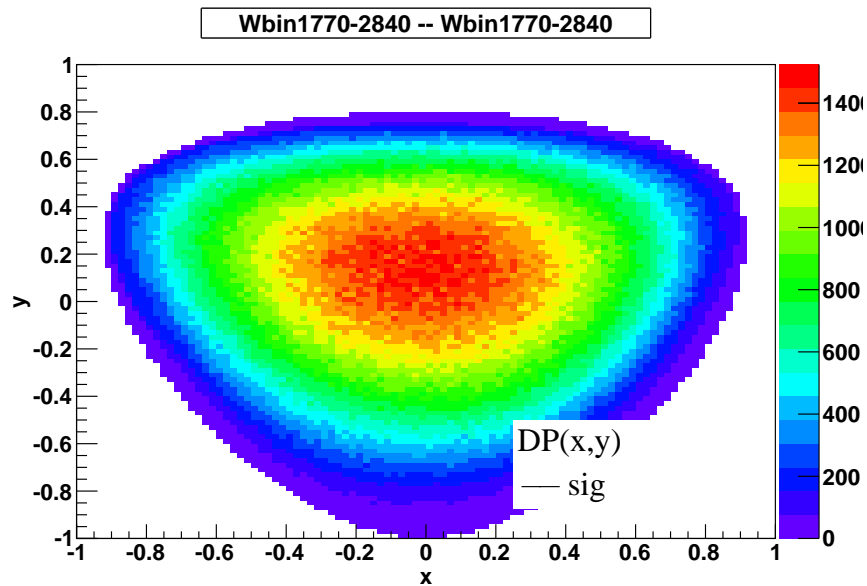


Figure 1.7: A Dalitz plot expressed in terms of dimensionless  $x$  and  $y$  variables using CLAS-g12 (signal) data for  $W$  : [1770 – 2840] MeV

obtains  $J_\omega = \{6, 5, 4, 3, 2, 1, 0\}$ ; and again, the case  $J_\omega = 1$  may be obtained. On the contrary, for  $l_{12} = 3$  and  $l_3 = 1$  or vice versa, we get  $J_\omega = \{4, 3, 2\}$  where  $J_\omega = 1$  is not possible.

## 1.8 The Experiment and Data

The two data sets used in this analysis originated from a fixed target experiments at the Continuous Electron Beam Accelerator Facility (CEBAF) located at JLab, Newport News, Virginia, using the CEBAF Large Acceptance Spectrometer (CLAS), see Fig. 2.1. CLAS is housed in Hall B, see Figures 2.2 and 2.5. While this detector was purposefully designed for the search and high-acceptance detection of baryon resonances, high-acceptance detection of photo-produced meson resonances were frequent bi-products of the CLAS experiments. During the summer 2005 and summer 2008 run periods, respectively the CLAS-g8b and CLAS-g12 experiments, light  $\omega$  vector mesons were photo-produced off a fixed, unpolarized, liquid-hydrogen target and the charged final-state particles for the sought reaction  $\gamma p \rightarrow p\omega \rightarrow p\pi^+\pi^-\{\pi^0\}$  were subsequently detected and recorded by CLAS. The parentheses around the neutral pion indicate that the neutral pion was undetected, yet it was reconstructed from kinematic fitting utilizing over-constrained event kinematics.

Having reconstructed, event selected, kinematically fitted, background subtracted, and acceptance corrected the two data sets, the differential cross sections respective to each set were extracted at FSU and are being refined at this time [1]. The differential production cross sections were in part determined from the counts of  $\omega$  events and target-incident photons. Respective to each data set, events were selected from reconstructed tracks which contained the charged particle final state  $p\pi^+\pi^-$ . Kinematic fits were obtained for the 4-momenta and vertices of the initial- and final-state particles, i.e.  $\gamma p$  and  $p\pi^+\pi^-\{\pi^0\}$  respectively. The kinematic fits were performed using the least squares method. The goodness-of-fit and quality of errors were determined through the use of the confidence level (CL) and pull distributions, respectively.

The background was reduced from the signal events using various kinematic cuts, see Ch. 4. The remaining background and signal were separated, see Figs. 1.8 and 1.9, using the quality factor (Q-value) method which assigns each event a weight corresponding to it likeliness of being a signal versus background event. Lastly, the efficiency of the detector to account for all  $\omega$  resonances was determined through a software called GSIM. This software simulates detector inefficiencies associ-

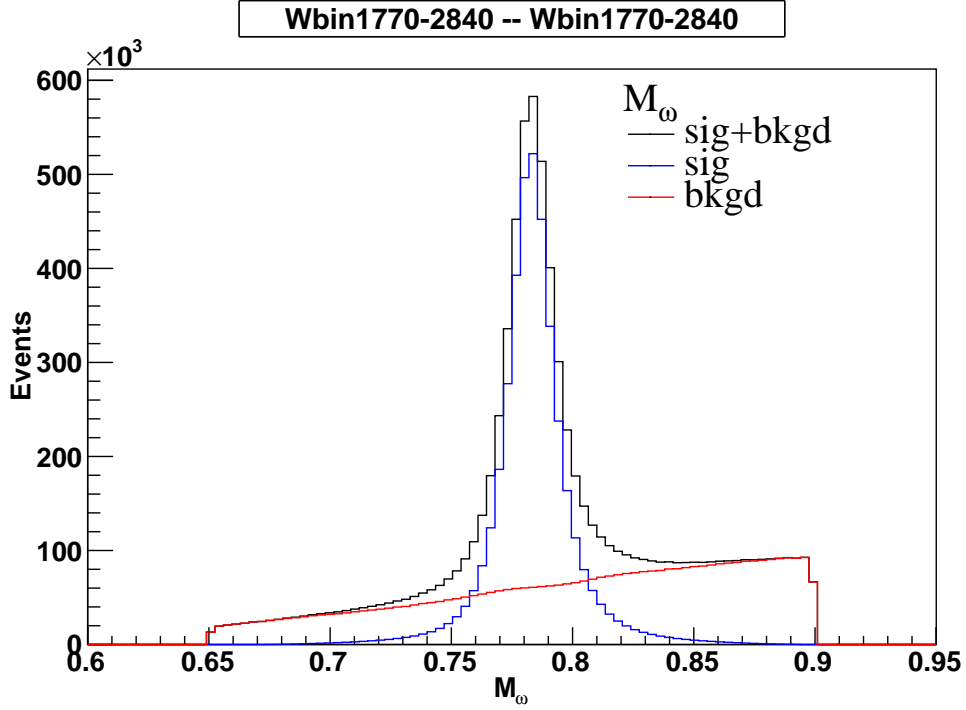


Figure 1.8: The (background separated)  $\omega$  mass,  $M_\omega$ , distribution from CLAS-g12 data for  $W : [1770 - 2840]$  MeV

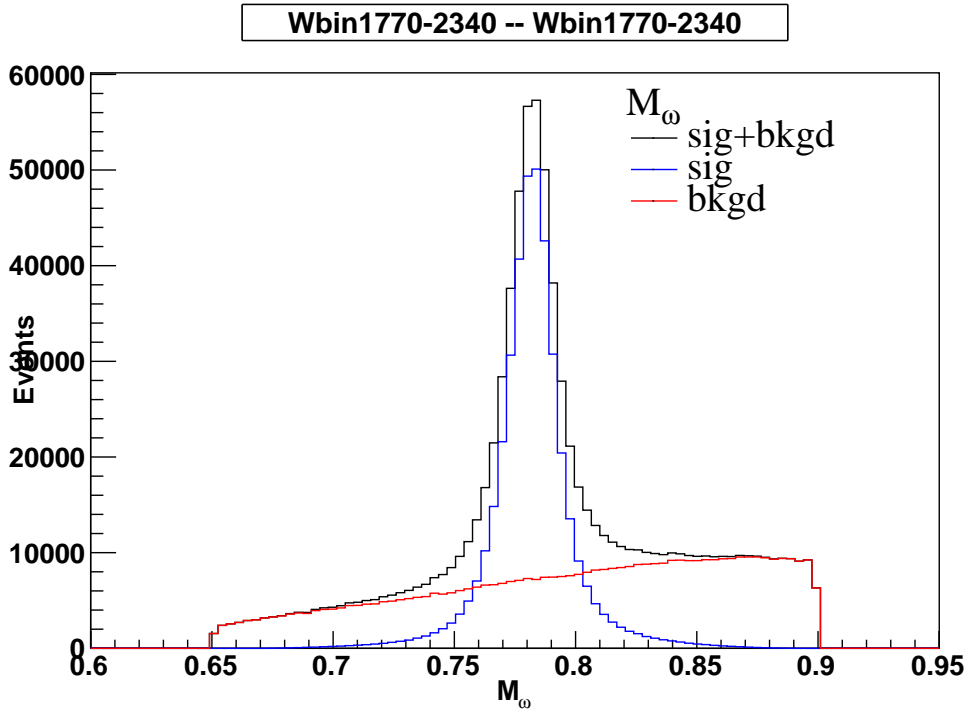


Figure 1.9: The (background separated)  $\omega$  mass,  $M_\omega$ , distribution from CLAS-g8b data for  $W : [1770 - 2340]$  MeV

Table 1.3: CLAS-g12 and CLAS-g8b data sample event counts

Data Type	CLAS-g12 events	CLAS-g8b events
Data	$\sim 8,500,000$	$\sim 900,000$
Generated M.C.	$\sim 200,000,000$	$\sim 600,000$
Detector Accepted M.C.	$\sim 20,000,000$	$\sim 60,000$

ated with the detector geometry (support structure) and software inefficiencies. The determined efficiency value was used to determine the actual count of  $\omega$  resonances produced from the target-incident photons. More information about the data reconstruction, kinematic fitting, background separation, and detector acceptance is provided in Chapters 3 - 4. The sample event counts for the CLAS-g12 and CLAS-g8b data sets are presented in Table 1.3.

# CHAPTER 2

## THE CLAS-g12 EXPERIMENT

This chapter contains a brief overview of the CLAS-g12 experiment which held its run-period during the summer of 2008. Herein, details are provided about the primary instruments used to obtain the  $\omega$  event data used in my analysis, chiefly: the accelerator, the photon tagging system, and the target and the final-state detection components of CLAS. In my analysis, in addition to extracting results from the high statistics CLAS-g12 data, I also extracted results for the purposes of comparison from on hand CLAS-g8b sample data which was obtained by our group from the earlier CLAS-g8b experiment. The CLAS-g8b experiment which had a summer 2005 run-period was quite similar to the CLAS-g12 experiment aside from the following three important differences: photon beam polarization, beam current, and target placement within relation to the center of CLAS. The run conditions for both experiments which include these differences are summarized in the last section of this chapter.

### 2.1 The Experiment Facilities

The Thomas Jefferson National Accelerator Laboratory (TJNAF or JLab for short), located in Newport News, Virginia, is home to the Continuous Electron Beam Accelerator Facility (CEBAF) and four nearby detection sub-facilities, detector “Halls” A, B, C, and D (see Fig. 2.1). The primary mission statement of JLab is to study the atomic nucleus, its fundamental constituents, and precise tests of their interactions (paraphrased) [40]. In practice, the scope of the mission statement encompasses the more general study of the fundamental constituents of baryons and mesons, collectively hadrons, as precision tests of their interactions provide the broadest supportive feedback about the atomic nucleus.

During the summer 2005 and summer 2008 experimental run-periods, the detector CEBAF Large Acceptance Spectrometer (CLAS) which was housed in Hall B had detected the data used in my analysis. As its name suggests, the accelerator facility CEBAF produces a semi-continuous beam of electrons. The detector CLAS was built for high acceptance, nearly  $4\pi$  angular cover-



Figure 2.1: An aerial view of CEBAF and its detector halls (2014) [39]

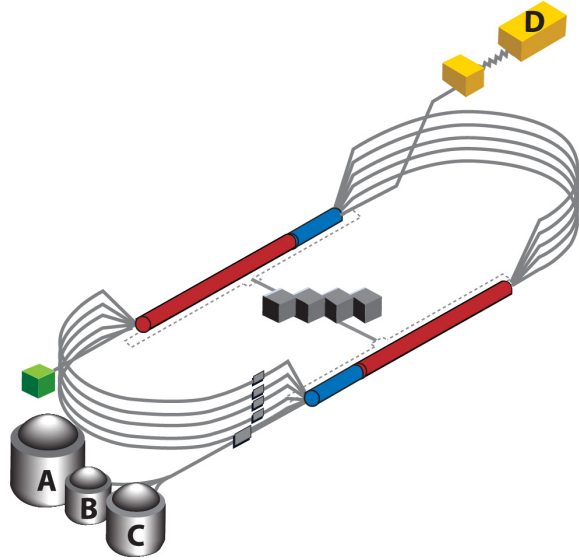


Figure 2.2: A schematic diagram of CEBAF and its detector halls post the 12 GeV upgrades [41]

age, detection of decay products which originate from either electron- or photon-induced nuclear reactions. Furthermore, while CLAS was constructed with the study of baryon resonances of primary interest, this run-period took advantage of a recently increased beam energy to obtain high acceptance data on photo-produced, light vector meson resonances.

## 2.2 The Accelerator

In brief, all experiments start with electrons being emitted from the injector site into the acceleration path of the accelerator, see Fig. 2.2. Here a system of lasers were used to photo-eject electrons from a GaAs photocathode [42]. The potential difference between the cathode and anode give the electrons an initial acceleration of 100 keV towards the accelerator beamline, and they are further accelerated to 40 – 80 MeV along their path to the first linear accelerator (LINAC).

Once along the accelerator beam path, the electrons begin to traverse the roughly  $7/8^{\text{th}}$  mile long accelerator ring. One path around the accelerator ring consists of entering and being accel-



Figure 2.3: A 5 cell cryostat cavity [43]

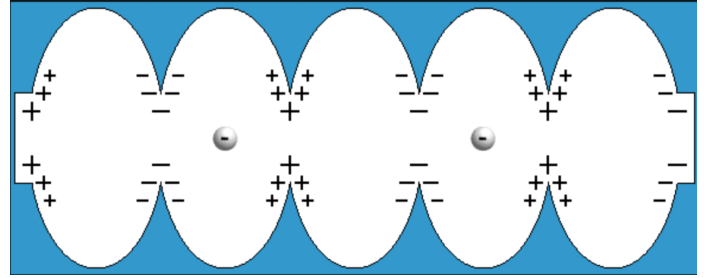


Figure 2.4: A schematic illustration of the RF controlled induced dipole across a 5 cell cryostat cavity [44]

erated through the North LINAC, entering and being steered through a  $180^\circ$  Recirculating Arc, entering and being accelerated through the South LINAC, and entering and being steered again through the opposite  $180^\circ$  Recirculating Arc. The recirculating arcs are composed of dipole magnets and each wing contains several arcs each of which correspond to a different kinetic energy sets (associated with laps around the ring) of the electrons. The electrons may make up to 5 passes around the ring thereby reaching a facility rated maximum kinetic energy before diversion towards their selected experimental detector hall.

The original (pre-12 GeV Upgrade) LINACS, shown in red in Fig. 2.2, comprise a row of 168 radio-frequency (RF) cavities which are made of superconducting niobium and maintained at a temperature of  $2^\circ$  Kelvin by a liquid Helium bath. For illustration, a 5 cell cryostat acceleration cavity along with a schematic representation of the induced electric dipoles across the cavities are shown in Figs. 2.3 and 2.4, respectively. As consequence to the induced electric dipoles, a sequence of near resistanceless electromagnetic waves span the adjacent RF cavities. Moreover, these electric dipoles are RF tuned to provide the electrons a series of increasing acceleration boosts on through the LINAC, obtaining an approximately 600 MeV energy boost overall. Thus, the electrons gain about 1.2 GeV in energy in one pass around the track (two LINACS) and up to 6 MeV after five passes around the track.

These electron bunches may be split into as many as three independent beam currents, allowing electron bunches separated by 2.004 ns, the so-called RF timing bucket, to be delivered to any one

of up to three experimental detector Halls at once. During the g12 run period, an electron beam was deliverable to Hall B of up to 5.7 GeV in energy, 75% in electron beam polarization, and was selected for a 10 – 100 nA beam current.

## 2.3 Photon Tagging System

For the CLAS-g12 experiment, the nuclear excited states of primary interest were photo- not electron-induced. The illustration of Hall B in Fig. 2.5 shows the arrangement of the so-called Bremsstrahlung (Photon) Tagging System ("Photon Tagger") upstream from the detector CLAS. It is within the Photon Tagger, Fig. 2.6, that an energy-tagged photon beam from the entering electrons was obtained. As the electron bunches encountered the system, they immediately impinged upon and penetrated the radiator which was a thin piece of gold foil (the radiator). As the electrons decelerated through the foil, they radiated photons, i.e. the process known as Bremsstrahlung radiation. The photons continued forth down-stream through a collimator before reaching the target with the detector CLAS. The bunches of electrons which entered the radiator share a flight-time coincidence with the corresponding bunch of photons leaving the radiator. The so-called "timing-bucket" is a reference used to describe a particular timing window spanned by the electron- or photon-bunches as they travel. Thus, the 2.004 ns timing-bucket spanning a particular bunch of electrons also corresponds with a timing-bucket for the target-bound bremsstrahlung radiated photons.

The electrons continued forth as well but instead followed diverted trajectories induced by dipole-magnets. The unaffected electrons which retained their full beam-energy followed a maximum trajectory leading to the beam dump. The decelerated electrons followed deflected and energy-dependent paths towards two independent planes of energy deposit and time counters (scintillators), so-called E- and T-counters, respectively. The E-counters measured the electron energy to within 1% resolution, and the T-counters measured the electron timing to within 300 ps resolution. The RF timing bucket information of the originating incoming electron beam along with the E- and T-counter information of the decelerated electrons yielded enough information to determine and "tag" the target-bound real photons with both their energies and timing upon leaving the radiator. The photon tagger was able to tag photons between 20 – 95% of the maximum electron beam energy which corresponded to  $E_\gamma \in [1.2 - 5.4]$  GeV given the CEBAF beam energy [47].

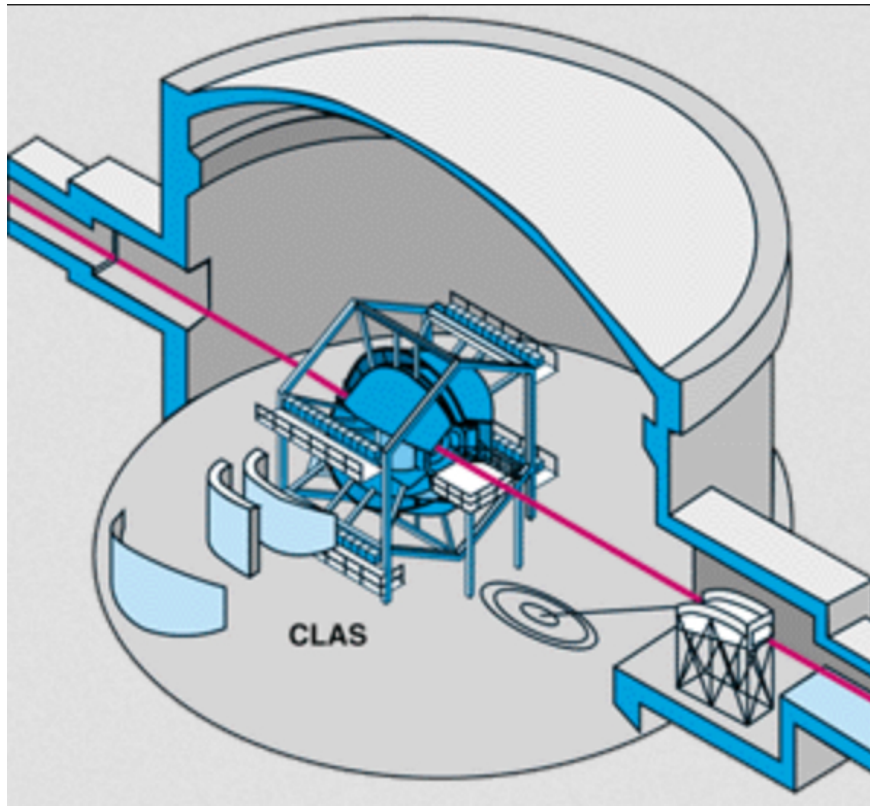
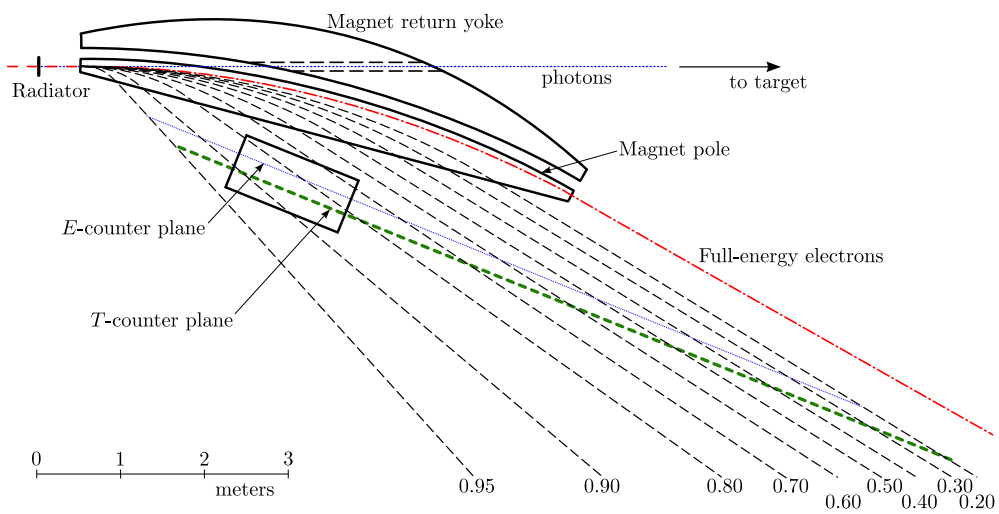


Figure 2.5: A schematic diagram of Hall B with the Photon Tagging System (upper-left) shown upstream from the target and center of CLAS [45]



p

Figure 2.6: A schematic diagram of CLAS Photon Tagging System [46]

## 2.4 The Detector

Beginning with the center of CLAS, Figs. 2.7 and 2.8, and moving outward, its multiple layers are listed as follows: a scintillator start counter (ST), three drift chamber (DC) regions with a toroidal magnet surrounding the second DC, a gas Čerenkov counter (CC), a scintillator time-of-flight (TOF) spectrometer, and finally an electromagnetic calorimeter (EC). The ST and TOF counters as well as the DCs and toroidal magnet respectively provided the speed and momentum measurements of the charged particles. By extrapolating the tracks and timing from the ST back to the target, the event vertex and occurrence time could be estimated. The CC and EC were not used in the CLAS-g12 experiment. When used in other CLAS experiments, they resolved the energy of the scattered electrons from electro-induced interactions. Respectively they aided in differentiating electrons from charged pions as well as recorded energy deposits from electrons (leptons), photon, and neutron showers.

A total of six identical concave, wall-segments (sectors) housed the DCs, Toroidal Magnet, CC, and TOF hardware layers. These segments were adjoined azimuthally around the beamline to provide the nearly  $4\pi$  center-of-mass angular coverage. The azimuthal coverage was  $360^\circ$  minus roughly  $10^\circ$  at each of the 6 structure support locations where two sectors are joined. The longitudinal lab frame coverage was  $8^\circ \leq \theta \leq 142^\circ(45^\circ)$  for charged (neutral) particles with a resolution of  $10^{-3}$  radians. The momentum detection range for charged particles was  $0.1 \leq p \leq 4.0$  GeV with resolutions of 0.5% and 1.0% at small and large angles, respectively.

### 2.4.1 Target

As the Bremsstrahlung-radiated real photons continued forth towards the target, they were collimated by a 3.1 mm radius collimator before reaching the target. Upon impact of the photons and the fixed, unpolarized, liquid-hydrogen target, Fig. 2.9, within the CLAS detector, excited nuclear resonance states (events) were photo-produced and the subsequent particle decay products were detected by CLAS. Only charged decay products were recorded during the CLAS-g12 experiment.

The Kapton (a type of polyimide film) target casing was 40 cm long with a radius of 2 cm. Its center was placed 90 cm upstream from the CLAS center for this CLAS-g12 experiment. The idea behind the placement upstream was to increase the forward angular coverage (from  $8^\circ$  to  $6^\circ$ ) at the cost of a decrease in rear angular coverage. This provided an increased event acceptance

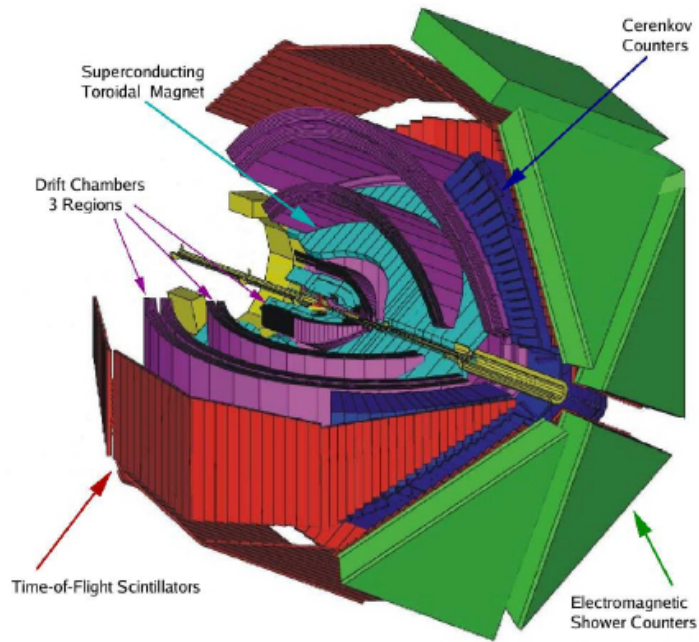


Figure 2.7: A schematic diagram of the CLAS detector [39]

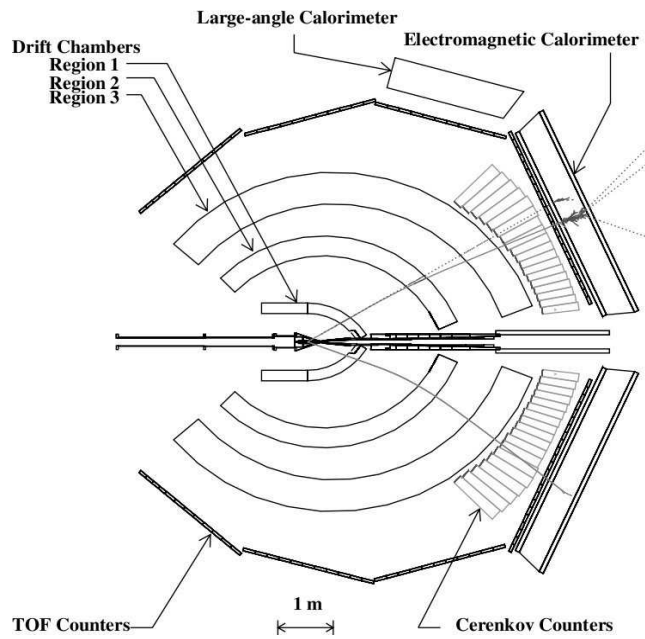


Figure 2.8: A 2D cross section sketch of the CLAS detector [46]



Figure 2.9: Schematic diagram of the CLAS-g12 (g8b, g11a) target [48]

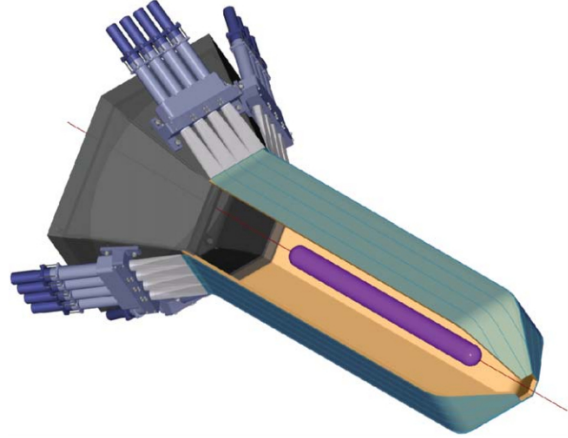


Figure 2.10: Schematic diagram of the CLAS start counter [49]

for high momentum-transfer (t-channel) scattered interactions, namely high momentum-transfer meson production.

### 2.4.2 Start Counter

The start counter (ST), Fig. 2.10, provided the initial timing information of the final state particles emanating from a photo-induced interaction event within the target. It consisted of 24 scintillators adjoining an hexagonal encasement which surrounded the target. Each of the 6 CLAS sectors was covered by 4 of the ST scintillators. Signals from the scintillators were transmitted to photo-multiplier tubes (PMT) which together yielded an overall ST timing resolution of 350 ps.

### 2.4.3 Drift Chambers

Within each of the six adjoining, concave, wall-segments of CLAS were three DC regions, Figs. 2.7 and 2.8. The DC regions were semi-radially concentric about the CLAS center and provide per sector a longitudinal and azimuthal angular coverage of  $134^\circ$  and  $50^\circ$ , respectively. The adjoining wall-segment posts were responsible for a reduction in the azimuthal coverage by about  $10^\circ$  per post, i.e. about  $60^\circ$  total. Each DC region was filled with ionizing gas (88% and 12% argon and carbon dioxide respectively) as well as both so-called field- and sense-wires [50]. In particular, each DC contains two superlayers of 6 so-called sense-wire sublayers, save Region 1 which has 4 sublayers. Each and every sense-wire was neighbored by 6 of the field-wires, see Fig. 2.11.

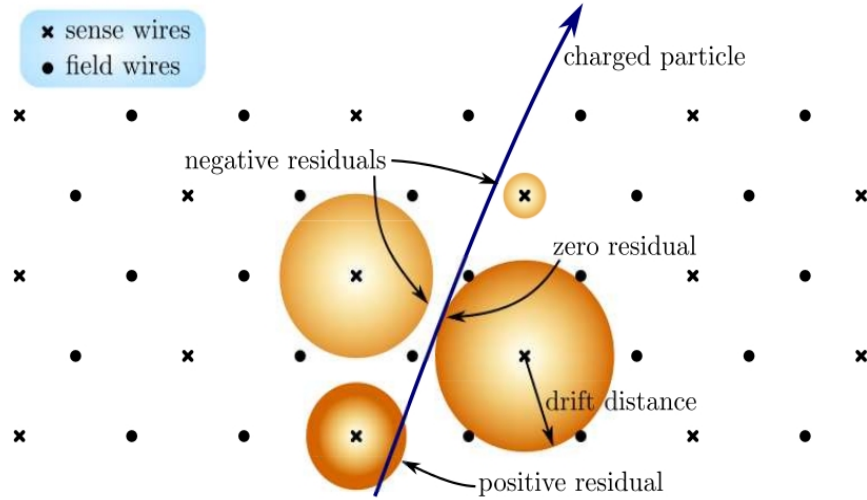


Figure 2.11: A schematic cross section diagram of the field and sense wires within a drift chamber [46]

When charged particles travel through the DCs, they ionize the gas particles along their trajectories. With the electric potentials established across neighboring sense and field wires, the freed electrons send current signals to the nearest sense wires. The signals were obtained and monitored along the paths traced out by the charged particles, thereby allowing for the reconstruction and recording of the tracks across the DCs. The recording of the tracks were dependent upon so-called trigger settings established before each run of the experiment.

#### 2.4.4 Toroidal Magnet

The purpose of the toroidal magnet, Fig. 2.12, within the CLAS was to aid with the identification of the charge and momentum of charged particles based on their deflection and traversed radius, respectively, as they travel through the Region 2 DC, see again Fig. 2.8. Within each of the 6 CLAS segments was a kidney-shaped superconducting magnet held at a temperature of 4.4° Kelvin using a liquid Helium bath. As current was run through the segments, a toroidal magnetic field was generated azimuthally about the beam line and was concentrated about the Region 2 DC. At a maximum current of 3790 A, this concentrated field was rated at a maximum of 3.5 T. The direction



Figure 2.12: The CLAS toroidal magnet during the assembly of CLAS [51]

of the field was chosen so that positively (negatively) charged particles were deflected away from (towards) the beam line. For the CLAS-g12 experiment, with negatively charged particles prone to being deflected out the beam line (end of the detector), the current was reduced and thus the field strength by about half so as to decrease the trajectory deflection and thereby increase the low angle acceptance of these particles.

#### 2.4.5 Time of Flight Counter

Following the Region 3 DC layer (see Fig. 2.8) and subsequent to the Čerenkov counter layer (not used in the CLAS-g12 experiment), there was a layer of scintillators which measure the timing of the charged final state particles. These scintillators were referred to as time of flight (TOF) counters as they measure the time at which the final state particles have reached them. The difference between the ST and TOF counters then provides the time of flight of the charged particles to traverse their paths between the two counters. This measurement along with the corresponding reconstructed track length provides a measure of the velocity of the charged particles. Additionally, the TOF provides information on the possible tracks originating from the event. The TOF counters

have a timing resolution between 80–160 ps, respectively corresponding with an increase in counter length [53]. The TOF was positioned about 5 m from the target.

#### 2.4.6 The ST and TOF

The ST and TOF counters were used along with the DC tracks in order to determine the flight-time of the charged final-state particles as they traversed through the three layers of DCs. As a charged particle traverses the gas which fills the DCs, the differential voltage signals caused by the gas ionization were transmitted to the sense-wires (detection elements) which were finely layered throughout the DCs segments. These signals allowed for reconstruction of the DC track.

Additionally, the charge of the particle could be determined from the angle of deflection the particle makes through the second DC layer; it was this DC layer of which the toroidal magnetic field surrounded and had its strongest influence on the charged particles. The ST and TOF counters as well as the DCs and toroidal magnet respectively provided the speed and momentum measurements of the charged particles.

#### 2.4.7 The CC and EC

The CC and EC were not used during the CLAS-g8b and CLAS-g12 photo-production experiments; however, they were essential for experiments using CLAS with an electron beam as they were used to detect scattered beam electrons. In particular, the CC with a determined detection efficiency of about 97% allows for  $e^\pm$  leptons and pions to be distinguished below  $\sim 2.5$  GeV, as leptons and pions have an ionization threshold of 9 MeV and 2.7 GeV, respectively. The EC consists of 8 inner and 5 outer (13 total) logical-layers which allow for distinction between leptons and pions based on energy deposits between the two (inner and outer) layers. In addition, the EC acts as a second TOF counter and energy-loss detection element which could be used for particle identification. The EC detects high-energy neutral particles such as photons, neutral pions, and neutrons. Further details about the detection, identification, and kinematics of the final-state particles, including those from the  $\omega$  decay events used in my Dalitz plot analysis presented herein, were provided in Chapters 3 - 4.

Table 2.1: Run conditions for the CLAS-g12 and CLAS-g8b experiments

Conditions	CLAS-g12	CLAS-g8b
$e^-$ Energy Beam	5.715 GeV	same
$e^-$ Current	60 – 65 nA	10 nA
Beam Polarization	Circular (up to 70%)	Linear (up to 90%)
Tagger Range	25 – 95% of $E_{e^-, max}$	same
B Field	$\frac{1}{2}B_{max}$ (1930 A)	same
Target Length	40 cm	same
Target Center	–90 cm	–20 cm
Target Material	$lH_2$	same
Target Polarization	None	same
Radiator	Gold Foil	Diamond
Radiator Thickness	$10^{-4}$ radiation lengths	50 $\mu\text{m}$
Trigger	2 – 3 charged particles	$\geq 1$ charged particle(s)

#### 2.4.8 Run Conditions

A summary of the CLAS-g8b and CLAS-g12 run conditions are provided in Table 2.1. These experimental runs took place during the summer of 2005 and summer of 2008, respectively. The main differences between the CLAS-g8b and CLAS-12 experiments were the following: the photon beam polarization type which was linear and circular, respectively; the beam current which was roughly 10 nA versus 60 nA, respectively; and the target placement with respect to the center of CLAS which was 20 cm versus 90 cm upstream, respectively. For each data set, the event samples of the differing beam polarizations were combined to obtain unpolarized samples for the respective sets. The two data sets provided two independent sources for result comparisons to be drawn.

# CHAPTER 3

## THE CLAS-g12 DATA & EVENT RECONSTRUCTION

The following chapter provides a brief description of how the CLAS-g12 data were monitored and recorded to tape by the Data Acquisition System, how event tracks and corresponding event-vertices were reconstructed, and how the charge, momentum, and particles species of the final state charge-particles were identified.

### 3.1 The Data Acquisition System & Triggers

The semi-discriminated signals (signals surpassing pre-set detector element, discriminator, noise-thresholds) from the photon tagging system and CLAS were transmitted through either analog- or time-to-digital-converters (ADC or TDC, respectively) which were monitored by the so-called Data Acquisition System (DAQ). Based on pre-run user-defined “trigger settings”, the DAQ stored the trigger-selected digital event-information into so-called BOS formatted data banks.

Moreover, these trigger settings were user-defined logic-based hardware and/or software settings monitored by DAQ. They may be adjusted per-run to require the DAQ to monitored and record select signal thresholds (e.g. quantity of particle tracks detected and timing coincidence windows) of interest by the run-group, for example, events which only contain at least three charged-particle tracks with one track per sector (so-called three-track events).

During the g12 run-period, either of two types of primary trigger conditions were implemented: One case recorded two-track events with a tagger cut on the incoming photon energy below 3.6 GeV; and the other case, recorded three-track events with no cut on incoming photon energy. The resulting incoming photon energy ranges were 3.6–5.4 GeV and 1.15–5.4 GeV, respectively. These were implemented as coincidences between the ST, TOF, and an OR logic unit (called the master-OR MOR) between the first 25 of 47 paddles of the tagger. Lastly, all CLAS subsystems (save the DCs) acquired signals within a few nanoseconds, the interval or gate for a trigger coincidence was 100 ns, and the system recorded events satisfying any of the trigger definitions at a rate of 8 kHz.

## 3.2 Track and Event Vertex Reconstruction

With the DAQ stored data (BOS formatted data banks) in hand, reconstruction of the events began with the aid of the reconstruction program called a1c (see CLAS-g12 Analysis Note for further details). This program used CLAS geometry parameters and calibration constants along with the digitized data to reconstruct the beam-based event timing (from the tagging system), charged particle tracking and momentum measurements, event-vertex fitting, and particle identification.

If and when there was a timing coincidence found between the ST and TOF within a sector was the so-called track reconstruction trigger condition met. Upon such a coincidence, the charged-particle drift chamber (DC) paths (tracks) were reconstructed through the use of a series of software algorithms. For each DC within the triggered segment, the traversing charged particle ionized the drift chamber gas. The neighboring sense wires which hold a potential difference themselves and so-called field wires transmitted the current where upon its registered by software. Regions with multiple neighboring “hits” were identified as clusters which were then sequentially linked to one another within and across each DC thus establishing a potential track path.

The links were further extrapolated towards the TOF panel where attempts were made to link the potential track path to a coincident TOF hit and thus also determine an upper time for the track end. With the TOF in hand, the linked clusters making up the DC tracks were kept or rejected based on whether or not they proceeded one another in a forward time sequence, starting and ending with the ST and TOF panels respectively. The process of re-fitting the track was repeated several times in order to increase the accuracy of the track path and DC flight-time measurements.

Lastly, attempts were made to reconstruct the event vertex by linking (within the target volume) the pre-estimated final-state charged-particle vertex location and time with those values separately determined for the initial state photon. First, the paths of two or more time-coincident charged-particle tracks (each from a different sector) were extrapolated back to the target from the ST using the distance of closest approach (DOCA) to the photon beam line. The midpoint between the ST and beam line was defined as the vertex of the particle, and the midpoint between the single particle vertices defines the event vertex.

Using the individual DC track speeds along with the respective track distances as measured between the corresponding ST counter location and the DOCA to the target, a track vertex-time was estimated for each track. The average of these times was obtained and referred to as the averaged ST

vertex-time. The track speeds were obtained simply from dividing the DC track lengths and track flight-times as measured between the ST counter and TOF counter distance and time differences, respectively (i.e.  $\beta_{DC} \approx \beta_{ST-TOF} = (l_{TOF} - l_{ST})/c (t_{TOF} - t_{ST})$ ). The photon vertex-time was determined from the photon-tagging system T-counters and the RF timing. Finally, reconstruction of the event vertex was established if a time-coincidence was found between the averaged ST vertex-time and a photon vertex-time. The coincidence was met if the difference between the two times fell within the 2 ns of the beam bucket.

### 3.3 Particle Identification

The identity of the charged final state particles were determined from collectively identifying their corresponding charge, speed, and momentum. The charge of the particle was determined from the direction of deflection of the track due to the magnetic field. As a charged particle penetrated the Region 2 DC within its sector, the toroidal magnetic field induced positively (negatively) charged particles to be deflected away from (towards) the beam line, see Fig. 2.8. As previously mentioned, the speed of each particle was determined from the total track length and flight-time measurements from the ST to TOF counter, i.e.  $\beta_{ST-TOF} = (l_{TOF} - l_{ST})/c (t_{TOF} - t_{ST})$ .

The momentum of the charged particles was determined from the radius of curvature of the tracks and the toroidal magnetic field strength within the respective sectors of the Region 2 DC. The two quantities were related through the relation  $p = qBr$  as well as  $p \sim qBl^2/(2s)$  where  $q$  is the assumed charge,  $e$ , for the particle,  $B$  is the magnetic field strength,  $r$  is the radius of trajectory curvature,  $l$  is half the chord length, and  $s$  is the sagitta; the second relation is an approximation for  $s \ll r$ .

With the momentum and the timing measurements, the rough mass of the particle was calculated using  $m = p/(\beta\gamma)$ . With the rough mass, an attempt to infer the particle identity was made. An algorithm compared the calculated mass to a list of mass-ranges which correspond to pre-identified DC mass ranges for an assortment of known particles. The events with particles having calculated masses outside the listed ranges were discarded as poorly reconstructed events. For the events having masses that fell within the listed ranges, the charged particles were given an particle identification number (PID) associated with the “book” mass value, i.e. the measured mass listed by the Particle Data Group.

## CHAPTER 4

# EVENT SELECTION, KINEMATIC FITTING, CUTS, & THE Q-VALUE METHOD

The following chapter discusses many of the final tasks required to prepare the data events, namely the  $\gamma p \rightarrow p \omega \rightarrow p \pi^+ \pi^- \{\pi^0\}$  reaction events, used in my  $\omega$  decay analysis. These procedures involve event selection, kinematic fitting, kinematic cuts, and signal-background separation using the Q-value method. The last section discusses Monte Carlo generation and simulation of detector accepted events. Together these sets of Monte Carlo events provide a means for acceptance correcting the data.

### 4.1 Final-State Event Selection

There are two dominant branching ratios for the  $\omega$  vector meson decay: one, the decay into the three-pion final-state  $\omega \rightarrow \pi^+ \pi^- \pi^0$  which happens roughly 89% of the time; and two, the decay into the one-pion and photon final-state  $\omega \rightarrow \pi^0 \gamma$ , which happens roughly 8.6% of the time. With the desire of having a high-statistics  $\omega$  event sample for analysis, data events from the former reaction type were sought from the CLAS-g12 reconstructed BOS data banks.

Moreover, since CLAS does not detect final-state neutral particles (neutrals) as indicated with the parentheses in the reaction above, reconstructed events with the final-state  $p \pi^+ \pi^-$  were selected as the possible  $\omega$  resonance candidates. A kinematic fit procedure, as described in the next section, was used to restore the missing neutral pion,  $\{\pi^0\}$ , to the final-state of each event,  $\gamma p \rightarrow p \pi^+ \pi^- \{\pi^0\}$ . Thus, this was our final state event selection criteria when drawing data events from the CLAS-g12 reconstructed BOS data banks.

### 4.2 Kinematic Fitting

In order to improve the event kinematics measurements after reconstruction, a kinematic fitting procedure was applied to the data. The kinematic fitting program used was developed by Dustin Keller [54]. It employs the method of Lagrange multipliers to impose supplied physical constraints,

such as energy-momentum conservation, on the event kinematics, and the method of least squares is used for the overall fitting. The fitter was supplied with an error correlation (covariance) matrix which contains the drift chamber (DC) track resolution uncertainties. In addition, unaccounted for energy, momentum, vertex position inefficiencies incurred in part due to track reconstruction inefficiencies and uncertainties were included. Energy losses, for example, due to path interference from various detector materials (e.g. the target and start counter (ST)), and multiple scattering effects [55] were also accounted for in the covariance matrix parameter space. During DC track reconstruction, an error covariance (or correlation) matrix is obtained. This matrix was used as an input in the kinematic fitter. The event kinematics were successively improved as the iterative fitting procedure minimized the correlation parameters spanning energy, momentum, vertex position inefficiencies. The tracking error correlation matrix was included. It was constructed from resolution uncertainties and parameters which were used for fitting the correlations between uncertainties during track reconstruction.

A set of  $n$  measured quantities  $\vec{\eta}$  may be expressed generally as a sum of their respective “true” values,  $\vec{\eta}'$ , plus the deviation errors (from the observed measurements),  $\vec{\epsilon}$ , such that

$$\vec{\eta} = \vec{\eta}' + \vec{\epsilon} \quad (4.1)$$

Moreover, a set of  $r$  general equations of constraint may be expressed as,

$$f_k(\vec{x}, \vec{\eta}) = 0, \quad \text{for } k = 1, 2, \dots, r \quad (4.2)$$

and where the set of  $m$  unknown parameters,  $\vec{x}$ , are related to the set of  $n$  true values  $\vec{\eta}'$  through the equations of constraint.

For the method of Lagrange multipliers, a general expression (Lagrangian) written in terms of the covariance matrix is minimized [54]. The method of least squares minimizes the sum of the squared differences between predicted and measured values. For the case of independent measurements, this reduces to minimizing the familiar  $\chi^2$  expression,

$$\chi^2 = \sum_i \left( \frac{\epsilon_i}{\sqrt{\sigma_{\eta_i}}} \right)^2 = \sum_i \left( \frac{\eta_i - \eta'_i}{\sqrt{\sigma_{\eta_i}}} \right)^2 \quad (4.3)$$

The quality of the fit error was examined by observing so-called pull distributions for each kinematical quantity fit. The  $i$ th pull distribution is given by

$$z_i = \frac{\epsilon_i}{\sigma_{\epsilon_i}} = \frac{\eta_i - \eta'_f}{\sqrt{\sigma_{\eta_i}^2 - \sigma_{\eta_f}^2}}, \quad (4.4)$$

where  $\eta_i$  is the. Moreover, as close as possible, the distributions ought to be normally distributed about zero and have a  $\sigma = 1$ .

The confidence level provides a goodness-of-fit test of the fitted event kinematics. It is expressed as

$$CL = \int_{\chi^2}^{\infty} f(z, n) dz \quad (4.5)$$

where  $f(z, n)$  is the  $\chi^2$  probability density function of  $n$  degrees of freedom. In particular, it is a measure of the probability that the  $\chi^2$  from the theoretical distribution is larger than that determined from the fit. The CL is flat on the interval (0,1] for events which satisfy the fit hypothesis, whereas it peaks near 0 for events which do not satisfy the hypothesis. For this reason, many background events may be eliminated from the signal events (at the cost of losing a much smaller amount of signal events) by making a low CL cut. Often a CL cut of either 0.01, 0.05, or 0.1 may be chosen depending upon how many signal events are being cut from the sample. In my analysis, I used a CL cut of 0.1.

The pull distributions may also be used to assess the quality of the fit as well (not just the quality of the fitted errors). If there are systematic errors with the measurements, a pull distribution may be shifted from or broadened (consistent underestimate) or narrowed (consistent overestimate) around the zero-point of the distribution as a result [56].

### 4.3 Photon Selection and Kinematic Cuts

This section touches on some additional corrections made to the data in the form of cuts. These cuts aimed to eliminate both non-physical as well as poorly reconstructed events; consequently, the cuts resulted in an additional reduction in background events from the data. The following cuts were employed to the data: photon selection cut, vertex cut, and a  $\Delta\beta$  cut. Despite having “cleaned-up” the data quite a bit and having removed much of the background events from the data sample, some background will remain among the signal events. A brief description is provided about an

event-based method which addresses the problem. In short, this method further distinguishes the remaining data in terms of the likeliness of each and every event having originated from signal as opposed to background.

Photon selection involved matching-up the final-state particles of an event with the photon that caused the event. In order to do this, the event vertex-times were compared. A time coincidence was sought between the photon vertex-time as determined from the tagging system and the averaged ST vertex-time as determined for the final-state particles. Moreover, since multiple photons were Bremsstrahlung radiated for a given electron bunch, these photons continued forth to the target area within the same 2.004 ns time interval or “timing bucket”. Furthermore, cases arise where more than one photon may satisfy the vertex-time coincidence. As such, there is an ambiguity surrounding which photon caused the event and which photon ought to be selected. From our g12-data for the  $\omega$  resonance, it was estimated that about 17% of our events had at least two photon candidates which could have caused the event. In these cases, the photons are often chosen at random or the events are thrown out. As a result, any subsequently determined observables, such as the cross section, using the data must account for this loss of data through statistical correction(s).

The event vertex cut eliminates events which originate outside of the target volume and somewhere within the surrounding support structure. The liquid-hydrogen target had a 2 cm radius and was 40 cm in length. The placement of the target was 90 cm upstream from the CLAS center; this was done in order to increase the acceptance in the forward direction for high-energy scattering events during the g12 runs. The tracking resolution was 5 mm and 6 mm in the radial and z direction respectively. In the end, event vertices were restricted to lie within a radius of 2.5 cm (allowing some room for the track resolution) and between the upstream z-axis coordinates (−110 cm, −70 cm).

The timing cut or  $\beta$  cut removes potential events with superluminal track speeds, and the  $\Delta\beta$  cut removes potential events where the determined  $\beta$  values, one by TOF and the other through momentum and identified mass (PID), differ from one another by a chosen threshold. The thresholds in both cases were chosen with the timing resolution of CLAS in mind. For our data, the cuts applied were  $\beta_{TOF} \leq 0.04$  and  $\Delta\beta = |\beta_{TOF} - \beta_{PID}| \leq 3\sigma$ . Lastly, during the CLAS-g12 run period, the efficiency of several TOF paddles were either quite poor or called into question. By “knocking

out” these paddles, we effectively remove any and all events with track hits associated with these effectively dead paddles.

## 4.4 The Q-Value Method

Despite having reduced the background from signal events through various corrections and cuts, there will be background events which have remained inseparable from the signal events. An effective way to further separate the signal from background events is through the so-called Q-value method. The Q-value method is an event-based method devised for extracting a signal-to-background quality factor (Q-value) for each sample event while also preserving the multi-dimensional kinematic correlations of the sample. These Q-values are ideal for use with unbinned, event based fits as terms for individual events may be weighted with more or less signal importance. In particular, the Q-values are weight factors valued between 0 and 1, and they represent whether an event is more or less likely to be a signal event (closer to 1) as opposed to being a background event (closer to 0) [57].

The dynamics of the photoproduced  $\omega$  and its subsequent three-body decay, i.e.  $\gamma p \rightarrow p\omega \rightarrow p\pi^+\pi^-\pi^0$ , may be described by 5 degrees of freedom (d.o.f.), namely 2 for the production and 3 for the decay, as is generally true for three-body decays. Given a data sample of  $N$  such events, we then choose the following kinematic variables for our 5 d.o.f: the invariant  $3\pi$  mass,  $m_i^{3\pi}$ ; the center-of-mass  $\omega$  production angle,  $\cos\theta_{cm}^\omega$ ; the normalized squared decay plane normal,

$$\begin{aligned} \lambda &= \frac{|\vec{p}_{\pi^+} \times \vec{p}_{\pi^-}|^2}{\lambda_{max}} = \frac{|\vec{p}_{\pi^+} \times \vec{p}_{\pi^-}|^2}{|\vec{p}_{\pi^+}|^2 |\vec{p}_{\pi^-}|^2 \sin^2(120^\circ)} \\ &= \frac{|\vec{p}_{\pi^+} \times \vec{p}_{\pi^-}|^2}{\frac{1}{108}(M_\omega^2 - 9m_{\pi_{mean}}^2)^2}, \end{aligned} \quad (4.6)$$

given in terms of the pion momenta in the  $\omega$  rest frame; and the decay angles,  $\cos(\theta_{Adair})$  and  $\phi_{Adair}$ , given relative to the decay plane normal as chosen in the Adair frame (see Fig. 4.1).

For the Adair-coordinate system, the orientation of the z-coordinate axis is chosen to lie along the direction of the photon beam direction in the overall center-of-mass (c.m.) frame. Also, the y-coordinate axis is chosen to lie normal to the production plane where the cross-product of the incoming photon beam direction,  $\hat{k}$ , is taken with the direction of the outgoing  $\omega$  meson,  $\hat{q}$ , in the overall c.m. frame, i.e.  $\hat{y} = \hat{n} = \hat{k} \times \hat{q}$ . The x-coordinate axis is then simply given by  $\hat{x} = \hat{y} \times \hat{k}$ .

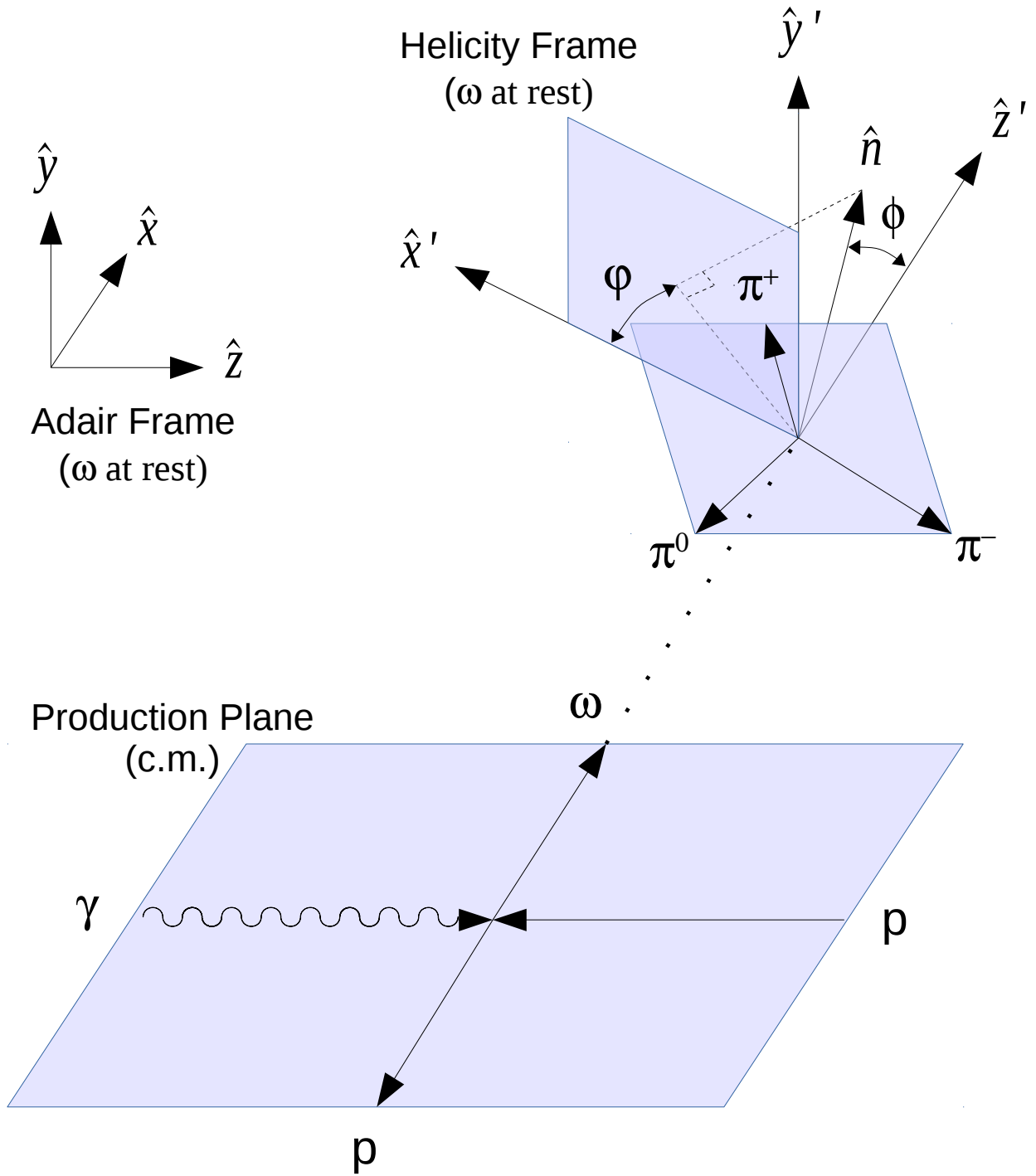


Figure 4.1: Helicity and Adair frame comparison

Lastly, the decay angles in the Adair-frame (Adair-angles) are determined through the following relations between these Adair-frame coordinates and the normal-coordinate of the decay plane,  $\hat{\pi}$ , which is defined in the  $\omega$  rest-frame as the absolute value of cross product between any two of the three pion directions, e.g.  $\hat{\pi} \propto |\hat{\pi}^+ \times \hat{\pi}^-|$ :

$$\cos(\theta) = \hat{\pi} \cdot \hat{z} \qquad \cos(\phi) = \frac{\hat{y} \cdot (\hat{z} \times \hat{\pi})}{|\hat{z} \times \hat{\pi}|} \qquad \sin(\phi) = \frac{-\hat{x} \cdot (\hat{z} \times \hat{\pi})}{|\hat{z} \times \hat{\pi}|}$$

Using these last three relations, the decay angles may be also be determined in relation to the Helicity and Gottfried-Jackson frames where the choice of z-coordinate axis serves as the defining characteristic that distinguishes the three systems from one another, i.e. the direction of the incoming photon in the c.m.-frame and  $\omega$  rest-frame, respectively.

The signal distribution,  $\mathcal{S}$  is defined as

$$S(m, \vec{x}) = F_s(\vec{x}) V(m, \mu, \sigma, \Gamma), \quad (4.7)$$

where  $F_s(\vec{x})$  is an unknown general expression dependent on the kinematic set

$$\vec{x} = (\cos \theta_{cm}^\omega, \lambda, \cos \theta_{Adair}, \phi_{Adair}), \quad (4.8)$$

and  $V(m, \mu, \sigma, \Gamma)$  is a Voigtian function (a convolution of a Gaussian with width  $\sigma$  and a non-relativistic Breit-Wigner of width  $\Gamma$ ) given by

$$V(m, \mu, \sigma, \Gamma) = \frac{1}{\sqrt{2\pi}\sigma} \text{Real} \left[ w \left( \frac{1}{2\sqrt{\sigma}}(m - \mu) + i \frac{\Gamma}{2\sqrt{2}\sigma} \right) \right] \quad (4.9)$$

where  $w(z)$  is the complex error function. Additionally, the background distribution may be written generally as  $\mathcal{B}(m, \vec{x})$  but its functional form is unknown. In terms of the spanned kinematic space  $\vec{x}$ , the shortest kinematic distance between any two events is given by

$$d_{ij}^2 = \sum_{k=1}^4 \left( \frac{\xi_k^i - \xi_k^j}{r_k} \right)^2, \quad (4.10)$$

where the metric used is a  $4 \times 4$  matrix defined by  $\delta_{ij}/r_i^2$  with  $\vec{r} = (2, 1, 2, 2\pi)$  giving the ranges of  $\vec{\xi}$ .

From the data event sample,  $N$ , for each  $i$ th event with mass  $m_i$  and kinematics  $\vec{\xi}_i$ ,  $N_{nn}$  kinematically nearest neighboring events (“nearest neighbors”), are found using Eqn. 4.10. Since

the phase space of the nearest neighbors,  $N_{nn}$ , is close to that of the event of interest, i.e.  $\vec{\xi}_j \approx \vec{\xi}_i$ , the signal and background functions of each event may be approximated as follows:

$$S(m_j, \vec{\alpha}_j) = F_s(\vec{\alpha}_i) V(m_j, \mu, \sigma, \Gamma) \approx A \cdot V(m_j, \mu, \sigma, \Gamma), \quad (4.11)$$

$$S(m_j, \vec{\alpha}_j) = S(m_j, \vec{\alpha}_j) \approx am_j + b, \quad (4.12)$$

where the background in the mass distribution is known to have a linear or low degree polynomial trend.

An event-based, unbinned maximum likelihood method is then used to fit the signal and background to the nearest neighbors sample,  $N_{nn}$ , and thus obtain the corresponding parameter set  $\eta_i(A_i, a_i, b_i)$  for that  $i$ th event. The quality factor (Q-value) for each event is then obtained in terms of the fitted signal and background functions by

$$Q_i = \frac{S_i}{S_i + B_i}, \quad (4.13)$$

where  $0 \leq Q_i \leq 1$ . As mentioned, each Q-value represents the likeliness of the corresponding event being a signal event as opposed to a background event.

## 4.5 Detector Efficiency Simulation and Data Acceptance Correction

As with all real detectors, they are not “perfect” detectors, and so the true number of “naturally occurring” sample events produced in the detector is unknown. The real detector has no way of assessing the number of events it could have detected but did not detect. These detection inefficiencies are associated with the support structure of the detector, broken hardware, and software failures. However, a good estimate of the detection efficiency fortunately can be obtained through the use of generated Monte Carlo events (MCs) and model simulation of their acceptance by CLAS. With the detector efficiency estimated, an estimate of the true number of photo-produced  $\omega$  events that a “perfect” detector would have detected was obtained. Furthermore, both the differential cross section used in my analysis as well as the partial-wave analysis itself rely on a high statistical estimate of the CLAS efficiency.

Two sets of MCs were prepared to determine the detector efficiency, so-called generated or raw MCs and so-called detector accepted or detector simulated MCs. Several programs available from

the CLAS repository were used to generate both sets of MCs. With respect to one another, the second set is simply the first one after having run detector acceptance simulations (and the same kinematic fitting and cuts as applied to the data) on them. Moreover, the detector efficiency was then obtained by comparing a ratio of the two sample counts from the same kinematic regions, e.g. center of mass production energy,  $E_{cm}$ , or  $\omega$  production angle,  $\cos\theta_{cm}^\omega$ . Lastly, while both sets of events respect their kinematic boundaries by definition of Monte Carlo generation, they are of course absent much physical content such as the event production and decay dynamics. As discussed in Chapter 6, some physics may be included and generated into the detector accepted MCs through weights, namely they may be weighted with the differential production cross section and Schilling Equation to mimic the production and angular decay distribution dynamics respectively.

Monte Carlo events for the  $\gamma p \rightarrow p\omega \rightarrow p\pi^+\pi^-\pi^0$  reaction were generated with a flat phase space, i.e. absent production or decay dynamics natural to the real data. The incoming photons were generated according to a Bremsstrahlung distribution of energies ranging between 1.5 to 5.4 GeV. Along with the particle masses, the natural decay width [8] for the invariant  $\omega$  mass resonance was included. The program used is called `genr8`. The event output is written in the so-called `gamp` file format. From the `gamp` files, two different paths are taken to obtain the two sets of MCs mentioned above. Using the program `gamp2root`, these so-called “raw” generated Monte Carlo events with a flat (no physics save the  $\omega$  resonance width) phase space distribution are readily obtained in ROOT format.

The ROOT format is standard event file format used for storing our data events as well as Monte Carlo event sets. The ROOT program is an object-oriented platform predominantly used by the particle physics communities for data analysis. The development of the framework was born from the desire to upgrade and integrate CERN particle physics libraries originally written in FORTRAN into modern object-oriented C++ class structures. Thus, the ROOT file format and program provide a convenient way to store, read, and display event information. The programs used in calculating the differential cross section and/or performing the partial-wave analysis directly read the events from this format.

Following the prescription outlined in the CLAS-g12 analysis note (see [cite] for more details), we continue the development process for obtaining the simulated CLAS-accepted MCs. After event generation, the raw MCs (`gamp` files) are fed into the program `gamp2part` which then smears the

generated target distribution to mimic a natural (physical) target distribution. The MCs (BOS part formatted files) are fed through the program GSIM which simulates the digital detection of such events in terms of ideal CLAS responses. Thus, for example, the events are expressed in terms of CLAS digitized DC hits similar to signals obtained from real events. The GSIM package is based on the GEANT3 detector simulation libraries developed by CERN. The output (BOS banks formatted files) is then passed through the GSIM Post-Processor program, GPP, which removes events which encountered dead DC wires and dead SC paddles. GPP incorporates simulated tracking resolution effects which are based on measurements obtained for the real data from the g12-run period. The events are passed through the a1c program which reconstructs the digitally simulated events in a similar manner to that performed for CLAS signals of real events. Finally, the detector simulated events are kinematically fit in the same manner as the real data events, and thus the CLAS accepted Monte Carlo event set has been obtained. With these two Monte Carlo event sets now obtained, generated MCs and CLAS accepted MCs, the simulated CLAS efficiency can be determined for common regions of kinematical phase space.

# CHAPTER 5

## PARTIAL WAVE ANALYSIS

In this analysis, a mass independent fit is performed following a variation of the unbinned, event-based, Maximum Likelihood Method (MLM). The MLM is based on maximizing the Likelihood function,  $\mathcal{L}$ , a product of individual probabilities of respective event occurrences,

$$\mathcal{L} \equiv \prod_i^n \mathcal{P}(\vec{x}, X_i), \quad (5.1)$$

where the product is over  $n$  total sample events and the probabilities,  $\mathcal{P}$ , are general functions of the parameters (estimators),  $\vec{x}$ , and event phase space kinematics,  $X_i$ . Maximizing the Likelihood,  $\mathcal{L}$ , in turn maximizes the individual event occurrence probabilities. In quantum mechanics, this is equivalent to maximizing individual normalized transition probability densities, e.g.  $\mathcal{P} \propto \mathcal{I}(\vec{x}, X_i)$  where  $\mathcal{I}$  is the intensity distribution per event occurrence. Additionally, under the assumption that the individual event occurrences are uncorrelated and thus the event sample is Poisson distributed, maximizing the following product is referred to as Extended Maximum Likelihood Method (EMLM),

$$\mathcal{L} \equiv \left( \frac{\bar{n}^n}{n!} e^{-\bar{n}} \right) \prod_i^n \mathcal{P}(\vec{x}, X_i), \quad (5.2)$$

where the factor within parentheses represents the Poisson distribution of obtaining  $n$  sample events from a distribution of  $\bar{n}$  expected events. Lastly, as it is computationally advantageous to sum instead of multiply a large number of event probabilities, one may minimize the logarithm of the extended likelihood function,  $-\ln(\mathcal{L})$ , which is referred to as the Log Likelihood Method (LLM).

In all cases, it is the intensity distribution,  $\mathcal{I}$ , which serves as the fit function of these unbinned, event-based, likelihood fits. In the following sections, it is the aim to show how this intensity function may be constructed in terms of partial wave helicity states following the method of [59], how spin-parity conservation leads to a special factorization feature for Dalitz plot distributions, what are the key features of these intensity distribution factors, and most importantly how they are represented and accounted for in this analysis.

Rather than extract partial wave states corresponding to the exchange mechanism underlying the photo-production of the  $\omega$  resonance, the focus of this analysis was on extracting information about the  $\omega \rightarrow 3\pi$  decay amplitude. In order to properly account for the acceptance of the detector, however, the Log Likelihood method requires fitting the overall (production and decay) intensity function. The measured differential cross section was therefore substituted for the squared decay amplitude, i.e.  $d\sigma/d\cos\theta_{c.m.}^\omega \propto |\mathcal{T}|^2$ , in the overall intensity function.

The squared decay amplitude contribution will be shown to factorize further into decay-angle-dependent and -independent parts. The former is a product of Wigner D functions referred to as the so-called angular decay distribution. This factor represents the angular decay distribution of the vector meson decay products. Also, it is associated with so-called spin density matrix elements (SDMEs) of the intermediate vector mesons. These SDMEs are in turn correlated through the production amplitudes with the photon beam spin density states. The squared dynamics amplitude is angle-independent and is associated with the dynamics of the resonance decay into its decay products.

The dynamic three-body decay model used in my analysis was developed by the Joint Physics Analysis Center (JPAC) at JLab and is discussed in the last section of this chapter. Its construction is of the dispersive and relativistic covariant framework. It is based on isobar decomposition and sub-energy unitarity and accounts for so-called elastic and inelastic rescattering effects. The latter contributions are unknown and novelly separated and parameterized from the former in terms of a power series of a suitably mapped variable. In this analysis, a single decay parameter suffices for the parameterization. The results of the SDMEs and JPAC  $\omega \rightarrow 3\pi$  decay parameter are presented in Chapter 6.

## 5.1 The Intensity Distribution

While ultimately interested in the dynamics of the  $\omega \rightarrow 3\pi$  decay and therefore in fitting the dynamical contribution of the decay amplitude with the data, the event-based fitting method used in my analysis requires the consideration of the overall intensity distribution, i.e. the vector meson photo-production on through to the decay final state. This is a requirement of this method in order to properly account for the CLAS (detector) acceptance. In terms of amplitudes, the full intensity

takes the form,

$$\mathcal{I}(\vec{x}, X) = \sum_{\alpha} \left| \sum_{\beta} \mathcal{V}_{\alpha\beta}(\vec{x}, X) \mathcal{A}_{\alpha\beta}(\vec{x}, X) \right|^2 \quad (5.3)$$

where  $\mathcal{V}_{\alpha\beta}$  is the production amplitude,  $\mathcal{A}_{\alpha\beta}$  is the decay amplitude, the sums over the general indices  $\alpha$  and  $\beta$  represent an incoherent and coherent sum over the amplitudes,  $\vec{x}$  represents a set of parameters (estimators), and  $X$  represents phase space kinematics for the event.

In this section, following the method of [59], we set out to formulate the overall intensity distribution in terms of helicity states. We begin with a three particle system of definite total angular momentum and parity which is built from single particle helicity states in the system rest frame [60, 61, 62, 63]. From here, general decay and production amplitudes in the helicity basis are developed. The spin-density distribution of the incoming photon beam is then introduced. Next, an integration over an Euler angle yields that (for Dalitz plot analyses) the squared reduced decay amplitude factorizes from angular decay distribution. Lastly, the intensity distribution for this Dalitz plot analysis is procured.

For general relativistic treatments, the so-called spinor helicity method may be used as an alternative; however, the treatments of states with three or more particle are quite complicated and cumbersome, especially when the masses are not neglected [62]. It is argued that the non-relativistic and relativistic treatments at least for the  $\omega \rightarrow 3\pi$  decay are equivalent in the rest frame of the decaying  $\omega$  resonance [63]. Thus, for purposes of motivating the origination and identification of the overall fit function factors used in my fits, I have stuck to a pedantic introduction using the non-relativistic (resonance rest frame) formalism. In terms of the final fit function, a seamless substitution of the generic non-relativistic reduced decay amplitude for the relativistic JPAC reduced decay amplitude (both chosen in the  $\omega$  rest frame) is made.

### 5.1.1 Rest Frame Helicity States

We follow the work of [62] for a straightforward and clear derivation of a non-relativistic one particle helicity state of definite total angular momentum. Such helicity states are comprised of simultaneous eigenstates  $\vec{J}^2$ ,  $J_z$ ,  $\vec{S}^2$ , and  $\Lambda$  where the first three operators are the standard canonical states and the fourth operator, a scalar and thus a commuting operator, is the so-called helicity operator. These helicity states form a convenient basis because they are invariant under

spatial rotations and forward boosts along momentum direction of the particle. They are convenient for describing relativistic scattering of both massless and massive particles [60, 61, 62, 63]. The helicity operator,  $\Lambda$ , is defined by the inner product of total angular momentum and momentum direction of the particle, namely,

$$\begin{aligned}
\Lambda &\equiv \vec{J} \cdot \hat{p} \\
&= (\vec{L} + \vec{S}) \cdot \hat{p} \\
&= (\vec{r} \times \vec{p} + \vec{S}) \cdot \hat{p} \\
&= \vec{S} \cdot \hat{p},
\end{aligned} \tag{5.4}$$

where it follows that the helicity operator amounts to the spin-projection along the momentum direction of the particle. Moreover, in the fixed-body frame of the particle, the momentum is given by  $\vec{p} = p\hat{z}$  such that  $\Lambda = \vec{J} \cdot \hat{z} = J_z = S_z$ , hence

$$J_z |p\hat{z}, \lambda\rangle = \lambda |p\hat{z}, \lambda\rangle. \tag{5.5}$$

We begin with the definition of the free one-particle helicity state of definite total angular momentum,

$$|p, jm\lambda\rangle = \sqrt{\frac{2j+1}{4\pi}} \int d\Omega \mathcal{D}_{m\lambda}^{*(j)}(\phi, \theta, -\phi) |\vec{p}, \lambda\rangle, \tag{5.6}$$

where the momentum, total angular momentum and its  $z$ -component, and rest frame helicity state of the free particle are respectively given by  $p$ ,  $j$ ,  $m$ , and  $\lambda$ . The spherical-wave helicity state (LHS) is represented by a familiar expansion of the plane-wave helicity states (RHS),  $|\vec{p}, \lambda\rangle$  (which differ from  $|p\hat{z}, \lambda\rangle$  only by a general rotation). The prefactor expression involves an angular integration over the Wigner  $D$  rotation matrix elements,

$$\begin{aligned}
\mathcal{D}_{mm'}^{(j)}(\alpha, \beta, \gamma) \delta_{jj'} &\equiv \langle jm | U[R(\alpha, \beta, \gamma)] | j'm' \rangle \\
&= \langle jm | e^{-\alpha J_z} e^{-\beta J_y} e^{-\gamma J_z} | j'm' \rangle \\
&= e^{-i\alpha m} \langle jm | e^{-\beta J_y} | j'm' \rangle e^{-i\gamma m'} \\
&= e^{-i\alpha m} d_{mm'}^j(\beta) e^{-i\gamma m'} \delta_{jj'},
\end{aligned} \tag{5.7}$$

where  $U[R(\alpha, \beta, \gamma)]$  is the unitary operator representing a general rotation about the three Euler angles (see Fig. 5.1),  $d_{mm'}^j(\beta)$  are the usual Wigner  $d$ -functions, and the convention  $R(\alpha, \beta, \gamma) \rightarrow R(\phi, \theta, -\phi)$  of [59] has been chosen.

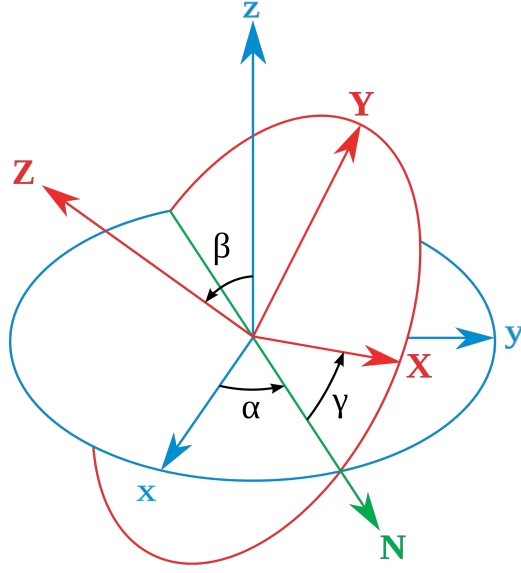


Figure 5.1: Schematic diagram of the Euler angles (Image Source: [64])

Note, since the final momentum direction,  $\hat{\mathbf{p}}$ , of a plane-wave particle may be specified by a rotation using only two angles, namely the polar and azimuthal Euler angles  $\beta$  and  $\alpha$  respectively, with respect to its original body-fixed  $z$ -axis orientation,  $\vec{\mathbf{p}} = p\hat{\mathbf{z}}$ , the additional rotation by  $\gamma$  about the new orientation,  $\hat{\mathbf{p}}$ , is arbitrary. In this analysis, we stick with the convention of [59] where the Euler angles are chosen such that  $R(\alpha, \beta, \gamma) \rightarrow R(\phi, \theta, -\phi)$ ; whereby for the sake of sticking with two angles, the result being the same as a rotation about an axis  $\hat{n} = (-\sin \phi, \cos \phi, 0)$  by the angle  $\theta$ . Therefore, the angular integration is actually over  $d\Omega \equiv d\cos \beta d\phi$  and Wigner D matrix elements of Eqn. 5.6 take the form,

$$\mathcal{D}_{mm'}^{(j)}(\phi, \theta, -\phi) \delta_{jj'} = e^{-i\phi(m-m')} d_{mm'}^j(\theta) \delta_{jj'}.$$

Finally, the expression  $\sqrt{(2j+1)/4\pi}$  simply comes from the proportionality factor between spherical harmonics and Wigner D functions,

$$Y_m^l(\theta, \phi) = \sqrt{\frac{(2l+1)}{4\pi}} \mathcal{D}_{m\lambda}^{*(l)}(\phi, \theta, \gamma), \quad (5.8)$$

where use was made of the Wigner D-function orthogonality relation (note the independence from the  $\gamma$ -angle),

$$\int d\Omega \mathcal{D}_{m\lambda}^{(j)}(\phi, \theta, -\phi) \mathcal{D}_{m'\lambda'}^{*(j')}(\phi, \theta, -\phi) = \frac{4\pi}{2j+1} \delta_{j,j'} \delta_{m,m'}. \quad (5.9)$$

Foregoing excessive details about a two-particle plane-wave state, let it suffice to say it may be conveniently defined by a general rotation of the direct product of two single particle states in the rest frame where the two momenta are equal in magnitude and back-to-back (opposite helicities) such that,

$$|\vec{p}, \lambda_1 \lambda_2\rangle = U[R(\phi, \theta, -\phi)] |p\hat{z}, \lambda_1\rangle \otimes |-p\hat{z}, \lambda_2\rangle, \quad (5.10)$$

where the helicity eigenvalue is given by

$$\vec{J} \cdot \hat{p} |\vec{p}, \lambda_1 \lambda_2\rangle = \lambda |\vec{p}, \lambda_1 \lambda_2\rangle, \quad \text{and } \lambda \equiv \lambda_1 - \lambda_2, \quad (5.11)$$

and the spherical-wave helicity state expanded in the plane-wave helicity states is given by

$$|p, jm\lambda_1\lambda_2\rangle = \sqrt{\frac{2j+1}{4\pi}} \int d\Omega \mathcal{D}_{m\lambda}^{*(j)}(\phi, \theta, -\phi) |\vec{p}, \lambda_1 \lambda_2\rangle. \quad (5.12)$$

Where the z-axis is a convenient choice for characterizing a general rotation of both a one- and a two-particle fixed-body helicity state, the decay plane normal in the system rest frame is a most convenient choice from which to characterize a general rotation of the three-particle fixed-body helicity state. The decay plane normal is then defined as the unit vector along the axial direction of any two momenta directions from the system rest frame,

$$\hat{n} = \frac{\vec{q}_1 \times \vec{q}_2}{|\vec{q}_1 \times \vec{q}_2|}. \quad (5.13)$$

Now following the theme as before, a three-particle plane-wave helicity state may be conveniently defined by a general rotation of the direct product of three single "body-fixed" particle states,

$$|\phi, \theta, -\phi; E_1, \lambda_1; E_2, \lambda_2; E_3, \lambda_3\rangle \equiv U[R(\phi, \theta, -\phi)] |\hat{n} = \hat{z}; E_1, \lambda_1; E_2, \lambda_2; E_3, \lambda_3\rangle, \quad (5.14)$$

where it is understood that the applied general rotation is made relative to the decay plane normal of the 3-particle fixed-body system.

A three-particle system helicity state with definite total angular momentum and parity (electromagnetic and strong decays) may be defined as follows:

$$|jmM; E_1, \lambda_1; E_2, \lambda_2; E_3, \lambda_3\rangle \equiv \sqrt{\frac{2j+1}{4\pi}} \int d\Omega \mathcal{D}_{mM}^{*(j)}(\phi, \theta, -\phi) |\phi, \theta, -\phi; E_1, \lambda_1; E_2, \lambda_2; E_3, \lambda_3\rangle \quad (5.15)$$

where  $j$  is again the total angular momentum of the system and the components  $m$  and  $M$  are respectively its projections along the fixed-body  $z$ -axis and decay plane normal axis,  $\hat{n}$ . Furthermore, the parity of the three particle state is given by,

$$P|jmM; E_1, \lambda_1; E_2, \lambda_2; E_3, \lambda_3\rangle = (-1)^M (-1)^{s_1-\lambda_1+s_2-\lambda_2+s_3-\lambda_3} \eta_1 \eta_2 \eta_3 |jmM; E_1, -\lambda_1; E_2, -\lambda_2; E_3, -\lambda_3\rangle, \quad (5.16)$$

where  $s_i$ ,  $\lambda_i$ , and  $\eta_i$  are the spin, helicity, and intrinsic parity of the final state particles. For a three pion final state,  $s_i = \lambda_i = 0$  and  $\eta_1 \eta_2 \eta_3 = (-1)^3 = -1$  such that

$$P|jmM; E_1, 0; E_2, 0; E_3, 0\rangle = (-1)^{M+1} |jmM; E_1, 0; E_2, 0; E_3, 0\rangle. \quad (5.17)$$

### 5.1.2 The Decay Amplitude

Next, we move to construct the decay amplitude in terms of the helicity states. For this subsection, the straight forward explanations given by [63] serve well; however, again we stick with the convention of [59] with  $R(\alpha, \beta, \gamma) \rightarrow R(\phi, \theta, -\phi)$ . Additionally, different spin-parity states are shown to not interfere for Dalitz plot analyses due to both the orthogonality of the Wigner D functions and the parity conservation symmetry relation.

With the following normalization on the plane-wave helicity states imposed,

$$\langle \phi', \theta', -\phi'; E'_i, \lambda'_i | \phi, \theta, -\phi; E_i, \lambda_i \rangle = \delta^{(2)}(R' - R) \delta(E'_1 - E_1) \delta(E'_2 - E_2) \prod_i \delta_{\lambda_i \lambda'_i}, \quad (5.18)$$

it follows from Eqns. 5.15 and 5.18 that the normalization of the spherical-wave helicity states is given by

$$\langle j'm'M'; E'_i, \lambda'_i | jmM; E_i, \lambda_i \rangle = \delta_{jj'} \delta_{mm'} \delta_{MM'} \delta(E'_1 - E_1) \delta(E'_2 - E_2) \prod_i \delta_{\lambda_i \lambda'_i}, \quad (5.19)$$

and the respective completeness relations are given as

$$\sum_{\lambda_i} \int d\Omega dE_1 dE_2 |\phi, \theta, -\phi; E_i, \lambda_i\rangle \langle \phi, \theta, -\phi; E_i, \lambda_i| = I, \quad (5.20)$$

and

$$\sum_{jmM\lambda_i} \int dE_1 dE_2 |jmM; E_i, \lambda_i\rangle \langle jmM; E_i, \lambda_i| = I. \quad (5.21)$$

The decay amplitude representing a resonance of definite total angular momentum and parity,  $J^\eta$ , decaying into three particles is given as,

$$\begin{aligned} A_{decay} &= \langle \phi, \theta, -\phi; E_i, \lambda_i | \mathcal{M} | jm \rangle \\ &= \sum_{jmM\lambda_i} \int dE_1 dE_2 \langle \phi, \theta, -\phi; E_i, \lambda_i | jmM; E_i, \lambda_i \rangle \langle jmM; E_i, \lambda_i | \mathcal{M} | jm \rangle \\ &= \sum_{jmM\lambda_i} \sqrt{\frac{2j+1}{4\pi}} \mathcal{D}_{mM}^{*(j)}(\phi, \theta, -\phi) \mathcal{F}_M^j(E_i, \lambda_i), \end{aligned} \quad (5.22)$$

where the orientation of the decay plane normal (of the three-particle system) with respect to the rest frame of the resonance is given by the angles  $(\phi, \theta, -\phi)$ , and Eqns. 5.15, 5.18, and 5.21 were used. Furthermore, the reduced decay amplitude,

$$\mathcal{F}_M^j(E_i, \lambda_i) = \langle jmM; E_i, \lambda_i | \mathcal{M} | jm \rangle, \quad (5.23)$$

is rotationally invariant (as was evident from construction), thus the decay operator  $\mathcal{M}$  is as well. Lastly, with parity conservation, the reduced decay amplitude has the following symmetry:

$$\mathcal{F}_M^j(E_i, \lambda_i) = (-1)^M (-1)^{s_1 - \lambda_1 + s_2 - \lambda_2 + s_3 - \lambda_3} \eta_1 \eta_2 \eta_3 \mathcal{F}_M^j(E_i, -\lambda_i). \quad (5.24)$$

### 5.1.3 The Production Amplitude

The Lorentz invariant transition amplitude for a two-to-two particle scattering process ( $a + b \rightarrow c + d$ ) in the center-of-mass frame may be defined in terms of the T-matrix (transition-matrix) and helicity basis by

$$(2\pi)^4 \delta^{(4)}(p_{f_1} + p_{f_2} - p_{i_1} - p_{i_2}) \mathcal{M}_{fi} = \langle p_{f_1}, \lambda_{f_1}; p_{f_2}, \lambda_{f_2} | T | p_{i_1}, \lambda_{i_1}; p_{i_2}, \lambda_{i_2} \rangle, \quad (5.25)$$

such that the two-to-two helicity amplitude may be written in the center-of-mass frame as,

$$\begin{aligned} \mathcal{M}_{fi} &= (4\pi)^2 \frac{E_{cm}}{\sqrt{|p_f||p_i|}} \langle \vec{p}_f, \lambda_{f_1} \lambda_{f_2} | T(E_{cm}) | p_i \hat{z}, \lambda_{i_1}; -p_i \hat{z}, \lambda_{i_2} \rangle \\ &= (4\pi)^2 \frac{E_{cm}}{\sqrt{|p_f||p_i|}} \mathcal{T}_{\lambda_{f_1} \lambda_{f_2} \lambda_{i_1} \lambda_{i_2}}(E_{cm}, \vec{p}_f, p_i), \end{aligned} \quad (5.26)$$

where the initial and final state momenta may be obtained in terms of the Källén triangle function,

$$\begin{aligned}\lambda(a^2, b^2, c^2) &= a^4 + b^4 + c^4 - 2a^2b^2 - 2a^2c^2 - 2b^2c^2 \\ &= (a^2 - b^2 - c^2)^2 - 4b^2c^2,\end{aligned}\tag{5.27}$$

namely  $|p_{i(f)}| = \sqrt{\lambda(E_{cm}^2, m_{1(3)}^2, m_{2(4)}^2)}/2E_{cm}$ .

Moreover, upon expanding the T-matrix elements in spherical waves,

$$\begin{aligned}\mathcal{T}_{\lambda_{f_1}\lambda_{f_2}\lambda_{i_1}\lambda_{i_2}} &= \sum_{jm} \sum_{\substack{\lambda_{f_1}\lambda_{f_2} \\ \lambda_{i_1}\lambda_{i_2}}} \langle \vec{p}_f, \lambda_{f_1}\lambda_{f_2} | p_f, jm \lambda_{f_1}\lambda_{f_2} \rangle \langle p_f, jm \lambda_{f_1}\lambda_{f_2} | T^j(E_{cm}) | p_i, jm \lambda_{i_1}\lambda_{i_2} \rangle \\ &\quad \langle p_i, jm \lambda_{i_1}\lambda_{i_2} | p_i \hat{z}, \lambda_{i_1}; -p_i \hat{z}, \lambda_{i_2} \rangle \\ &= \sum_j \sum_{\substack{\lambda_{f_1}\lambda_{f_2} \\ \lambda_{i_1}\lambda_{i_2}}} \frac{2j+1}{4\pi} \sum_m \mathcal{D}_{\lambda_i m}^{*(j)}(0, 0, 0) \mathcal{D}_{m \lambda_f}^{*(j)}(\phi, \theta, -\phi) \mathcal{T}_{\lambda_{f_1}\lambda_{f_2}\lambda_{i_1}\lambda_{i_2}}^{(j)} \\ &= \sum_j \sum_{\substack{\lambda_{f_1}\lambda_{f_2} \\ \lambda_{i_1}\lambda_{i_2}}} \frac{2j+1}{4\pi} \mathcal{D}_{\lambda_i \lambda_f}^{*(j)}(\phi, \theta, -\phi) \mathcal{T}_{\lambda_{f_1}\lambda_{f_2}\lambda_{i_1}\lambda_{i_2}}^{(j)},\end{aligned}\tag{5.28}$$

where Eqns. 5.10 and 5.12 were used along with the group property

$\mathcal{D}_{kk'}^{*(j)}(R_2 R_1) = \sum_m \mathcal{D}_{km}^{*(j)}(R_2) \mathcal{D}_{mk'}^{*(j)}(R_1)$ , again  $\lambda_{i(f)} = \lambda_{i_1(f_1)} - \lambda_{i_2(f_2)}$ , and the T-matrix helicity elements were re-expressed by

$$\mathcal{T}_{\lambda_{f_1}\lambda_{f_2}\lambda_{i_1}\lambda_{i_2}}^{(j)}(E_{cm}, p_f, p_i) = \langle p_f, jm \lambda_{f_1}\lambda_{f_2} | T^j(E_{cm}) | p_i, jm \lambda_{i_1}\lambda_{i_2} \rangle.\tag{5.29}$$

Thus, the production amplitude may be expressed in terms of helicity states as

$$\mathcal{A}_{prod} = (4\pi)^2 \frac{E_{cm}}{\sqrt{|p_f||p_i|}} \sum_j \frac{2j+1}{4\pi} \mathcal{D}_{\lambda_i \lambda_f}^{*(j)}(\phi, \theta, -\phi) \mathcal{T}_{\lambda_{f_1}\lambda_{f_2}\lambda_{i_1}\lambda_{i_2}}^{(j)}(E_{cm}, p_f, p_i).\tag{5.30}$$

Furthermore, given the general theoretical definition of the differential cross section,

$$d\sigma \equiv \frac{1}{4\sqrt{(p_{i_1} \cdot p_{i_2})^2 - m_{i_1}^2 m_{i_2}^2}} |\mathcal{M}_{fi}|^2 d\Phi_n,\tag{5.31}$$

respectively a product of the so-called flux-factor, the squared transition amplitude, and the n-body final state phase-space factor, the differential cross-section for the two-to-two scattering process in

the center-of-mass frame may be obtained as follows:

$$\begin{aligned}
d\sigma &= \frac{1}{4\sqrt{(p_{i_1} \cdot p_{i_2})^2 - m_{i_1}^2 m_{i_2}^2}} |\mathcal{M}_{fi}|^2 d\Phi_2 \\
&\stackrel{c.m.}{=} \frac{1}{4|p_i|E_{cm}} |\mathcal{M}_{fi}|^2 \left( \frac{1}{(4\pi)^2} \frac{|p_f|}{E_{cm}} d\Omega_{cm} \right) \\
&= \frac{1}{(8\pi E_{cm})^2} \frac{|p_f|}{|p_i|} |\mathcal{M}_{fi}|^2 d\Omega_{cm}, \tag{5.32}
\end{aligned}$$

or alternatively,

$$\begin{aligned}
d\sigma &= \frac{1}{4\sqrt{(p_{i_1} \cdot p_{i_2})^2 - m_{i_1}^2 m_{i_2}^2}} |\mathcal{M}_{fi}|^2 d\Phi_2 \\
&= \frac{1}{2\sqrt{(2p_{i_1} \cdot p_{i_2} + p_{i_1}^2 - m_{i_1}^2 + p_{i_2}^2 - m_{i_2}^2)^2 - 4m_{i_1}^2 m_{i_2}^2}} |\mathcal{M}_{fi}|^2 d\Phi_2 \\
&= \frac{1}{2\sqrt{[(p_{i_1} + p_{i_2})^2 - m_{i_1}^2 - m_{i_2}^2]^2 - 4m_{i_1}^2 m_{i_2}^2}} |\mathcal{M}_{fi}|^2 d\Phi_2 \\
&\stackrel{c.m.}{=} \frac{1}{2\sqrt{\lambda(E_{cm}^2, m_{i_1}^2, m_{i_2}^2)}} |\mathcal{M}_{fi}|^2 \left( \frac{1}{(4\pi)^2} \frac{|p_f|}{E_{cm}} d\Omega_{cm} \right) \\
&= \frac{1}{2\beta_{12}E_{cm}^2} \frac{1}{(4\pi)^2} \frac{\beta_{34}}{2} |\mathcal{M}_{fi}|^2 d\Omega_{cm} \\
&= \frac{1}{(8\pi E_{cm})^2} \frac{\beta_{34}}{\beta_{12}} |\mathcal{M}_{fi}|^2 d\Omega_{cm}, \tag{5.33}
\end{aligned}$$

where  $|p_{i(f)}| = E_{cm}\beta_{12(34)}/2$  and  $\beta_{12(34)} \equiv \sqrt{\lambda_{12(34)}/E_{cm}^2}$  were used.

#### 5.1.4 The Full Intensity and SDMEs

Additionally, the production and decay amplitudes may be coupled through a sum over the common helicity states of the intermediate vector meson resonance. Using Eqns. 5.22 and 5.30, the transition helicity amplitude for a two-to-two resonance production followed by a resonance three-body decay as in this analysis, is given by

$$\begin{aligned}
\mathcal{M}_{fi} &= (4\pi)^2 \frac{E_{cm}}{\sqrt{|p_f||p_i|}} \sum_m \langle \phi, \theta, -\phi; E_i, \lambda_i | \mathcal{M} | jm \rangle \langle \vec{p}_f, \lambda_{f_1} m | T(E_{cm}) | p_i \hat{z}, \lambda_{i_1}; -p_i \hat{z}, \lambda_{i_2} \rangle \\
&= (4\pi)^2 \frac{E_{cm}}{\sqrt{|p_f||p_i|}} \sum_{jmM} \sum_{\substack{\lambda_{f_1} m \\ \lambda_{i_1} \lambda_{i_2}}} \frac{2j+1}{4\pi} \mathcal{D}_{\lambda_i \lambda_f}^{*(j)}(\phi, \theta, -\phi) \mathcal{T}_{\lambda_{f_1} m \lambda_{i_1} \lambda_{i_2}}^{(j)}(E_{cm}, \vec{p}_f, p_i) \\
&\quad \sum_{\lambda_i} \sqrt{\frac{2j+1}{4\pi}} \mathcal{D}_{mM}^{*(j)}(\phi, \theta, -\phi) \mathcal{F}_M^j(E_i, \lambda_i), \tag{5.34}
\end{aligned}$$

where  $\lambda_{f_2} = m$  is the resonance helicity from the center-of-mass production plane.

Summing over the spin states, the squared transition helicity amplitude becomes,

$$\sum_{spins} |\mathcal{M}|^2 \propto \sum_{mm'} \sum_{\lambda_i} \langle \phi, \theta, -\phi; E_i, \lambda_i | \mathcal{M} | jm \rangle \rho_{mm'}^j \langle jm' | \mathcal{M}^\dagger | \phi, \theta, -\phi; E_i, \lambda_i \rangle, \quad (5.35)$$

where the spin density matrix elements (SDMEs) of the resonance,  $\rho_{mm'}^j$ , have been introduced (in the helicity basis) and are assumed independent of the resonance mass [63]. The resonance SDMEs are in turn given in terms of the production helicity amplitudes and incoming particle SDMEs,

$$\rho_{mm'}^j \propto \int d\Omega_0 \sum_{\substack{\lambda_{f_2} \lambda_{i_1} \lambda_{i_2} \\ \lambda'_{f_2} \lambda'_{i_1} \lambda'_{i_2}}} \langle \vec{p}_f, \lambda_{f_1} m | T(E_{cm}) | p_i \hat{z}, \lambda_{i_1}; -p_i \hat{z}, \lambda_{i_2} \rangle \rho_{\lambda_{i_1}, \lambda'_{i_1}} \rho_{\lambda_{i_2}, \lambda'_{i_2}} \\ \langle p_i \hat{z}, \lambda'_{i_1}; -p_i \hat{z}, \lambda'_{i_2} | T^\dagger(E_{cm}) | \vec{p}_f, \lambda'_{f_1} m' \rangle, \quad (5.36)$$

where the incoming polarization states of the beam and target are handled within their respective SDME sums. For example, the familiar 1/2 factors are appropriately accounted for here when averaging over incoming polarization states for an unpolarized beam and target, respectively. Moreover, it has been made apparent the SDMEs of the resonance are in fact correlated with the spin states (SDMEs) of the incoming particles through a helicity summed product with the production amplitude helicity states. For example, as with this analysis, the vector meson SDMEs for photo-production off an unpolarized fixed target proton where the recoil particle spin is unobserved may be compactly expressed as  $\rho_{mm'}(V) = [T\rho(\gamma)T^\dagger]_{mm'}$ .

Lastly this subsection follows up with the differential cross section and so-called angular decay distribution for a two-to-two resonance production followed by a resonance decay to a three-body final state ( $a + b \rightarrow c + d \rightarrow c + 1 + 2 + 3$ ). The differential cross-section is given by

$$\frac{d\sigma}{dRdw dE_1 dE_2} = \frac{2j+1}{8\pi^2} \sum_{mm'} \rho_{mm'}^j \sum_{MM'} \mathcal{D}_{mM}^{*(j)}(R(\alpha, \beta, \gamma)) \mathcal{D}_{m'M'}^{(j)}(R(\alpha, \beta, \gamma)) \\ \times K(w) \sum_{\lambda_i} \mathcal{F}_M^{*(j)} \mathcal{F}_M^{(j)}, \quad (5.37)$$

where again the helicity basis SDMEs of the resonance,  $\rho_{mm'}^j$ , have been introduced with an explicit sum over the resonance polarization states. The kinematic factor,  $K(w)$ , contains the squared propagator (e.g. Breit-Wigner) pole of the decay resonances as well as the kinematics factors

arising from the phase space differential [63],

$$d\phi_4 = \frac{16}{(4\pi)^8} \frac{p_0}{E_{cm}} d\Omega_0 \{w dw dR dE_1 dE_2\}. \quad (5.38)$$

The normalized angular decay distribution is given by integrating over all but the decay angles,  $d\Omega$ ,

$$\frac{dN}{d\Omega} = \sum_{mm'} \rho_{mm'}^j \sum_M \mathcal{D}_{mM}^{*(j)}(\phi, \theta, -\phi) \mathcal{D}_{m'M}^{(j)}(\phi, \theta, -\phi) g_M^j, \quad (5.39)$$

where the squared, reduced-decay-amplitude factors are given by

$$g_M^j = \int dw dE_1 dE_2 K(w) \sum_{\lambda_i} |\mathcal{F}_M^j(E_i, \lambda_i)|^2. \quad (5.40)$$

Note, the sum on  $M$  runs over  $2j + 1$ , indicating up to as many couplings. The distribution is normalized when  $\int d\Omega dN/d\Omega = 1$  thus requiring  $\sum_m \rho_{mm}^j = 1$  and  $\sum_M g_M^j = 1$ . It is the normalized event (vector meson decay) distribution with respect to the orientation of the decay plane normal relative to the decay angles,  $d\Omega = d\cos\theta d\phi$ . In terms of the overall intensity distribution, the normalized angular decay distribution is an independent product factor with the non-normalized squared production amplitudes and squared reduced decay amplitudes,  $\mathcal{I} = |\mathcal{T}|^2 \mathcal{W} |\mathcal{F}|^2$ .

As it turns out for Dalitz plot distributions, different spin-parity states which could lead to the same final state do not interfere with one another. First, consider two resonances resonances of total angular momentum  $J_1$  and  $J_2$ . The amplitude is then given by,

$$M_{fi} \propto \sum_{m_1 M_1} \mathcal{T}_1(m_1) \mathcal{D}_{m_1 M_1}^{*(j_1)}(\phi, \theta, -\phi) \mathcal{F}_{M_1}^{j_1}(E_i, \lambda_i) + \sum_{m_2 M_2} \mathcal{T}_2(m_2) \mathcal{D}_{m_2 M_2}^{*(j_2)}(\phi, \theta, -\phi) \mathcal{F}_{M_2}^{j_2}(E_i, \lambda_i), \quad (5.41)$$

where for a Dalitz plot distribution,

$$\frac{d\sigma}{dw dE_1 dE_2} \propto \sum_{m_1 M_1 \lambda_i} |\mathcal{T}_1(m_1) \mathcal{F}_{M_1}^{j_1}(E_i, \lambda_i)|^2 + \sum_{m_2 M_2 \lambda_i} |\mathcal{T}_2(m_2) \mathcal{F}_{M_2}^{j_2}(E_i, \lambda_i)|^2, \quad (5.42)$$

the interference terms vanish upon integration over the decay angles due to the Wigner D function orthogonality relation (see Eqn. 5.9). Considering now two resonances with the same total angular momentum but different parities, the interference terms vanish,

$$\begin{aligned} \frac{d\sigma}{dw dE_1 dE_2} &\propto \sum_{mM\lambda_i} |\mathcal{T}_1(m) \mathcal{F}_M^j(E_i, \lambda_i) + \mathcal{T}_2(m) \mathcal{F}_M^j(E_i, -\lambda_i)|^2 \\ &= \sum_{mM\lambda_i} |\mathcal{T}_1(m) \mathcal{F}_M^j(E_i, \lambda_i) - \mathcal{T}_2(m) \mathcal{F}_M^j(E_i, \lambda_i)|^2 = 0, \end{aligned} \quad (5.43)$$

where in the second line the parity conservation condition (Eqn. 5.24) was used.

With the rest frame helicity formalism basics presented, e.g. rest frame helicity states and both the cross-section and angular decay distribution discussed in terms of SDMEs and helicity production and decay amplitudes, the following sections proceed with specializations of the normalized angular decay distribution and decay amplitude for the case of a vector meson decaying into three pseudoscalar mesons.

## 5.2 Schilling's Equation and Spin Density Matrix Elements

In this section, the normalized angular decay distribution and spin-density-matrix-elements (SDMEs) (see Eqns. 5.36, 5.39, and 5.40) as used in my analysis are presented following the formalism outlined by [2] which is an extension to the work of [59]. In particular, the normalized angular decay distribution is given in general for a vector meson photoproduced off an unpolarized proton target which subsequently decays into three pseudoscalar mesons and the recoil proton is unmeasured. This distribution which describes the direction of the decay plane normal relative to the production rest frame is often referred to as the Schilling equation. Moreover, the Schilling equation is a linear sum of normalized vector meson spin-density-matrix-elements (SDMEs) which depend upon and are expressed in terms of the summed product of the production helicity amplitudes and incoming beam SDMEs (polarization states). Finally, the vector meson SDMEs are projected out into the time- and space-like Pauli-matrices where different linear combinations of the projected Schilling Equations correspond to different incoming beam polarization types (unpolarized, circularly polarized, and linear polarized).

Recall that the normalized angular decay distribution is given in terms of a summed product over the helicities of the decay amplitudes with the resonance SDMEs which are in turn a summed product over the helicities of the production amplitude with the incoming particle SDMEs. Then for an unspecified beam polarization, an unpolarized target, and unmeasured recoil proton, the normalized angular decay distribution is given by,

$$\frac{dN}{d\cos\theta d\phi} \equiv W(\theta, \phi) = M\rho(V)M^\dagger = MT\rho(\gamma)T^\dagger M^\dagger, \quad (5.44)$$

$$\rho(V) = T\rho(\gamma)T^\dagger, \quad (5.45)$$

where the sums and normalizations were left implicit here. Also, since the incoming nucleon is only considered here as unpolarized, the sum over the target SDMEs, represented by  $\rho(N_t)$  (see

Eqn. 5.36), was left out (left implicit) since it accounts for the usual initial state averaged spin sum, e.g.  $\overline{\sum_{s_p} |T_{(s_p)}|^2} = (1/2) \sum_{s_p} |T_{(s_p)}|^2$  for a proton.

Explicitly, the normalized angular decay distribution above reads,

$$\mathcal{W}(\cos \theta, \phi, \rho(V)) = \frac{3}{4\pi} \sum_{\lambda_V \lambda_{V'}} \rho(V)_{\lambda_V \lambda_{V'}} \mathcal{D}_{\lambda_V 0}^{*(1)}(\phi, \theta, -\phi) \mathcal{D}_{\lambda_{V'} 0}^{(1)}(\phi, \theta, -\phi), \quad (5.46)$$

where the normalized vector meson SDMEs are given by

$$\rho(V)_{\lambda_V \lambda_{V'}} = \frac{1}{N} \sum_{\lambda_{N'} \lambda_\gamma \lambda_N \lambda_{\gamma'}} \mathcal{T}_{\lambda_V \lambda_{N'} \lambda_\gamma \lambda_N} \rho(\gamma)_{\lambda_\gamma \lambda_{\gamma'}} \mathcal{T}_{\lambda_{V'} \lambda_{N'} \lambda_\gamma \lambda_N}^*, \quad (5.47)$$

$$N = \frac{1}{2} \sum_{\lambda_V \lambda_{N'} \lambda_\gamma \lambda_N} |\mathcal{T}_{\lambda_V \lambda_{N'} \lambda_\gamma \lambda_N}|^2, \quad (5.48)$$

the Wigner D functions are

$$\begin{aligned} \mathcal{D}_{10}^{(1)}(\phi, \theta, -\phi) &= -\frac{1}{\sqrt{2}} \sin \theta e^{-i\phi}, \\ \mathcal{D}_{00}^{(1)}(\phi, \theta, -\phi) &= \cos \theta, \\ \mathcal{D}_{-10}^{(1)}(\phi, \theta, -\phi) &= \frac{1}{\sqrt{2}} \sin \theta e^{i\phi}, \end{aligned} \quad (5.49)$$

the pure state photon beam polarization density matrices are

$$\rho^{unpolarized}(\gamma) = \frac{1}{2} \begin{bmatrix} 1 & 0 \\ 0 & 1 \end{bmatrix}, \quad (5.50)$$

$$\rho^{circular+(-)}(\gamma) = \begin{bmatrix} 1 & 0 \\ 0 & 0 \end{bmatrix} \left( \begin{bmatrix} 0 & 0 \\ 0 & 1 \end{bmatrix} \right), \quad (5.51)$$

$$\rho^{linear}(\gamma) = \frac{1}{2} \begin{bmatrix} 1 & e^{-2i\Phi} \\ e^{-2i\Phi} & 1 \end{bmatrix}, \quad (5.52)$$

where  $\Phi$  is the angle between the xz production plane and the photon polarization vector,  $\epsilon = (\cos \Phi, \sin \Phi, 0)$ , and the sum over the normalized strong coupling is  $\sum_M g_M^{(1)} = 1$  (see comments following Eqn. 5.40). In terms of the overall intensity distribution then, the Schilling equation (normalized angular decay distribution) is an independent product factor with the non-normalized squared production amplitudes and squared reduced decay amplitudes,  $\mathcal{I}_{full} = |\mathcal{T}|^2 \mathcal{W}^{Sch} |\mathcal{F}|^2$  [2].

As mentioned, the beam polarizations matrices may be represented in standard form in terms of a sum of the identity matrix,  $1_{4 \times 4}$ , and Pauli-matrices,

$$\rho(\gamma) = \frac{1}{2} I + \frac{1}{2} \mathbf{P}_\gamma \cdot \boldsymbol{\sigma}, \quad (5.53)$$

where the polarization vectors,  $\mathbf{P}_\gamma$ , for an unpolarized, circularly polarized, and linear polarized beam type are respectively given by,

$$\begin{aligned}\mathbf{P}_\gamma &= 0, \\ \mathbf{P}_\gamma &= P_\gamma(0, 0, \pm 1), \\ \mathbf{P}_\gamma &= P_\gamma(-\cos 2\Phi, -\sin 2\Phi, 0),\end{aligned}\tag{5.54}$$

and  $P_\gamma$  is the measured amount of respective polarization. Consequently, it follows from Eqns. 5.44 and 5.45 that the vector meson density matrix and Schilling Equation may be respectively represented likewise as,

$$\rho(V) = \rho^0(V) + \sum_{\alpha=1}^3 P_\gamma^\alpha \rho^\alpha(V),\tag{5.55}$$

$$W(\theta, \phi, \rho(V)) = W^0(\theta, \phi, \rho^0(V)) + \sum_{\alpha=1}^3 P_\gamma^\alpha W^\alpha(\theta, \phi, \rho^\alpha(V)).\tag{5.56}$$

Finally, plugging the polarization vectors (Eqn. 5.54) into the Eqn. 5.56, the Schilling equation may be separated according to their polarization types,

$$W^{unpolarized}(\theta, \phi) = W^0(\theta, \phi, \rho^0(V))\tag{5.57}$$

$$W^{circular}^\pm(\theta, \phi) = W^0(\theta, \phi, \rho^0(V)) \pm P_\gamma W^3(\theta, \phi, \rho^3(V))\tag{5.58}$$

$$\begin{aligned}W^{linear}(\theta, \phi) &= W^0(\theta, \phi, \rho^0(V)) \\ &\quad - P_\gamma \cos 2\Phi W^1(\theta, \phi, \rho^1(V)) - P_\gamma \sin 2\Phi W^2(\theta, \phi, \rho^2(V))\end{aligned}\tag{5.59}$$

and the explicit  $W^\alpha$  terms [2] are given by

$$\begin{aligned}W^0(\theta, \phi, \rho^0(V)) &= \frac{3}{4\pi} \left( \frac{1}{2}(1 - \rho_{00}^0) + \frac{1}{2}(3\rho_{00}^0 - 1) \cos^2 \theta \right. \\ &\quad \left. - \sqrt{2}\rho_{10}^0 \sin 2\theta \cos \theta - \rho_{1-1}^0 \sin 2\theta \cos \theta \right), \\ W^1(\theta, \phi, \rho^1(V)) &= \frac{3}{4\pi} (\rho_{11}^1 \sin^2 \theta + \rho_{00}^1 \cos^2 \theta \\ &\quad - \sqrt{2}\rho_{10}^1 \sin 2\theta \cos \theta - \rho_{1-1}^1 \sin^2 \theta \cos 2\theta), \\ W^2(\theta, \phi, \rho^2(V)) &= \frac{3}{4\pi} (\sqrt{2}Im\rho_{10}^2 \sin 2\theta \sin \theta + Im\rho_{1-1}^2 \sin^2 \theta \sin 2\theta), \\ W^3(\theta, \phi, \rho^3(V)) &= \frac{3}{4\pi} (\sqrt{2}Im\rho_{10}^3 \sin 2\theta \sin \theta + Im\rho_{1-1}^3 \sin^2 \theta \sin 2\theta),\end{aligned}\tag{5.60}$$

where the matrix elements of the hermitian vector meson matrices  $\rho(\alpha)$  for  $\alpha = \{0, 1, 2, 3\}$  were reduced by parity conservation,

$$\rho_{\lambda\lambda'}^\alpha = (-1)^{\lambda-\lambda'} \rho_{-\lambda-\lambda'}^\alpha \quad \text{for } \alpha = 0, 1, \quad (5.61)$$

$$\rho_{\lambda\lambda'}^\alpha = -(-1)^{\lambda-\lambda'} \rho_{-\lambda-\lambda'}^\alpha \quad \text{for } \alpha = 2, 3. \quad (5.62)$$

Thus, specific to my analysis, for the photoproduction of the  $\omega$  vector meson off and unpolarized fixed-target proton where the outgoing (recoil) proton polarization is unobserved, the Schilling equation for an unpolarized incoming photon is given as,

$$\begin{aligned} \mathcal{W}^0(\theta, \phi, \rho_{\lambda_\omega \lambda'_\omega}^0(\omega)) \equiv & \frac{3}{4\pi} \left[ \frac{1}{2}(1 - \rho_{00}^0) + \frac{1}{2}(3\rho_{00}^0 - 1) \cos^2 \theta \right. \\ & \left. - \sqrt{2} \operatorname{Re} \rho_{10}^0 \sin 2\theta \cos \phi - \rho_{1,-1}^0 \sin^2 \theta \cos 2\phi \right], \quad (5.63) \end{aligned}$$

where the decay angles  $\theta_{adair}$ ,  $\phi_{adair}$  (orientation angles of the decay plane normal) were chosen in the so-called Adair-frame (see Fig. 4.1), and the matrix elements  $\rho_{00}^0$ ,  $\rho_{10}^0$ ,  $\rho_{1,-1}^0$  are the SDMEs of the  $\omega$  vector meson. Again, while the helicity basis subscripts of the  $\omega$  vector meson SDMEs run through  $\lambda_\omega = 0, \pm 1$ , only these three SDMEs remain due to hermiticity and parity conservation. For further details about the Adair-coordinate system, see Sec. 4.4.

### 5.3 The Differential Production Cross Section

With the Schilling equation (normalized angular decay distribution) discussed in the previous section, the additional production and angle-independent decay contributions to the overall intensity distribution,  $\mathcal{I}_{full} = |\mathcal{T}|^2 \mathcal{W}^{Sch} |\mathcal{F}|^2$ , may now be addressed. In this section, a brief discussion of the differential production cross section measurements are given. In short, these measurements are proportional to the squared production amplitude, i.e.  $d\sigma/d\Omega_{prod} \propto |\mathcal{T}|^2$ ; hence, they aid in the extraction (fitting) of the  $\omega$  vector meson SDMEs from the Schilling equation,  $\mathcal{W}^{Sch}$ , as well as the decay parameter(s) of the reduced (angle-independent) decay distribution,  $|\mathcal{F}|^2$ .

Measurements of the differential cross section for the  $\omega$  photo-production,  $\gamma p \rightarrow p\omega$ , were determined at FSU [1] using the equation,

$$\frac{d\sigma}{d\Omega} \cong \frac{N_\omega(E_{cm}, \Delta\Omega)}{\Delta\Omega n_\gamma \rho_{target} l_{target} N_A \epsilon_{acc} BR_{\omega \rightarrow \pi^+ \pi^- \pi^0}}, \quad (5.64)$$

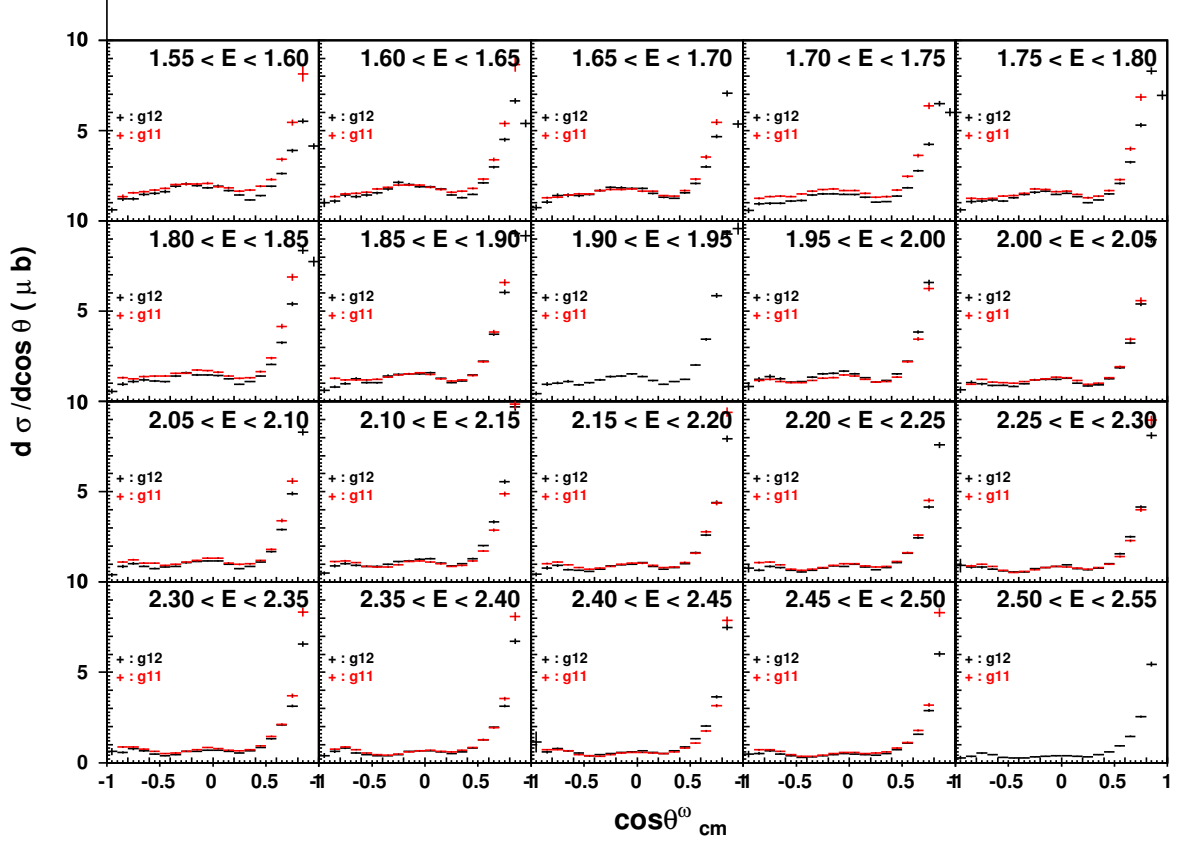


Figure 5.2:  $g_{11}$ ,  $g_{12}$   $\gamma p \rightarrow p\omega$  Differential Cross Sections,  $E_\gamma \in [1.55 - 2.55]$  MeV, Refs. [1, 7]

where  $N_\omega$  is the total number of observed  $\gamma p \rightarrow p\omega$  events,  $\Delta\Omega$  is the bin width of the production solid-angle,  $n_\gamma$  is the total number of photons on target,  $\rho$  is the density of the target,  $l$  is the length of the target, and  $N_A$  is Avogadro's Number,  $\epsilon_{acc}$  is the detector acceptance, and  $BR_{\omega \rightarrow \pi^+\pi^-\pi^0}$  is the branching ratio for the  $\omega \rightarrow \pi^+\pi^-\pi^0$  decay. In order to reduce the need for additional corrections to the reconstructed data, only runs which held the same beam current, trigger conditions, and electron polarization were used. In total, 20 – 30% of the total sample of reconstructed data was used to determine the  $\omega$  differential cross section.

Furthermore, upon inspection of the  $g_{12}$  and  $g_{11a}$  differential cross sections shown in Fig. 5.2, it may be noted that the cross section is not constant across the azimuthal center-of-mass (c.m.) production angle,  $\cos\theta_{cm}^\omega$ . For all of the incoming photon energy bins ( $E_\gamma$  in MeV), much of the cross section along the middle of the  $\cos\theta_{cm}^\omega$  range is relatively level and modest in terms of the number

of produced  $\omega$  events. This is indicative of s-channel or  $N^*$  production. Production by s-channel is where the target nucleon absorbs the incoming photon and becomes excited before its subsequent decay. Furthermore, looking towards the forward c.m. angle, there is a steep increase in the cross section. This is indicative of a large t-channel or forward scattering production. Production by t-channel is where the incoming photon scatters off the target nucleon through particle exchange, for example pseudoscalar ( $J^P = 0^-$ ) exchange. In fact, this figure demonstrates that most of the  $\omega$  events used in my analysis are produced via the t-channel. Also, since most of the  $\omega$  resonances occurred in the forward direction of the detector (near the forward hole), it was quite important for my analysis to have good simulation of the detector acceptance in this region, see Section 4.5. While the  $g_{12}$  and  $g_{11a}$  differential cross section measurements differ by roughly 5%, the former was continuing to be refined at the time of my analysis. Thus, I used the reported  $g_{11a}$  differential cross section results [7] to account for the squared production amplitude in my overall fit function.

## 5.4 The Decay Model

In this section, the  $\omega \rightarrow 3\pi$  decay model developed by the Joint Physics Analysis Center (JPAC) at JLab is presented. It takes the place of the last factor, the reduced squared decay amplitude, of the overall intensity distribution,  $\mathcal{I}_{full} = |\mathcal{T}|^2 \mathcal{W}^{Sch} |\mathcal{F}|^2$  used in my fits to the data. The model is of the dispersive variety [28, 29, 30, 31] and is based on isobar decomposition, see Fig. 5.3, and sub-energy unitarity. While the JPAC decay amplitude has been compared with that of similar models [33, 35], this was the first time this amplitude has been fit to data. The decay amplitude was developed in the covariant tensor formalism as opposed to the non-relativistic Zemach approach which I used in the introduction to motivate the core ideas behind the amplitude's ansatz construction and Dalitz plot distribution features.

The decay amplitude accounts for both elastic ( $\pi\pi - \pi\pi$ ) and inelastic (e.g.  $k\bar{k} - \pi\pi$ ) three-body rescattering effects, see Fig. 5.4. The effects of the inelastic contributions to the decay amplitude are largely unknown, they are often constrained with a fit parameter which must be determined from measured data. The unique and defining characteristic of this decay amplitude lies with the latter having been novelly separated and parameterized from the former in a power series of a suitably mapped variable. In my analysis, a single decay parameter,  $a_{JPAC}^{\omega \rightarrow 3\pi}$ , was used and sought. Further details of the JPAC  $\omega \rightarrow 3\pi$  decay model are left to Ref. [3].

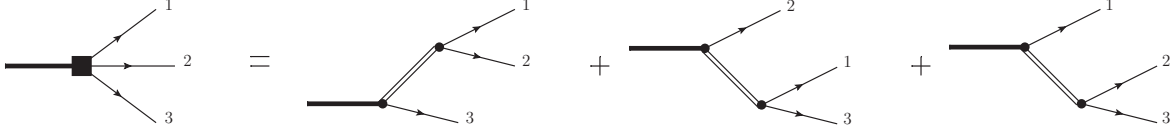


Figure 5.3: Isobar decomposition [3]

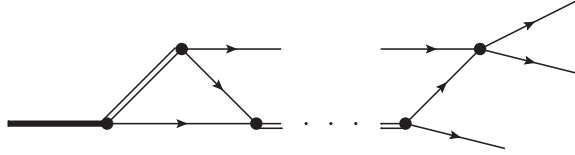


Figure 5.4: Crossed channel rescattering effects [3]

The  $\omega \rightarrow 3\pi$  decay transition matrix elements may be expressed as

$$\langle \pi^a(p_1)\pi^b(p_2)\pi^c(p_3)|T|V(p_\omega, \lambda) \rangle = (2\pi)^4 \delta(p_\omega - p_1 - p_2 - p_3) H_\lambda^{abc}. \quad (5.65)$$

The helicity decay amplitude expressed in the covariant tensor formalism is then given by

$$\mathcal{H}_\lambda^{abc} = i\epsilon_{\mu\nu\rho\sigma}\epsilon^\mu(p_\omega, \lambda) p_1^\nu p_2^\rho p_3^\sigma \frac{P_{abc}^1}{\sqrt{2}} \mathcal{F}(s, t, u), \quad (5.66)$$

where  $a$ ,  $b$ , and  $c$ , are the isospin indices,  $P_{abc}^1$  is the isospin coupling factor between the  $\omega$  and pions. The 4-momenta of the three pions are contracted with the polarization vector for the  $\omega$  meson through a totally anti-symmetric 4<sup>th</sup> rank Levi-Civita tensor leaving the expression Lorentz invariant. Since the isospin factor and spin-parity factor are each anti-symmetric, the overall helicity amplitude is symmetric as required to reflect the Bose symmetry of the system.  $\mathcal{F}(s, t, u)$  is an analytic scalar function which describes the dynamics of the decay in terms of the final-state particle-pair Mandalstam invariants,

$$s = (p_3 + p_1)^2, \quad t = (p_1 + p_2)^2, \quad u = (p_2 + p_3)^2. \quad (5.67)$$

The scalar function is free from kinematic singularities and respects a crossing symmetry such that it describes both the  $\omega \rightarrow 3\pi$  as well as the  $\omega\pi \rightarrow 2\pi$  transition processes.

Considering s-channel scattering  $\omega(p_\omega, \lambda)\pi_3^c \rightarrow \pi_1^a\pi_2^b$  in the center-of-mass frame, the momentum the incoming pion and outgoing pions may be obtained again through the use of the symmetric Källén functions

$$p(s) = \frac{\lambda^{\frac{1}{2}}(s, M_\omega^2, m_\pi^2)}{2\sqrt{s}}, \quad q(s) = \frac{\lambda^{\frac{1}{2}}(s, m_\pi^2, m_\pi^2)}{2\sqrt{s}}. \quad (5.68)$$

The s-channel scattering angle may be obtained in terms of the Mandalstam variables through

$$\cos\theta_s = \frac{t-u}{4p(s)q(s)} = \frac{t-u}{k(s)} = z_s. \quad (5.69)$$

The s-channel partial wave decomposition of the decay amplitude may be written in the x-z plane as

$$\mathcal{H}_\lambda^{abc} = \frac{P_{abc}^1}{\sqrt{2}} \sum_{j=l=1,3,\dots}^{\infty} (2j+1)d_{\lambda 0}^j(\theta_s) f_\lambda^j. \quad (5.70)$$

For the strong decay of a vector meson into three pseudoscalar (spinless) mesons, e.g.  $\omega \rightarrow 3\pi$ , the Wigner D function orthogonality condition as well as parity conservation lead to noninterference of  $J^n$  states. Consequently, only one (scalar) coupling which is proportional to the decay width (see Eqns. 5.40, 5.42, 5.43). Furthermore, Bose symmetry and parity conservation lead to odd integer values of total angular momentum and only one scalar function,  $f_0^j(s) = 0$ , and  $f_1^j(s) = -f_{-1}^j(s) \equiv f_j(s)$ .

Relating  $\mathcal{H}_\lambda^{abc}$  to  $\mathcal{F}(s, t, u)$ , the kinematic singularities in  $f_j(s)$  may be identified and factored leaving only dynamical singularities to contend with in  $\mathcal{F}(s, t, u)$ . The helicity amplitude may be re-expressed as

$$\mathcal{H}_\lambda^{abc} = -P_{abc}^1 \frac{\sqrt{\phi}}{4} \sum_{j=l=1,3,\dots}^{\infty} (p(s)q(s))^{j-1} P_j'(z_s) F_j(s), \quad (5.71)$$

where the Wigner d-functions have been written in terms of Legendre polynomial derivatives,  $P_j'(\cos\theta_s)$ , such that

$$d_{10}^j(\theta_s) = -\frac{\sin\theta_s}{\sqrt{j(j+1)}} P_j'(\cos\theta_s), \quad (5.72)$$

$F_j(s)$  is now given by,

$$F_j(s) = \frac{\sqrt{2}(2j+1)f_j(s)}{\sqrt{s}\sqrt{j(j+1)}(p(s)q(s))^j}, \quad (5.73)$$

and  $\phi = (2 \sin \theta \sqrt{s} p(s) q(s))^2 = stu - m_\pi^2 (M_\omega^2 - m_\pi^2)^2$  is the Lorentz invariant so-called Kibble boundary function. This boundary function is of the same origin of the previously discussed  $\lambda$  factor, see Eqns. 1.24 and 4.6. By inspection,

$$\mathcal{F}(s, t, u) = \sum_{j=l=1,3,\dots}^{\infty} (p(s)q(s))^{j-1} P'_j(z_s) F_j(s) \quad (5.74)$$

where the polynomial  $(p(s)q(s))^{j-1} P'_j(z_s)$  is free from kinematic singularities. Thus, only dynamical singularities must be contended with for the redefined reduced partial waves expression  $F_j(s)$ .

The infinite sum in the s-channel physical region converges, however, it is truncated with the expectation that the first few angular momentum states dominate. The other channels are obtained through an analytical continuation of the s-channel beyond the physical region on into the decay region, and they are then introduced into the overall amplitude sum. The scalar function  $\mathcal{F}(s, t, u)$  is approximated by a linear combination of the truncated partial wave series,

$$\mathcal{F}(s, t, u) = \sum_{j=l=1,3,\dots}^{\infty} (p(s)q(s))^{j-1} P'_j(z_s) F_j(s) + (s \rightarrow t) + (s \rightarrow u), \quad (5.75)$$

with the t- and u-channel scattering angles given by

$$\cos \theta_t = \frac{s-u}{4p(t)q(t)} = \frac{s-u}{k(t)} = z_t, \quad \cos \theta_u = \frac{t-s}{4p(u)q(u)} = \frac{t-s}{k(u)} = z_u. \quad (5.76)$$

The lowest angular momentum state of the partial-wave expansion is expected to dominate. Thus, only the P-wave,  $J = L = 1$  is considered. For real  $s \leq (M_\omega + m_\pi)^2$ ,  $F_{j=l=1}(s) = F(s)$  is given by

$$F(s) = \frac{1}{\pi} \int_{4m_\pi^2}^{\infty} \frac{DiscF'(s')}{s' - s - i\epsilon} ds', \quad (5.77)$$

where

$$DiscF(s) = \rho(s) t^*(s)(F(s) + \hat{F}(s)), \quad \hat{F}(s) = 3 \int_{-1}^{+1} \frac{1-z_s^2}{2} F(t(s, z_s)) dz_s. \quad (5.78)$$

where  $\rho(s)$  is the two-body phase space of the two-body  $\pi\pi - \pi\pi$  amplitude ( $\rho(s) = \sqrt{1 - 4m_\pi^2/s}$ ),  $t^*(s)$  is the two-to-two-body scattering channel associated with the  $\rho$  isobars,  $\mathcal{F}(s)$  is the direct-channel  $\omega$  decay contribution, and  $\hat{\mathcal{F}}(s')$  is the rescattered  $\pi\pi - \pi\pi$  subamplitude contribution. For the other channels, this equation must be analytically continued in  $s$  to the decay region  $4m_\pi^2 \leq s \leq (M_\omega + m_\pi)^2$ .

Upon implementation of several analytic integration techniques and inclusion of inelastic scattering contributions [3], Eqn. 5.77 becomes

$$\mathcal{F}(s) = \Omega(s) \left( \frac{1}{\pi} \int_{s_\pi}^{s_i} ds' \frac{\rho(s')t^*(s')}{\Omega^*(s')} \frac{\hat{\mathcal{F}}(s')}{s-s'} + \Sigma(s) \right), \quad (5.79)$$

where clean separation has been made of the elastic and inelastic scattering contributions, respectively the first and second terms. A conformal mapping technique was used to analytically express and parameterize the inelastic contributions via the power series expansion,

$$\Sigma(s) = \sum_{i=0}^{\infty} a_i \omega^i(s), \quad (5.80)$$

where

$$\omega^i(s) = \frac{\sqrt{s_i} - \sqrt{s_i - s}}{\sqrt{s_i} + \sqrt{s_i - s}} \quad (5.81)$$

is a conformal variable accounting for the analytic continuation of the inelastic contributions.  $\Omega(s)$  is the so-called Omnès function which contains the direct-channel contribution for the  $\omega$  decay. The parameter  $s_i$  is set equal to  $1 \text{ GeV}^2$  which is the energy where inelastic contributions are likely to start becoming significant, e.g.  $4m_K^2 \sim 0.97 \text{ GeV}^2$ .

The differential decay width is given by

$$\frac{d^2\Gamma}{dsdt} = \frac{P(s,t)|F(s,t,u)|^2}{3(2\pi)^3 32M_\omega^3}, \quad (5.82)$$

where  $P(s,t) = \phi/4$  with  $\phi$  given in Eqn. 5.71,  $F(s,t,u)$  is the full JPAC  $\omega \rightarrow 3\pi$  decay amplitude, and  $M_\omega$  is the mass of the decaying  $\omega$  resonance. Note, only one decay parameter for the power series expansion was used in my fits, i.e.

$$\Sigma(s,t,u) \sim N \left( 1 + 2 \frac{a_1}{a_0} \omega^1(s,t,u) \right) = N \left( 1 + 2a_{JPAC}^{\omega \rightarrow 3\pi} \omega^1(s,t,u) \right) \quad (5.83)$$

where all three isobar channels were included,  $a_0$  was absorbed into the overall normalization  $N$ ,  $\omega^0(s,t,u) \equiv 1$ ,  $\omega^1(s,t,u)$  for the three channels is given by Eqn. 5.81, and  $\frac{a_1}{a_0} \equiv a_{JPAC}^{\omega \rightarrow 3\pi}$ . Fig. 5.5 is an illustration of “reduced” Dalitz plot distribution comparisons between the CLAS-g12 acceptance corrected (signal) data and JPAC modelled distributions for various value selections of the JPAC  $\omega \rightarrow 3\pi$  decay parameter. These Dalitz plots distributions have been “reduced” by dividing out the kinematic factor  $\phi$ , see Eqn. 5.71. This was done in order to visualize the sole effects of the squared JPAC decay amplitude contribution in the distribution. The predicted value to be extracted from the data was roughly +8, i.e.  $a_{JPAC}^{\omega \rightarrow 3\pi} \sim +8$ .

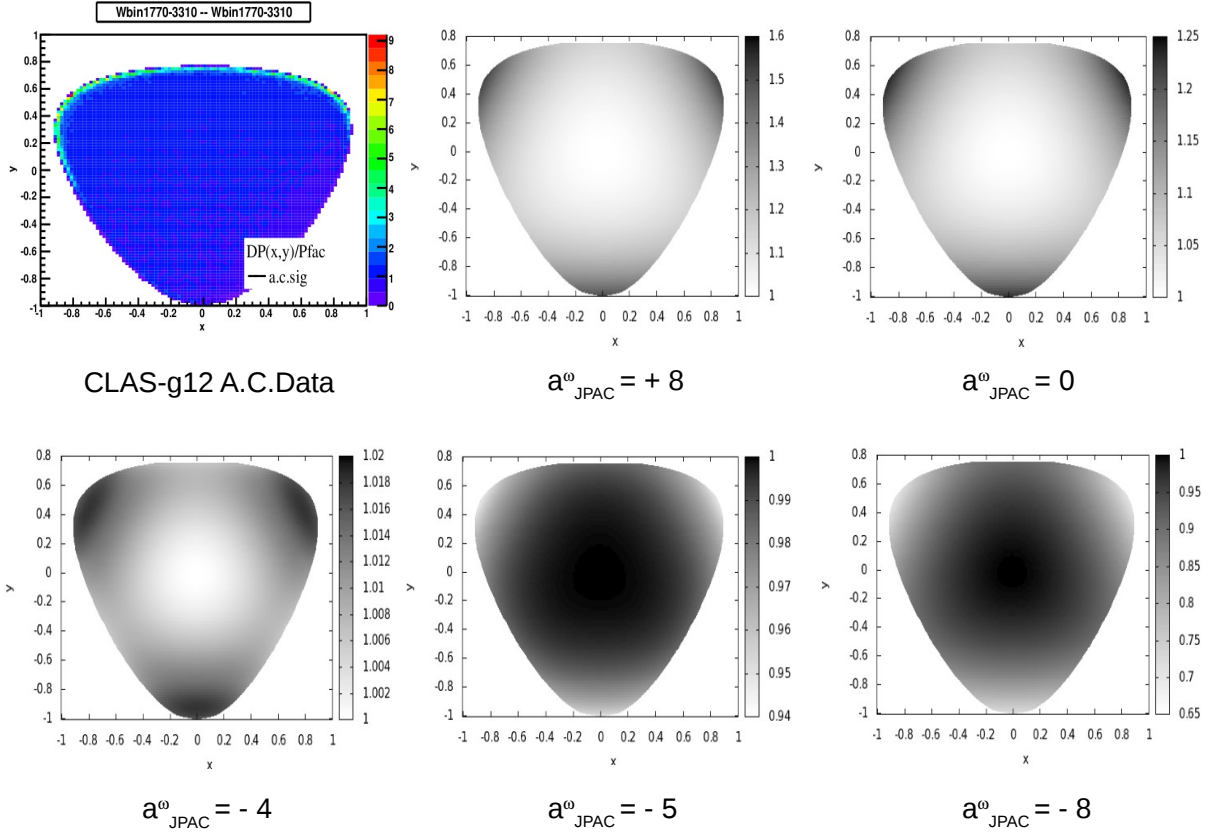


Figure 5.5: A reduced Dalitz plot distribution,  $DP(x,y)/\phi$ , comparison between the CLAS-g12 acceptance corrected (signal) data versus JPAC modelled distributions for various chosen JPAC  $\omega \rightarrow 3\pi$  decay parameter values. The decay distribution factor  $\phi$ , given in Eqn. 5.71, is divided out for the purpose of visualizing the effects of the JPAC distribution alone. The JPAC  $\omega \rightarrow 3\pi$  decay parameter was expected to be about +8, i.e.  $a_{JPAC}^{\omega \rightarrow 3\pi} \sim +8$  [65]

# CHAPTER 6

## FIT PROCEDURE AND RESULTS

Results using the two independent CLAS data sets are presented for spin density matrix elements (SDMEs) of the Schilling equation. As well, investigatory results for the JPAC decay parameter of the dynamic JPAC decay amplitude are presented using the two data sets. The latter results are first-time extractions of the decay parameter using real data. Systematic errors were not yet taken into account. A brief overview of the framework used to conduct the Dalitz plot analysis for the  $\omega \rightarrow 3\pi$  decay precedes the results.

The overview includes the fit framework set-up, framework additions, the fit method, fitter consistency and result quality checks, and the fit functions used. Some detail is provided in regards to the overall fitting and plotting process which proceeded as follows: data input formatting, data reading, amplitude fitting, result output, filling “booked” histograms, and histogram comparison-plotting.

### 6.1 Fit Framework

For my Dalitz plot analysis of the  $\omega \rightarrow 3\pi$  decay, I built up a framework of data analysis tools (a multitude of C++, ROOT, and bash scripting programs) centered around a core partial-wave analysis (PWA) software package called AmpTools, see Fig. 6.1. AmpTools was developed at Indiana University (IU) [4] and serves as an excellent event-based fitting framework. It employs the extended Log Likelihood Method (LLM) which is based on the Maximum Likelihood Method (MLM). Its internal fitting techniques utilize the widely used MINUIT (ROOT TMinuit class) routines which were originally developed at CERN [6]. This portion of the package was written at Cornell University.

#### 6.1.1 Setting Up AmpTools

The AmpTools framework consists of a series of C++ based, user-level interfaces which provide users with an organized and flexible means to utilize its core fitting and plotting software. Out of the

## “DataTools” and AmpTools Framework Schema

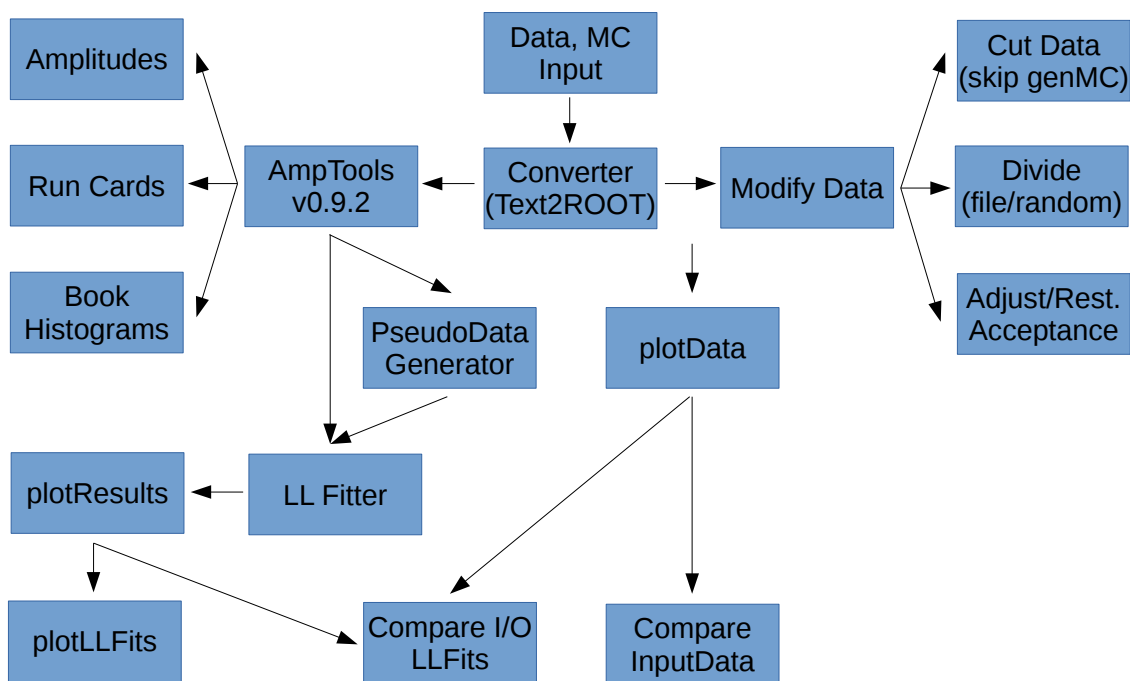


Figure 6.1: A schema of my partial-wave analysis framework

box, there are two practice PWA tutorials which allow new users to familiarize themselves with the main features of the framework as well as the user-scopes of these interfaces. Using a tutorial copy as a template, one re-tailors the user-scopes of the interfaces to meet their own process dependent and formatting needs. Depending on how you count them, there are roughly five main interfaces to edit: a data reader, a data writer, an amplitude calculator, a fit specific run-card, and a results plotter.

In brief, AmpTools reads and stores to memory the 4-momenta of the data and Monte Carlo (MC) events from separate ROOT-formatted n-tuple files, i.e. the 4-momenta of the data, raw MC, and detector simulated MC events must respectively be stored into separate (.root) files. Following the scheme illustrated in Fig. 6.1, I obtained these ROOT-formatted n-tuple files from our data text files through a “converter” (e.g. a txt2root) routine. AmpTools handles an events 4-momenta by storing them into a so-called kinematics array, and it has an option for storing and using event weights as well. My converter routine loads and stores data and MC event weights, e.g. Q-values and the differential cross section values, into ROOT n-tuples at this stage. For the purpose conserving run-time memory usage, only the event 4-momenta and weights are utilized by AmpTools. Therefore, while one may store more event kinematic quantities (event kinematics) of interest into these ROOT files for use with other routines, they won’t be accessible within the interfaces. Should any event kinematics be desired for use within one of the interfaces, one must recalculate the respective kinematics from the event 4-momenta available from the AmpTools kinematics array.

The formatting of the data reader class is to be tailored to read the event 4-momenta and weight from the respective n-tuples within the ROOT files. It is within this interface that the 4-momenta and weight for each event are stored into a kinematics array which is accessible by various routines within the AmpTools framework. For convenience, AmpTools also includes a data writer interface which may be used in conjunction with a basic phase space generator and “toy” acceptance generator to write out events for fit testing purposes. One may, however, skip the setup and use of the data writer altogether as I did if the MCs have already been obtained through other programs such as genr8 and GSIM which were mentioned in Sec. 4.5.

The amplitude interface is the so-called “CalcAmplitude()” class where an amplitude may be written out or called for example from an external link to a fortran sub-routine. Here the previ-

ously loaded event 4-momenta are accessible and desired event kinematics may be calculated. An amplitude expression may be directly derived and expressed or the event kinematics may be used in supplement to a subroutine call function. For each supplied event, the routine will then of course calculate and return the complex (real or imaginary if specified) amplitude values. Moreover, multiple complex amplitudes may be included (“registered”) at once in this manner. Whether these multiple amplitudes are needed as an overall product or a type of product sum can be specified within the run-card for the fit.

The run-card is read by the data reader. In it, foregoing specific details, the user may specify the links to the three data-type event files, set event cut flags, register the amplitude(s) to be used, initialize any amplitude parameter(s), designate different amplitude products and sums, set desired signal “switch(es)” to respective registered amplitudes, and specify the output links. After submitting a fit and upon fit convergence, the fit parameter values and their corresponding MINUIT calculated covariant error matrix are printed to a text file. One must write a set of scripts here to read in and plot these values. I used a combination of C++, ROOT, and bash scripts.

The result plotting interface must be set up. The underlying routine for this interface does not plot the fit parameter results; rather, it uses them in a manner which attempts to reproduce real event kinematic distributions from the corresponding fit-function weighted MC distributions. To set up these kinematic distributions, this interface uses the Histogram Booking method similar to that used in ROOT. Here one defines, calculates, and fills their output histograms. As of AmpTools version 0.9.0 and later, its dependence on CERN’s CLHEP libraries was removed. Thus, any and all calculations developed using ROOT libraries, e.g. for displaying kinematic distributions of the input data, may now be copied and pasted directly into this interface for immediate use.

Furthermore, the results plotting routine will produce an ROOT output file containing these kinematic distributions for both the fit-weighted MC event output and original real data event input. A program needs to be made to overlay the respective input and output distribution types for visual comparison. These comparisons are referred to as so-called “quality checks” of the corresponding Log Likelihood fit. Thus, these checks provide a further means for assessing the quality of the fit results in relation to how well they reproduce the event kinematics of the input data.

### 6.1.2 Framework Additions

In addition to getting the AmpTools framework up and running, I extended and generalized my overall data (“DataTools”) and PWA analysis framework by developing additional joint C++ and ROOT based program modules, see Fig. 6.1. Each and every routine throughout the analysis framework is “push-button” and “switch” automated through bash scripting. All routines which can utilize server job submission, e.g. currently the FSU server, are equipped to do such. Throughout the overall framework, both single and double-binned fitting with up to 5 primary and secondary bin-type selections have been enabled. The following routines were added to the framework: input and output directory creation; “text2root” data conversion with event weight options; three data modification routines; fit-function selection, fixed and random initialization, and run-card creation; pseudo-data generation with multiple consistency check options; multi-fit-function array submission options; “best” fit selection of  $N$  submitted and returned fits, and three types of plot comparison routines.

The primary and secondary bin-type selections may each be chosen from any of the following five kinematic bin-variables: the overall center-of-mass (c.m.) energy,  $\sqrt{s} = W$ ; the incoming photon lab-frame energy,  $E_\gamma$ ; the resonance mass,  $M_\omega$ ; the c.m. resonance production angle,  $\cos\theta_{cm}^\omega$ ; and the recoil momentum, Mandalstam- $t$ . The data and MC weighting options include Q-value weighting the data and both differential cross-section and/or Schilling equation weighting the detector simulated accepted MCs. I created a routine which can be used to obtain additional or supplementary weights from either histogram input or result output. The routine outputs the weights into text files which may be readily fed back into the data converter for subsequent fits.

There are three data modification routines. The cutData routine allows one to apply kinematic cuts to the events from a ROOT file. The divideData routine allows one to obtain events from an  $N^{\text{th}}$  “segment” of the ROOT file. For example, if one wanted to divide a ROOT file into 10<sup>ths</sup> and investigate only the events in the 9<sup>ths</sup> partition, this routine will extract those events from the original ROOT file. Also, the routine provides the option for randomly extracting  $N$  events from a ROOT file. The adjAcceptance routine allows one to adjust the acceptance of a set of MC files. For example, if one wants to study global event acceptance effects across a set of files binned in  $W$  at 10 MeV intervals, one can simply specify a desired acceptance to apply across the range of files. Then one can run fits using these files to see how much the fitted parameters or quality

checks change. Once investigated, a `restAcceptance` routine can be run which restores (swaps) the modified MC files back to their originals.

I modified the pseudo-data generator within the PWA framework from the original version provided with `AmpTools`. The method used behind this routine is based on the so-called acceptance-rejection method which is discussed in Sec. 6.2.1. The modifications allow one to use their MCs directly from the original ROOT files (from the data converter) as opposed to generating basic MCs from the ROOT class `TPhaseSpace`. Thus, either set of MCs (raw or detector simulated MCs) may be used to generate the pseudo-data. The accompanying bash script provides 7 options each of which pertain to obtaining and/or generating a useful data set (three data types) combination. These data sets combinations are then used as inputs to the fitter for various respective systematic checks, e.g. fitter, fit function, acceptance checks. For example, note that the fit method and fitter require the three input files which typically correspond to the following three data types: data, raw MCs, and detector simulated MCs (i.e. data, “rawMC” a.k.a. “genMC”, “simMC” a.k.a. “accMC”). However, a check on the consistency of a fitter with a particular fit function may utilize the option which creates the data set from genMC events only, i.e. `pseudodata-genMC, genMC, genMC`, where the first data-type is pseudo-data generated from genMC and the latter data-types account assume a perfect detector (no-detector effects). Another but similar option may include the detector effects which are absent from data set of the previous example, i.e. `(pseudo-data-accMC, genMC, accMC)`.

Also, I developed three separate plotting routines which collectively rendered pertinent feedback from various kinematic distribution comparisons of both the input and output events. One program, `compareInputData`, compares the input data types and acceptance corrected data. In particular, various kinematic distributions of the data are respectively presented side-by-side for the three background-signal separation (Qvalue) weight types: signal and background (no-Qvalue), signal only (Qvalue), and background only (1-Qvalue). Also, MC comparisons are presented for the distributions with and without MC-weights. Next, the program, `plotLLfits`, is simply a routine which provides side-by-side quality checks of various kinematic distributions between the signal input data and fit weighted detector simulated MCs. Additionally, the program `compareLLFitIO`, compares aspects found in both above comparison programs. Importantly, this program provides

before-fit and after-fit acceptance comparisons for various kinematic distributions, not merely global bin count acceptances. This program allows one to assess the acceptance dependence of the fits.

## 6.2 Fit Method

As mentioned in the prelude of Chapter 5, in this analysis, a mass independent fit is performed following a variation of the unbinned, event-based, Maximum Likelihood Method (MLM). This method used within AmpTools is the so-called Minimum Extended Log Likelihood Method (Minimum ELLM) or simply the Log Likelihood Method (LLM) for short. Starting from the Extended Maximum Likelihood equation,

$$\mathcal{L} \equiv \left( \frac{\bar{n}^n}{n!} e^{-\bar{n}} \right) \prod_i^n \mathcal{P}(\vec{x}, X_i), \quad (6.1)$$

$\mathcal{P}(\vec{x}, X_i)$  is the probability density or normalized intensity distribution,  $\mathcal{P} \propto \mathcal{I}$ , function representing the occurrence of an event  $i$  with parameter set  $\vec{x}$  and kinematic factors  $X_i$ ,  $\prod_i^n$  indicates a product of the probability densities over the range  $1, i, \dots, n$  is made, and the factor within parentheses represents the Poisson distribution of obtaining  $n$  sample events for an expected  $\bar{n}$  events. Thus, the Likelihood function is a product of probabilities with a range over all measured sample events. In order to account for the fact that the total number of sample events measured from a sample size  $N$  is an occurrence of probability itself, the Likelihood function is “extended” by additionally multiplying it by the Poisson distribution.

By maximizing this likelihood function, one obtains the best estimators  $\hat{x}$  for the parameters. In practice, a computationally efficient way to maximize this extended likelihood function is to actually turn the product into a sum by taking its natural log,

$$-\ln \mathcal{L} \equiv - \sum_{i=1}^{N_{data}} \ln \mathcal{I}(\vec{x}, X_i) + \frac{\mathcal{S}(s)}{N_{gen}} \sum_{j=1}^{N_{acc}} \mathcal{I}(\vec{x}, X_j) + const., \quad (6.2)$$

and instead minimize the log of the extended likelihood, the so-called Log Likelihood Method. Note, the first term on the right-hand-side of Eqn. 6.2 involves a sum of natural logarithms of the intensity function over the sample of reconstructed data events,  $n = N_{data}$ . The form of the second term which was derived from the number of expected events,  $\bar{n}$ , is proportional to the Monte Carlo simulated efficiency (acceptance) of the detector. This term involves a sum of the intensity over the accepted MC events,  $N_{acc}$  and it is normalized by the total number of generated MC events,

$N_{gen}$ . Lastly, the factor  $\mathcal{S}(s)$  is proportional to the expected event phase space. The two terms are referred to as the data log sum and Monte Carlo (MC) integral sum, respectively. Since the logarithm of the likelihood function is a monotonically increasing function, it is guaranteed that by minimizing the log-likelihood function the likelihood function is maximized. Additionally, instead of optimizing the log-likelihood function by setting its derivative to zero, the AmpTools framework fits for the best estimators of the parameter set by floating the parameter values and recalculating the log-likelihood for each adjustment until convergence to the log likelihood minima is reached.

Furthermore, AmpTools views and treats an intensity in the following way,

$$\mathcal{I}(\vec{x}, X_i) = \sum_{\alpha} \left| \sum_{\beta} \mathcal{T}_{\alpha\beta} \mathcal{M}_{\alpha\beta}(\vec{x}, X_i) \right|^2, \quad (6.3)$$

where the intensity is a function of both the production amplitudes,  $\mathcal{T}_{\alpha\beta}$ , and the decay amplitudes,  $\mathcal{M}_{\alpha\beta}(\vec{x}, X_i)$ . AmpTools treats the production amplitudes as complex fit parameters and the decay amplitudes are supplemented fit functions of the decay theory. The sums over the general  $\alpha$  and  $\beta$  indices represent incoherent and coherent sums over the amplitudes, respectively. In terms of a sum over total angular momentum states (partial-waves), the log likelihood function, Eqn. 6.2, within AmpTools takes the form

$$\begin{aligned} -2 \ln \mathcal{L} = & -2 \sum_{n=1}^{N_{data}} Q_n \ln \left| \sum_{j,j'} \mathcal{T}_j \mathcal{T}_{j'}^* \mathcal{M}_j(\vec{x}, X_n) \mathcal{M}_{j'}^*(\vec{x}, X_n) \right| \\ & + 2 \frac{1}{N_{gen}} \sum_{j,j'} \left( \mathcal{T}_j \mathcal{T}_{j'}^* \sum_{m=1}^{N_{acc}} \left| \mathcal{M}_j(\vec{x}, X_m) \mathcal{M}_{j'}^*(\vec{x}, X_m) \right| \right) + const., \end{aligned} \quad (6.4)$$

where the Q-value weights,  $Q_i$ , of the data events has been made explicit and the phase space factor  $\mathcal{S}(s)$  as shown in Eqn. 6.2 was absorbed into the production amplitudes which AmpTools treats as complex fit parameters. For finely binned fits, the corresponding change to the production amplitudes within the log term results in a mere constant shift to the overall log likelihood function. For the same reasons the phase space factor is no longer visually explicit, any MC weight factors used to weight the detector simulated MC events follow the same treatment path mentioned of the phase space factor. They are, therefore, not made explicit here either.

In particular, AmpTools starts with the calculation of the first of the two terms in Eqn. 6.4. The intensity is calculated event-by-event using the 4-momenta from the momentum n-tuple stored in the data ROOT-file. The intensity is re-calculated for each and all of the data events over and

over again for each and every adjustment made to the fit parameters by MINUIT. This iterative process is continued until either convergence of the fit is reached or the fit fails. With only one iteration needed, the intensity was calculated for each the detector-simulated MCs using the very same parameter values found from the data converged fit. Finally, the log likelihood is calculated from the two terms and printed to an output file along with the values of the fit parameters, the covariant error matrix, the integral populations of each data-type, and the detector acceptance.

While a robust goodness-of-fit criteria has been established for the binned minimum  $\chi^2$  method, it has often been the case that only relative goodness-of-fit treatments have been used for the unbinned, event-based log-likelihood method. For example, in order to reduce the likeliness that a fit has reached a local-extrema rather than the global-extrema, a relative comparison can be made by re-running the fitter with different initialization values of the parameter set and comparing the relative log-likelihood values, taking the smallest value as the relatively best fit. Lastly, a fairly recent paper, however, may warrant future attention and consideration, as it suggests and demonstrates some possibly robust methods which various disciplines have picked up and used for their goodness-of-fit definition for the log-likelihood method [66]. In my analysis for each fit, I use the former method and take the “best” relative fit results out of 10 pseudo-randomly initialized parameter fits. The chosen bounds for which the randomly initialized parameter values span are either already mathematically bounded, for example a SDME may range between  $[-1, 1]$  or based on theoretical guidance.

### 6.2.1 Fit Quality and Fitter Consistency Checks

The acceptance-rejection method (ARM) is a popular method used for generating random samples from single- as well as multi-variate distributions. This method is used to obtain “quality” checks on the event kinematic distributions. Additionally, this method may be used to obtain an essential and preliminary assessment check on the convergence consistency of the fitter. The two respective programs using this method are the plotResults program of AmpTools and a re-tailored version of the pseudoData generator program of AmpTools, see Fig. 6.1.

The idea behind the ARM stems from the desire to obtain a sample distribution of say a distribution of density  $f$  within a domain  $X \subset \mathbf{R}^d$ . If a sample from another distribution of density

$g(x)$  is generated such that,

$$f(x) \leq c g(x) \quad \text{for all } x \in X, \quad (6.5)$$

where constant  $c > 0$ , then a sample  $X$  may be obtained from  $g(x)$  with an acceptance of probability  $f(X)/[cg(X)]$  [67]. In practice, one simply compares a calculated weight,  $w_i$ , for each and every event of a sample distribution to that of a pseudo-randomly generated event,  $u_i$ , of a uniform distribution  $U(0,1)$  via the condition

$$u_i \leq w_i = \frac{I(x_i)}{I_{max}}, \quad (6.6)$$

where the constant  $c$  is equal or near to 1,  $I_i$  is the calculated event variable of interest,  $I_{max}$  is the variable maximum out of the event sample, and the events  $x_i$  are accepted (rejected) when the condition is upheld (not upheld).

Using this method, one can weight various kinematic distributions for the detector simulated MCs and compare these distributions to those of the input signal (q-weighted) data events. These comparisons are referred to as quality checks on the fits. Its a measure of how well the fit weighted kinematic MC distributions reproduce the event kinematics of the data. Furthermore, this method can be used to select out events from a MC distribution based on the fixed-parameter value selection used in obtaining the event intensity (fit-function) weights, e.g.  $I_i(x = 3, X_i)/I_{max}$  where  $x = 3$  is the selected fixed-parameter value and  $X_i$  represents the kinematic phase space for the  $i^{th}$  event. Subsequently, when the “selected” MC sample is fed back through the fitter (along with the two other accompanying data inputs), the freely varying fit parameter ought to converge towards the same value previously selected. This is referred to as a consistency check on the fitter for a given fit function and phase space. I modified the pseudo-data generator in my PWA framework to directly accept the ROOT format MC files which are also used as inputs to the fitter.

### 6.3 Fit Functions

The overall fit function or rather the intensity for a PWA takes the general form as that found in Eqn. 6.4, namely  $\mathcal{I}(\vec{x}, X) = \sum_{j,j'} \mathcal{T}_j \mathcal{T}_{j'}^* \mathcal{M}_j(\vec{x}, X) \mathcal{M}_{j'}^*(\vec{x}, X)$ . In the case of the  $\omega \rightarrow 3\pi$  decay, the Bose-statistics of the final-state particles require the sum over total angular momentum in the partial-wave expansion to only be of integer values, i.e.  $J = l = 1, 2, 3, \dots$ . Conservation of

parity adds the additional restriction that these be odd integers, i.e.  $J = 1, 3, 5, \dots$ . For Dalitz plot analyses of strong decays, different spin-parity states don't interfere. This was demonstrated from the orthonormality condition of Wigner D-functions and parity conservation. Lastly, for low energies, the first terms of a partial-wave expansion are expected to dominate. Lastly, with the lowest lying states of a partial-wave expansion expected to dominate, only the P-wave ( $J = L = 1$ ) was considered in my analysis. The intensity function in my PWA takes the factorized form,

$$\mathcal{I}_{full} = |\mathcal{T}|^2 |\mathcal{M}|^2, \quad (6.7)$$

where  $\mathcal{T}$  and  $\mathcal{M}$  are the production and decay amplitudes, respectively. The squared decay amplitude,  $|\mathcal{M}|^2$ , is comprised of three factors,

$$|\mathcal{M}|^2 = |\vec{p}_{\pi^+} \times \vec{p}_{\pi^-}|^2 \mathcal{W} |\mathcal{F}|^2, \quad (6.8)$$

where  $|\vec{p}_{\pi^+} \times \vec{p}_{\pi^-}|^2$  is a kinematic boundary factor,  $\mathcal{W}$  is the angular decay distribution, and  $|\mathcal{F}|^2$  is the reduced decay distribution. The latter two distributions factorized from one another in part due to their respective helicity dependent and independence, see Eqns. 5.39 and 5.40.

Thus, the fit function for my analysis takes the factorized form

$$\mathcal{I}_{full} = |\mathcal{T}|^2 |\vec{p}_{\pi^+} \times \vec{p}_{\pi^-}|^2 \mathcal{W}^0(\cos \theta, \phi, \rho_{10}^0, \rho_{00}^0, \rho_{1,-1}^0) |\mathcal{F}(s, t, u, a_{JPAC}^{\omega \rightarrow 3\pi})|^2, \quad (6.9)$$

where  $\mathcal{W}^0(\cos \theta, \phi, \rho_{10}^0, \rho_{00}^0, \rho_{1,-1}^0)$  is the Schilling equation (Eqn. 5.60) for an unpolarized beam and target and unobserved recoil proton spin,  $\theta$  and  $\phi$  are the decay angles (chosen in the Adair frame, see Fig. 4.1) with respect to the decay plane normal, the  $\rho^0$ 's are the  $\omega$  meson SDMEs for the respective Schilling equation,  $\mathcal{F}(s, t, u, a_{JPAC}^{\omega \rightarrow 3\pi})$  is the JPAC decay amplitude (Eqn. 5.82), and  $a_{JPAC}^{\omega \rightarrow 3\pi}$  is the JPAC  $\omega \rightarrow 3\pi$  decay parameter. The squared production amplitude,  $|\mathcal{T}|^2$ , was supplemented with the differential cross section measurements from the CLAS-g11a group [7] for all of my fits. In practice, I did this by weighting my detector accepted MC events with the differential cross section measurements for all of my fits.

Note, with the Log Likelihood function, there are two sums, the data log sum and the MC integral sum (see Eqn. 6.2). The intensity distribution in the former (latter) term is calculated using data (detector simulated MC) events. The goal of the Log Likelihood method is to minimize the difference between these two terms. The major differences between the data and detector

simulated MC (accMC) distributions can be attributed to the lack of real physics modelled in the latter. By extracting physics weights from the data, one can enhance the physics modelled in the MC as well as improve the minimization or convergence of the Log Likelihood function. For example, quite often with partial-wave analyses, in the absence of differential cross section measurements, the exponential t-slope dependence of the data is extracted and the MC events are generated with this dependence. This is further improved when performed per energy bin.

When extracting the three SDMEs,  $\rho_{10}^0, \rho_{00}^0, \rho_{1,-1}^0$ , the fit function I used in my fits was given by

$$\mathcal{I}_{full} = |\vec{p}_{\pi^+} \times \vec{p}_{\pi^-}|^2 \mathcal{W}^0(\cos \theta, \phi, \rho_{10}^0, \rho_{00}^0, \rho_{1,-1}^0), \quad (6.10)$$

where the differential cross section measurements were used to weight the accMC events, the  $\lambda$  of Eqn. 4.6 was used for  $|\vec{p}_{\pi^+} \times \vec{p}_{\pi^-}|^2$ , and  $\mathcal{F} = 1$ . When extracting the JPAC  $\omega \rightarrow 3\pi$  decay parameter,  $a_{JPAC}^{\omega \rightarrow 3\pi}$ , the fit function I used was given by

$$\mathcal{I}_{full} = |\vec{p}_{\pi^+} \times \vec{p}_{\pi^-}|^2 \mathcal{W}^0(\cos \theta, \phi, \rho_{10}^0, \rho_{00}^0, \rho_{1,-1}^0) |\mathcal{F}(s, t, u, a_{JPAC}^{\omega \rightarrow 3\pi})|^2, \quad (6.11)$$

where the differential cross section measurements along with the Schilling equation were used to weight the accMC events, and the  $\lambda$  of Eqn. 4.6 was used for  $|\vec{p}_{\pi^+} \times \vec{p}_{\pi^-}|^2$ . Also, the  $\phi$  in terms of the physical (non-averaged) pion masses was also used. This differs from the  $\phi$  given in Eqn. 5.71. For comparison, the two versions are given by

$$\phi_{ave} = stu - m_{\pi_{ave}}^2 (M_\omega^2 - m_{\pi_{ave}}^2)^2 \quad (6.12)$$

$$\begin{aligned} \phi_{physical} = & stu + 2m_{\pi^+}^2 m_{\pi^-}^2 m_{\pi_0}^2 + 2(M_\omega^2 - s)m_{\pi^+}^2 m_{\pi^-}^2 - M_\omega^2 m_{\pi_0}^2 \\ & + 2(M_\omega^2 - t)m_{\pi^-}^2 m_{\pi_0}^2 - M_\omega^2 m_{\pi^+}^2 + 2(M_\omega^2 - u)m_{\pi^+}^2 m_{\pi_0}^2 - M_\omega^2 m_{\pi^-}^2, \end{aligned} \quad (6.13)$$

where they have been labelled in order to distinguish their use in the figures and discussion of the results. For the Schilling equation weights, I used the SDME values from the CLAS-g11a experiment.

## 6.4 Results

The results presented in this section for the  $\omega \rightarrow 3\pi$  decay distribution are two-fold. The distribution factorizes into two contributions, namely a helicity independent part and a helicity

dependent part, each of which contain parameters to be fitted to data. In order to investigate the JPAC decay amplitude model [3] (see Eqn. 5.82) which is the dynamic (helicity independent) contribution of the decay amplitude, I also needed to account for the Schilling equation [2] (see Eqn. 5.60) which is the angular (helicity dependent) contribution of the decay. Hence, parameter results are presented for both contributions. A brief recap of the two contributions and their respective parameterizations is provided below.

The normalized angular decay distribution for a vector meson decaying to three pseudoscalar particles under the experimental conditions of an unpolarized beam, unpolarized target, and unobserved spins for the recoil particles, is described by the Schilling equation. This equation describes the distribution of the decay with respect to the decay angles as well as Spin Density Matrix Elements (SDMEs) of the decaying resonance. The decay angles are taken with respect to the decay plane normal, and the SDMEs are spin density states (in the helicity basis) of the decay resonances. Under the conditions mentioned above and due to hermiticity and parity conservation, the distribution contains three contributing SDMEs. For the  $\omega \rightarrow 3\pi$  decay, these SDMEs are  $\rho_{10}^\omega$ ,  $\rho_{00}^\omega$ , and  $\rho_{1,-1}^\omega$  where the subscripts define the helicity transition states of the respective matrix elements.

The dynamic contribution of the decay is modelled by the JPAC decay amplitude. The isobar based, covariant helicity amplitude was constructed in the dispersive framework making use of analyticity and sub-energy unitarity. It accounts for both elastic and inelastic rescattering effects. Per isobar channel, the largely unknown inelastic contributions were novelly separated from the elastic contributions and parameterized by a power series expansion about a conformally mapped Mandalstam variable of the respective isobar state. Due to the symmetry of each channel and with the leading contribution of each expansion expected to suffice, only one parameter contributed to the overall parameterization of all inelastic contributions (see Eqn. 5.83). This parameter is referred to as the JPAC  $\omega \rightarrow 3\pi$  decay parameter,  $a_{JPAC}^{\omega \rightarrow 3\pi}$ .

In this section, I present both SDME and JPAC decay parameter results for the  $\omega \rightarrow 3\pi$  decay which were each extracted from both CLAS-g12 and CLAS-g8b data. The extracted CLAS-g12 and CLAS-g8b  $\omega$  meson SDMEs are each independently compared with the results published by the CLAS-g11a group [7]. The investigatory results for the JPAC  $\omega \rightarrow 3\pi$  decay parameter,  $a_{JPAC}^{\omega \rightarrow 3\pi}$ , are first time fits to real data. The expected results for this parameter are +8, see Fig.5.5. Each fitted parameter result presented is the best (lowest likelihood value) out of 10 results wherein the

parameters for each fit were randomly initialized. For all results, the systematic errors remain to be studied and taken into account.

Considering the differences in target position for the three data sets, my results for the CLAS-g12 and CLAS-g8b SDMEs are each in fairly good agreement with those extracted from the g11a data. The preliminary fits for the JPAC  $\omega \rightarrow 3\pi$  decay parameter show a strong dependence on the production variables, e.g. center-of-mass energy and momentum transfer, as well as the resonance mass (i.e.  $W = E_{c.m.}$ ,  $t$ , and  $M_\omega$ , respectively).

#### 6.4.1 CLAS-g12 SDMEs

SDMEs were extracted for the center-of-mass (c.m.) production energy for  $W : [1770 - 2840]$  MeV at widths of 10 MeV and the c.m.  $\omega$  cosine of the production angle for  $\cos(\theta_{c.m.}^\omega) : [-1.0 - 1.0]$  at widths of 0.1. My results across  $W : [1900 - 2840]$  MeV were in fairly good agreement with those extracted from the CLAS-g11a data, see sample Figs. 6.2 through 6.11. The difference in target position between the two experiments (90 cm upstream and the CLAS center, respectively) may contribute to the observed differences in both the SDMEs and differential cross section measurements. The differential cross section measurements obtained from the two experiments differ by roughly 5% [1]. The systematic errors for these CLAS-g12 SDME results remain to be studied and taken into account.

Scanning across the c.m. production energies, one see that the strongest differences between the SDMEs of the CLAS-g12 and CLAS-g11a results appear in the forward c.m. production angle, roughly between  $\cos(\theta_{c.m.}^\omega) : [0.5 - 1.0]$ . As well, differences between the  $\rho_{1,-1}$  SDMEs in the forward production angle region  $\cos(\theta_{c.m.}^\omega) : [0.2 - 1.0]$  on across the energies  $W : [1900 - 2410]$  MeV tend to be the strongest. These differences tended to be exacerbated for some of the fits across  $W : [1800 - 1900]$  (not present in the figures) and require further investigation. Yet there were no strong or obvious indications that these differences were correlated with any trends in the respective global bin acceptances or the more subtle quality check acceptances. The trends of the result values for each of the three SDMEs across the energy and cosine angle are in fairly good agreement between the two data sets.

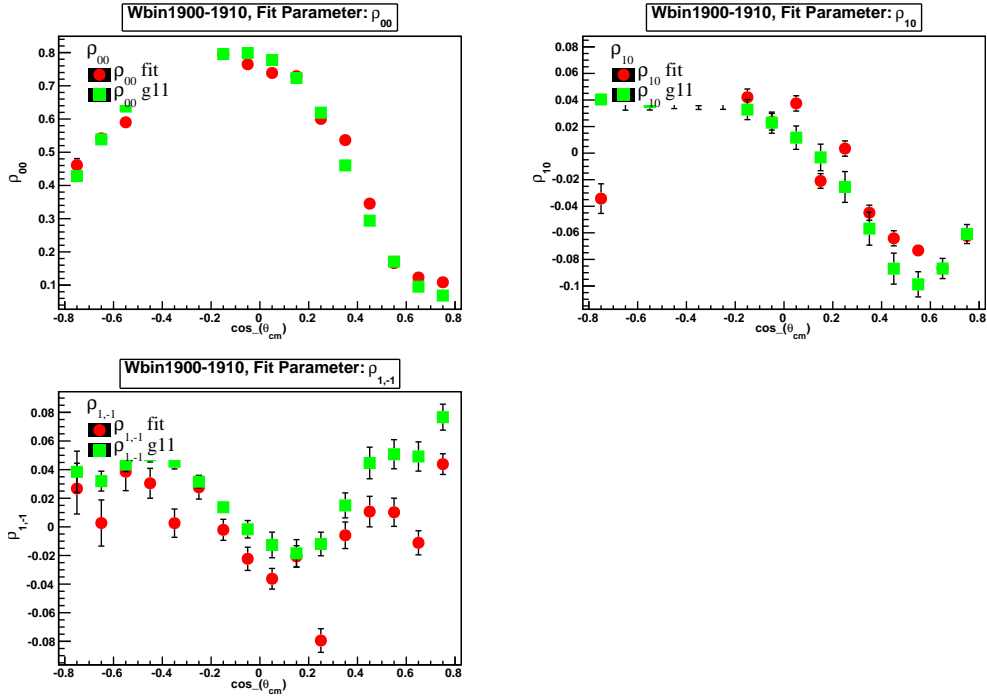


Figure 6.2: g12, g11a SDME comparison for  $W : [1900 - 1910]$  MeV and  $\cos(\theta_{cm}^\omega) : [-1.0 - 1.0]$  at widths of 0.1

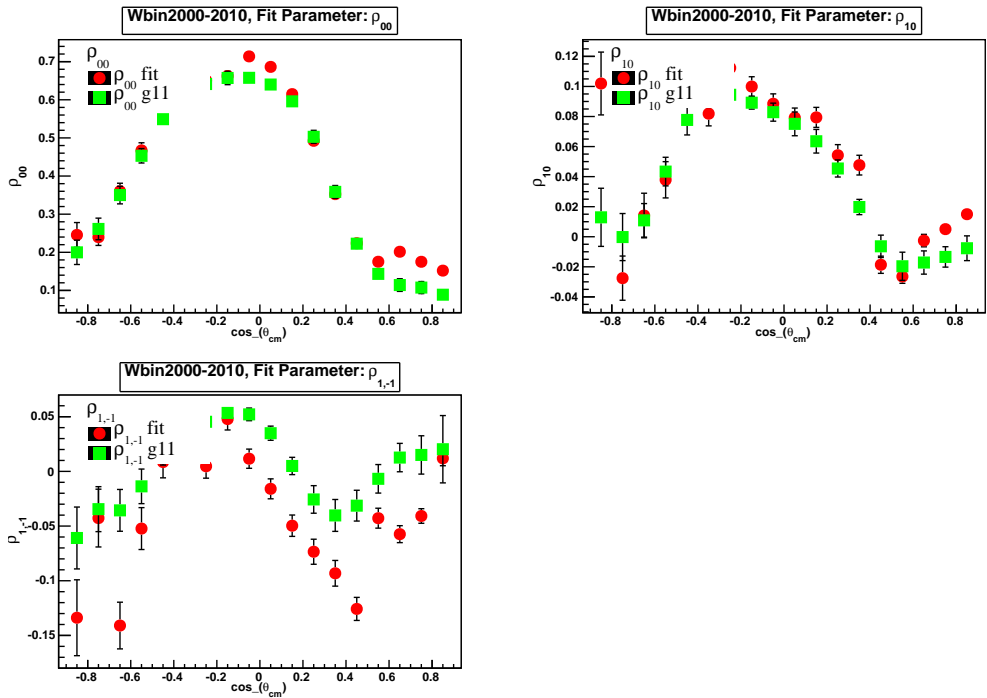


Figure 6.3: g12, g11a SDME comparison for  $W : [2000 - 2010]$  MeV and  $\cos(\theta_{cm}^\omega) : [-1.0 - 1.0]$  at widths of 0.1

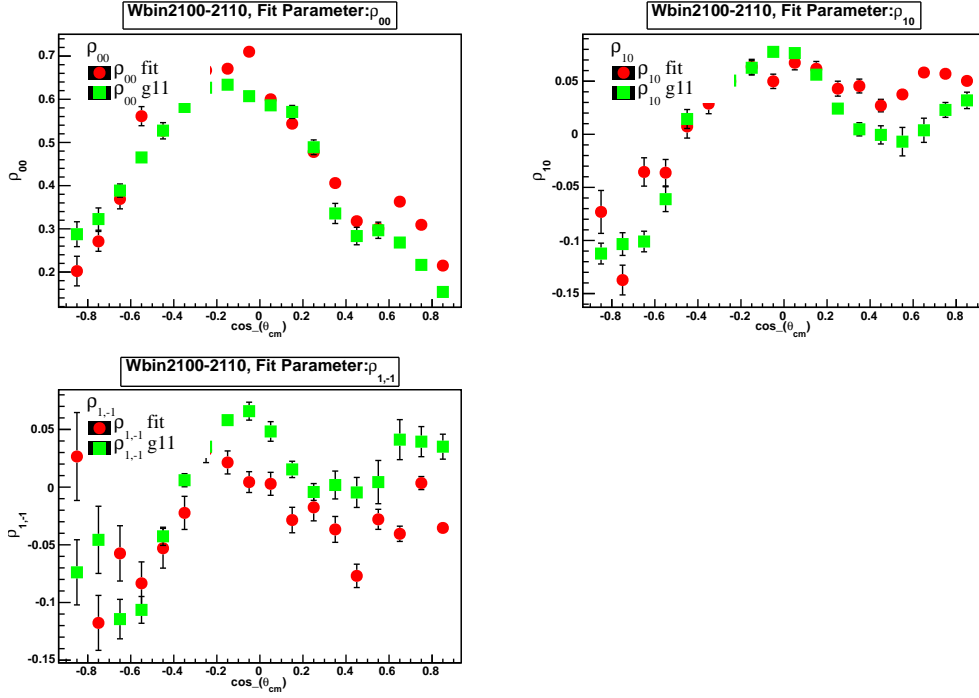


Figure 6.4: g12, g11a SDME comparison for  $W$  :  $[2100 - 2110]$  MeV and  $\cos(\theta_{cm}^\omega) : [-1.0 - 1.0]$  at widths of 0.1

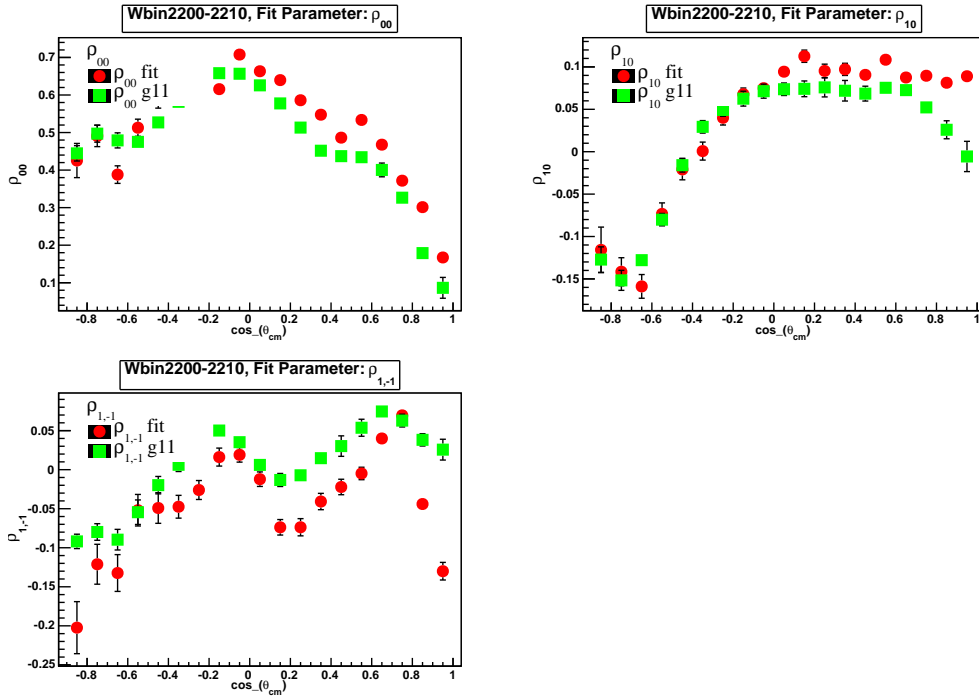


Figure 6.5: g12, g11a SDME comparison for  $W$  :  $[2200 - 2210]$  MeV and  $\cos(\theta_{cm}^\omega) : [-1.0 - 1.0]$  at widths of 0.1

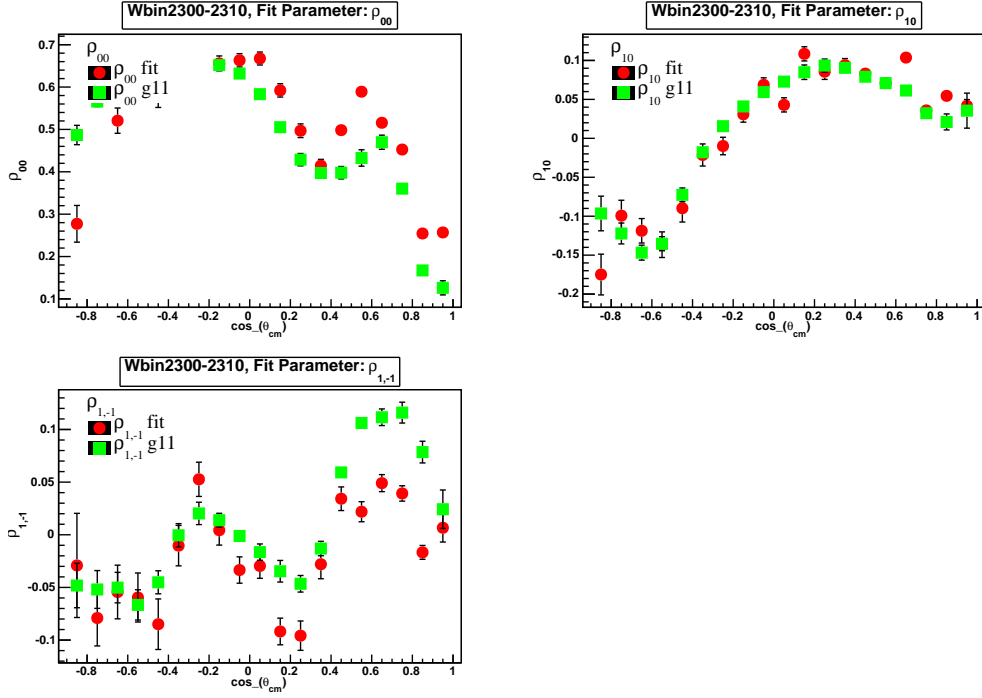


Figure 6.6: g12, g11a SDME comparison for  $W : [2300 - 2310]$  MeV and  $\cos(\theta_{cm}^\omega) : [-1.0 - 1.0]$  at widths of 0.1

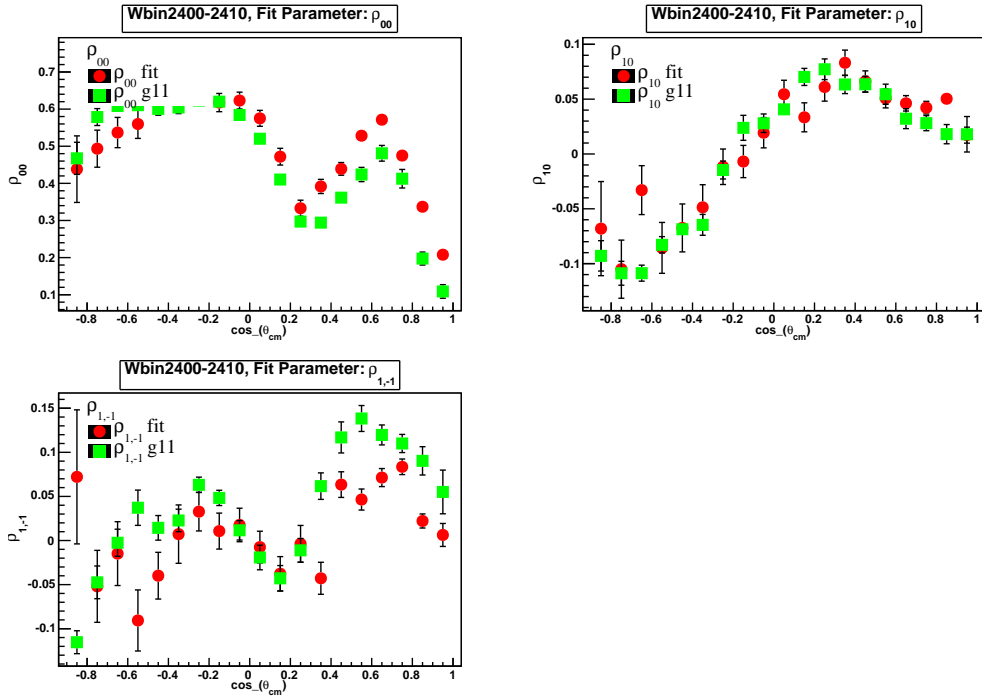


Figure 6.7: g12, g11a SDME comparison for  $W : [2400 - 2410]$  MeV and  $\cos(\theta_{cm}^\omega) : [-1.0 - 1.0]$  at widths of 0.1

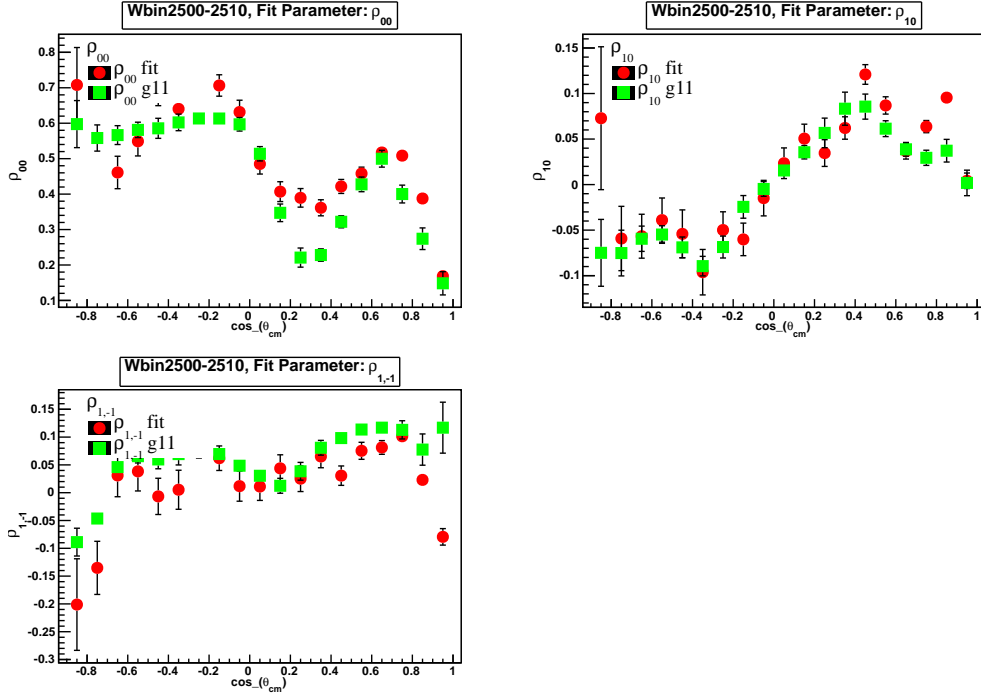


Figure 6.8: g12, g11a SDME comparison for  $W : [2500 - 2510]$  MeV and  $\cos(\theta_{cm}^\omega) : [-1.0 - 1.0]$  at widths of 0.1

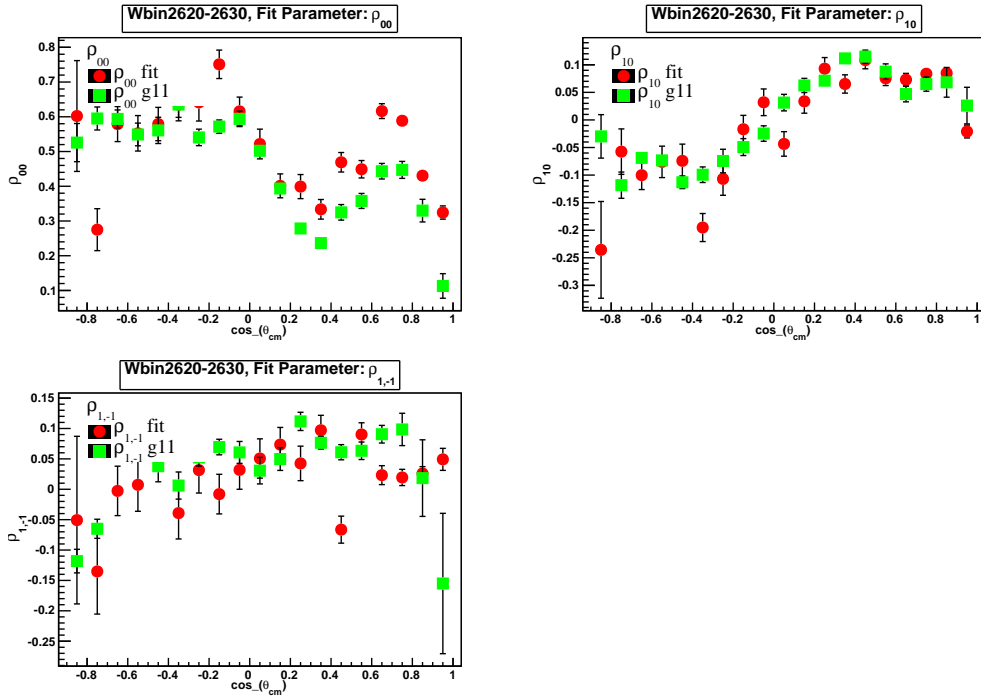


Figure 6.9: g12, g11a SDME comparison for  $W : [2620 - 2630]$  MeV and  $\cos(\theta_{cm}^\omega) : [-1.0 - 1.0]$  at widths of 0.1

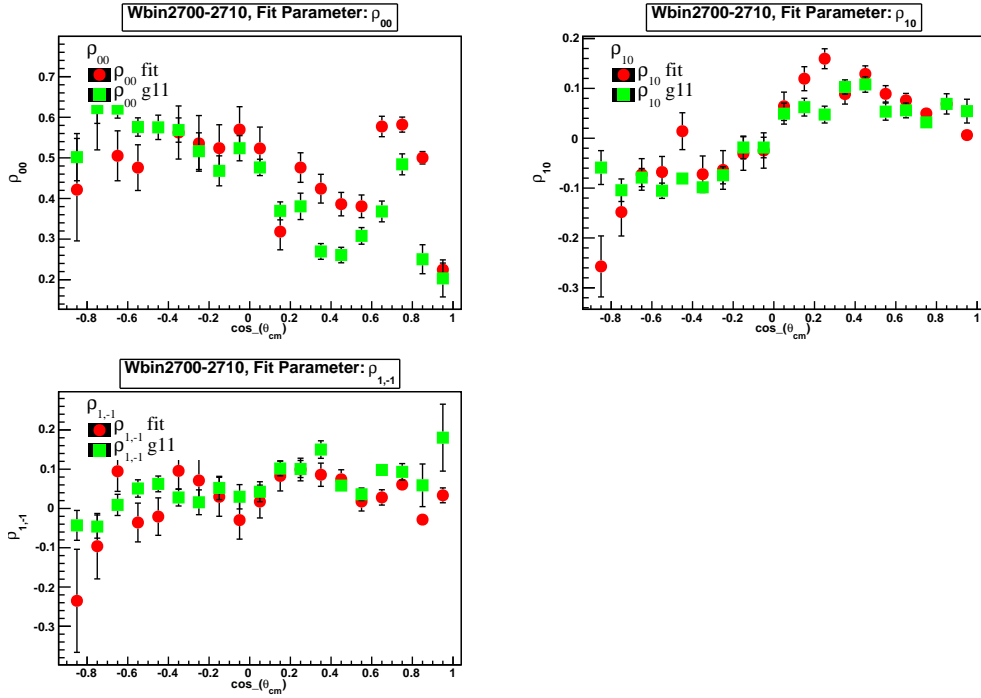


Figure 6.10: g12, g11a SDME comparison for  $W : [2700 - 2710]$  MeV and  $\cos(\theta_{cm}^\omega) : [-1.0 - 1.0]$  at widths of 0.1

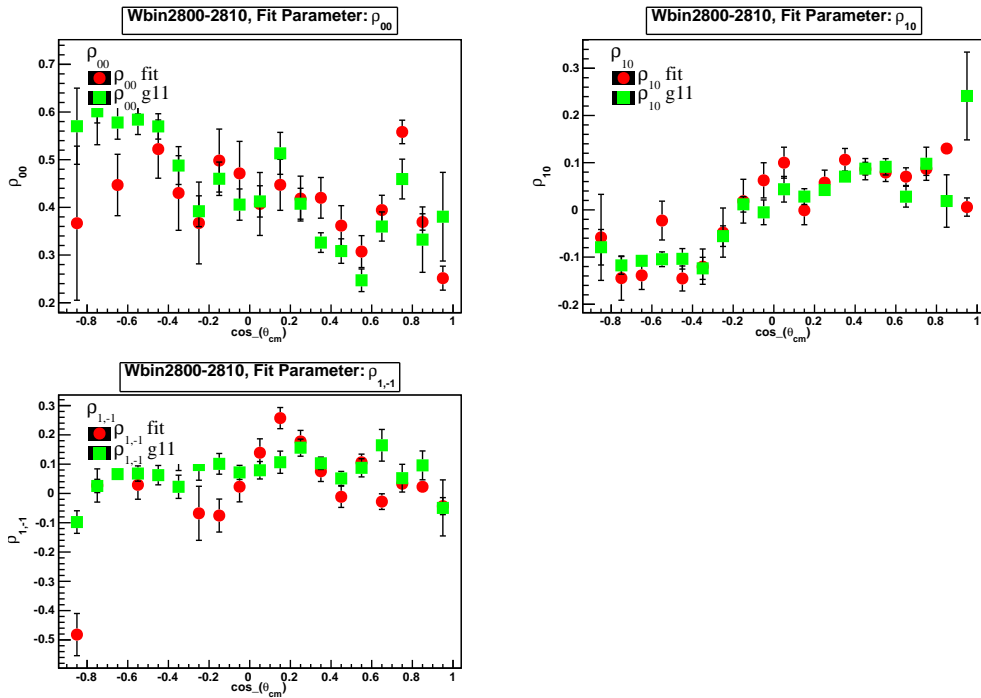


Figure 6.11: g12, g11a SDME comparison for  $W : [2800 - 2810]$  MeV and  $\cos(\theta_{cm}^\omega) : [-1.0 - 1.0]$  at widths of 0.1

### 6.4.2 CLAS-g8b SDMEs

SDMEs were extracted for the center-of-mass (c.m.) production energy for  $W : [1800 - 2300]$  MeV at widths of 50 MeV and the c.m.  $\omega$  cosine of the production angle for  $\cos(\theta_{c.m.}^\omega) : [-1.0 - 1.0]$  at widths of 0.1. My results across  $W : [1900 - 2300]$  MeV were in fairly good agreement with those extracted from the CLAS-g11a data, see sample Figs. 6.12 through 6.15. The difference in target position between the two experiments (20 cm upstream and the CLAS center, respectively) may contribute to the observed differences in both the SDMEs and differential cross section measurements. The differential cross section measurements obtained from the two experiments differ by roughly 5% [1]. The systematic errors for these CLAS-g8b SDME results remain to be studied and taken into account.

Scanning across the c.m. production energies, one see that the strongest differences between the SDMEs of the CLAS-g8b and CLAS-g11a results appear in the forward c.m. production angle, roughly between  $\cos(\theta_{c.m.}^\omega) : [0.2 - 1.0]$ . Across the entire c.m. cosine production angle,  $\cos(\theta_{c.m.}^\omega) : [-1.0 - 1.0]$ , for the energies  $W : [1900 - 2200]$  MeV, the trends between  $\rho_{0,0}$  SDME values for the two data set appear reasonably similar yet the g8b results were consistently shifted upwards from the corresponding g11a results. Correcting for systematic error might resolve this observed difference. These differences tended to be exacerbated for some of the fits across  $W : [1800 - 1900]$  (not present in the figures) and require further investigation. Yet there were no strong or obvious indications that these differences were correlated with any trends in the respective global bin acceptances or the more subtle quality check acceptances. The trends of the result values for each of the three SDMEs across the energy and cosine angle are in fairly good agreement between the two data sets.

### 6.4.3 CLAS-g12 JPAC $\omega \rightarrow 3\pi$ Decay Parameter

The following JPAC  $\omega \rightarrow 3\pi$  decay parameter results were extracted from the JPAC decay amplitude,  $\mathcal{F}(s, t, u, a_{JPAC}^{\omega \rightarrow 3\pi})$ , using CLAS-g12 data. The squared production amplitude,  $|\mathcal{T}|^2$ , and angular decay distribution,  $\mathcal{W}$ , of the overall fit function,  $I_{full} \propto |\mathcal{T}|^2 \mathcal{W} |\mathcal{F}|^2$ , were taken into account by weighting the detector simulated MC events with the differential cross section measurements and Schilling equation. Thus, the fit function fitted to the CLAS-g12 data took the reduced form  $I_{full} = |\vec{P}_{\pi^+} \times \vec{P}_{\pi^-}|^2 |\mathcal{F}|^2$  where the prefactor is the (squared decay plane normal)

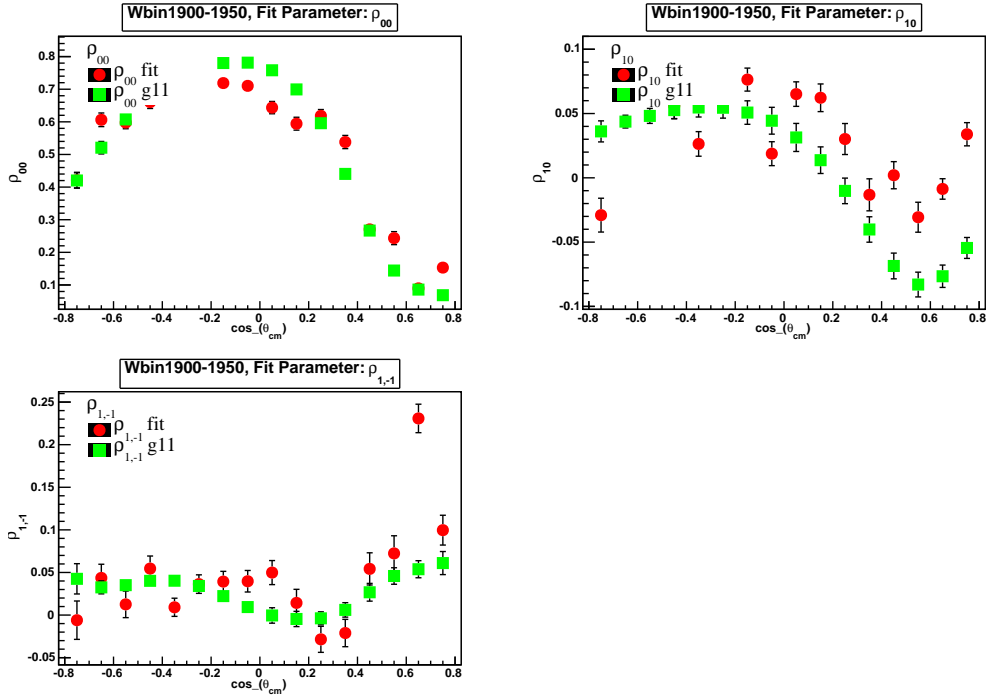


Figure 6.12: g8b, g11a SDME comparison for  $W : [1900 - 1950]$  MeV and  $\cos(\theta_{cm}^\omega) : [-1.0 - 1.0]$  at widths of 0.1

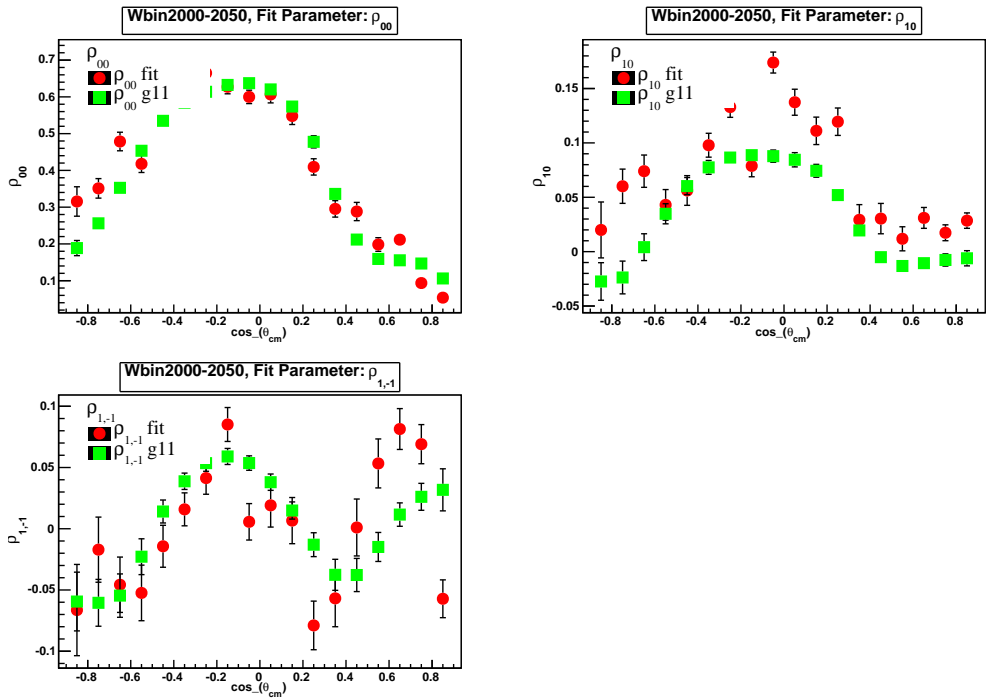


Figure 6.13: g8b, g11a SDME comparison for  $W : [2000 - 2050]$  MeV and  $\cos(\theta_{cm}^\omega) : [-1.0 - 1.0]$  at widths of 0.1

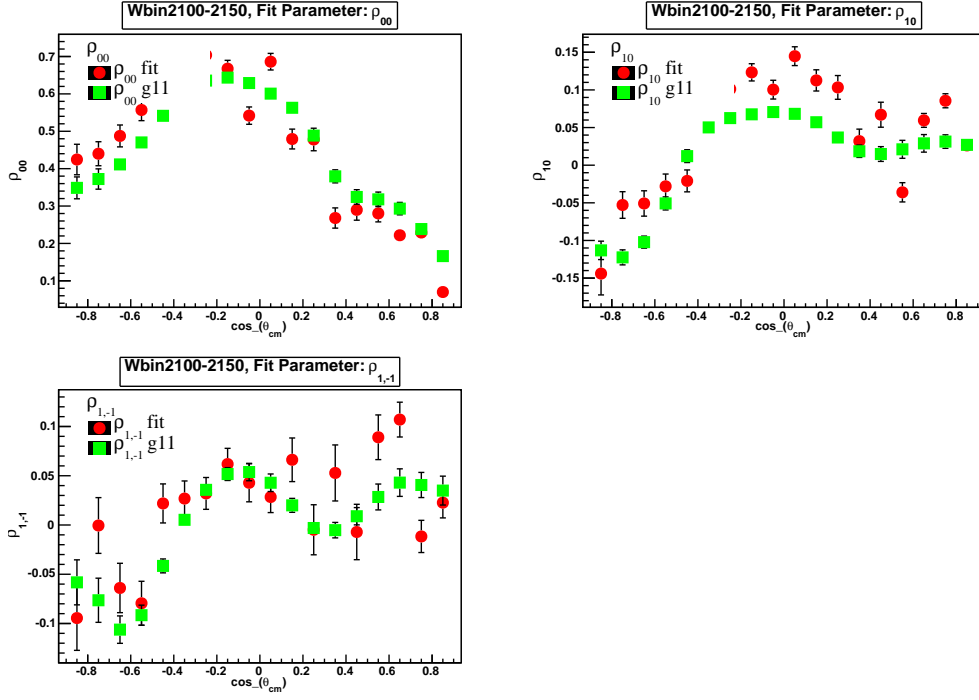


Figure 6.14: g8b, g11a SDME comparison for  $W : [2100 - 2150]$  MeV and  $\cos(\theta_{cm}^\omega) : [-1.0 - 1.0]$  at widths of 0.1

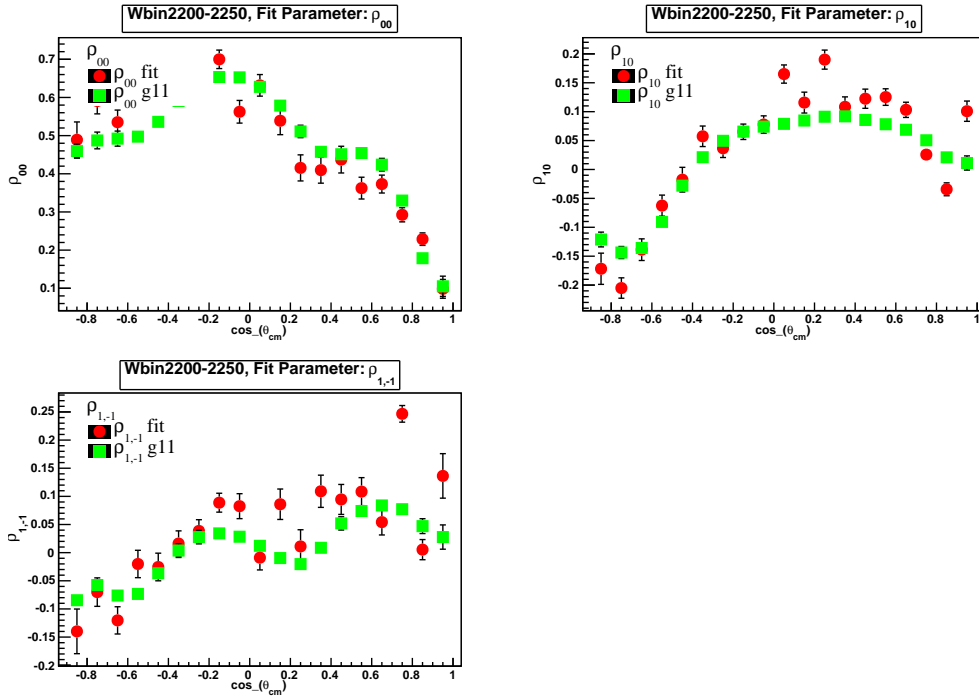


Figure 6.15: g8b, g11a SDME comparison for  $W : [2200 - 2250]$  MeV and  $\cos(\theta_{cm}^\omega) : [-1.0 - 1.0]$  at widths of 0.1

kinematic boundary factor. For these investigatory results of the JPAC decay parameter, it is important to note that the CLAS-g11a differential cross section measurements and SDMEs were used in lieu of those extracted from the CLAS-g12 data. The systematic errors for the CLAS-g12 SDMEs and JPAC decay parameter results remain to be studied and taken into account.

The fit results for the JPAC decay parameter,  $a_{JPAC}^{\omega \rightarrow 3\pi}$ , to CLAS-g12 data are ordered with respect to single and double binned fits as follows: single bins of c.m. production energy,  $W$ ; primary bins of incoming photon energy,  $E_\gamma$  with secondary bins in momentum transfer,  $t$ -Mandelstam; single bins across the  $\omega$  resonance mass,  $M_\omega$ ; and primary bins of c.m. production energy,  $W$ , with secondary bins having symmetric cuts about the omega mass mean, e.g.  $M_\omega \pm 10$  MeV.

For  $W : [1770 - 2840]$  MeV at widths of 10 MeV, Fig. 6.16, the JPAC decay parameter using  $\lambda$  as the boundary factor had an visible c.m. production energy dependence for the parameter with a spread mostly between  $a_{JPAC}^{\omega \rightarrow 3\pi} : [-5 - 5]$ . The sources for the two peaks between  $W : [1770 - 2000]$  MeV and the rise in the higher energy region from  $W : [2500 - 2840]$  MeV are unknown at this time. Focusing on the more stable region  $W : [2000 - 2500]$  MeV, also Fig. 6.17, the parameter values have a spread mostly from  $a_{JPAC}^{\omega \rightarrow 3\pi} : [-3.5 - 1.0]$ . These values were all lower than the expected  $a_{JPAC}^{\omega \rightarrow 3\pi} = +8$ .

These fits were reproduced using  $\phi_{physical}$  for the boundary parameter, see Figs. 6.18 and 6.19. The peaks in the lower energy region and the lift in the higher energy region were visibly present as before. The bow across the energy might be due to experimental effects such as slight differences in the mean values of the  $\omega$  mass distribution across the c.m. production energy. This effect is under investigation. Focusing again on the more stable middle region,  $W : [2000 - 2500]$  MeV, the spread in parameter values appear to be slightly tighter aside from the issue of the obvious energy dependence. Most notable from the change in boundary factors is the overall decrease for the parameter values across the entire energy range. The spread across the more stable middle region has shifted downward from roughly  $a_{JPAC}^{\omega \rightarrow 3\pi} \approx -1.5$  to  $a_{JPAC}^{\omega \rightarrow 3\pi} \approx -4.5$  and  $a_{JPAC}^{\omega \rightarrow 3\pi} \approx -6.5$  in the low and high energy regions of  $W : [2000 - 2500]$  MeV, respectively.

For  $E_\gamma : [1200 - 3800]$  MeV at widths of 100 MeV and  $t : [0.100 - 3.100]$  GeV<sup>2</sup> at widths of 0.100 GeV<sup>2</sup>, the JPAC decay parameter using  $\lambda$  as the boundary factor had a visible momentum transfer dependence, see sample Figs. 6.20 through 6.23. The decay parameter values within  $E_\gamma : [1700 - 1800]$  and  $t : [0.400 - 1.300]$  GeV<sup>2</sup>,  $E_\gamma : [2100 - 2200]$  and  $t : [0.100 - 0.400]$  GeV<sup>2</sup>, and

$E_\gamma : [2300 - 2400]$  and  $t : [0.100 - 0.400]$  GeV<sup>2</sup> are notably positive,  $a_{JPAC}^{\omega \rightarrow 3\pi} \approx [1 - 3.8]$ ; however, the vast majority of decay parameter values are negative.

Coming back to the middle region of  $W : [2000 - 2500]$ , the JPAC decay parameter was extracted using  $\phi_{physical}$  for the boundary parameter for primary bins in  $W$  at widths of 100 MeV and secondary bins in the omega mass for  $M_\omega : [650 - 900]$  MeV at widths of 10 MeV and 5 MeV. The results for  $W : [2000 - 2100]$  and  $M_\omega : [650 - 900]$  MeV at widths of 10 MeV and 5 MeV are respectively given in Figs. 6.24 and 6.25. The remaining 4 pairs of results across  $W$  are given between Figs. 6.26 and 6.33. A clear dependence on both the energy and resonance mass were observed. The lower and higher mass regions tended to have larger positive decay parameter values than those extracted from the middle mass region of  $M_\omega : [775 - 795]$  MeV. The latter tend towards zero or just below zero. The fitted parameter values of the 10 MeV wide mass bins often tend to be larger than those of the 5 MeV wide bins. Parameter values for the mass ranges below and above  $M_\omega : [745 - 820]$  MeV are not present due to low statistics (predominantly low Monte Carlo statistics).

Perhaps most interesting are the next sets of fits for the decay parameter with respect to symmetric cuts about the  $\omega$  resonance mass. For  $W : [2000 - 2500]$  at width of 10 MeV and increasingly tighter symmetric cuts about the mean of the resonance mass, i.e.  $M_\omega \pm 40, 30, 20, 15, 10, 5, 2$  MeV, the JPAC decay parameter was extracted using  $\phi_{physical}$  for the boundary parameter, see Figs. 6.34 through ???. The decay parameter increases across the energy, most notably shifting from negative to positive values as the symmetric cuts approach the mean value of the  $\omega$  mass which roughly corresponds to the precision PDG value. Thus, as the width of the mass approaches zero and the mass itself approaches that of the PDG value, the JPAC decay parameter shifts from the negative values of Fig. 6.34 towards the expected positive value region, e.g. more closely aligned with the expected  $a_{JPAC}^{\omega \rightarrow 3\pi} = +8$ .

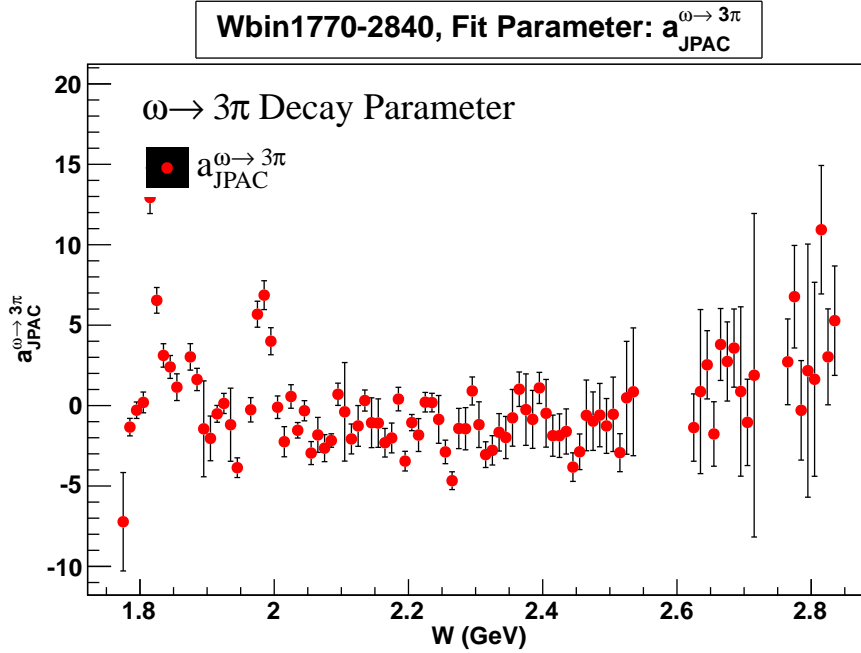


Figure 6.16: JPAC  $\omega \rightarrow 3\pi$  decay parameter,  $a_{JPAC}^{\omega \rightarrow 3\pi}$ , fitted to CLAS-g12 data for  $W : [1770-2840]$  MeV at widths of 10 MeV. The boundary factor used was  $\lambda$ , Eqn. 4.6

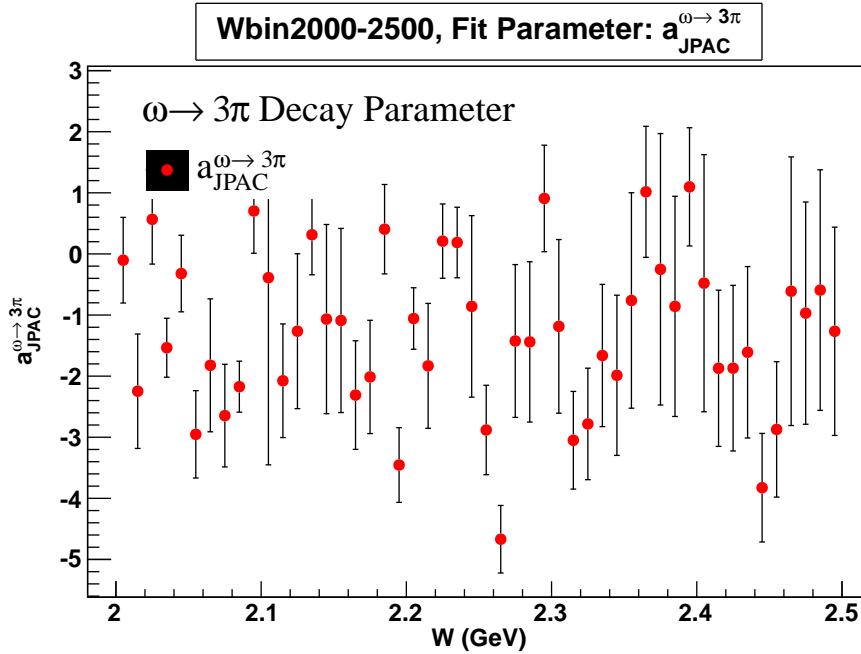


Figure 6.17: JPAC  $\omega \rightarrow 3\pi$  decay parameter,  $a_{JPAC}^{\omega \rightarrow 3\pi}$ , fitted to CLAS-g12 data for  $W : [2000-2500]$  MeV at widths of 10 MeV. The boundary factor used was  $\lambda$ , Eqn. 4.6

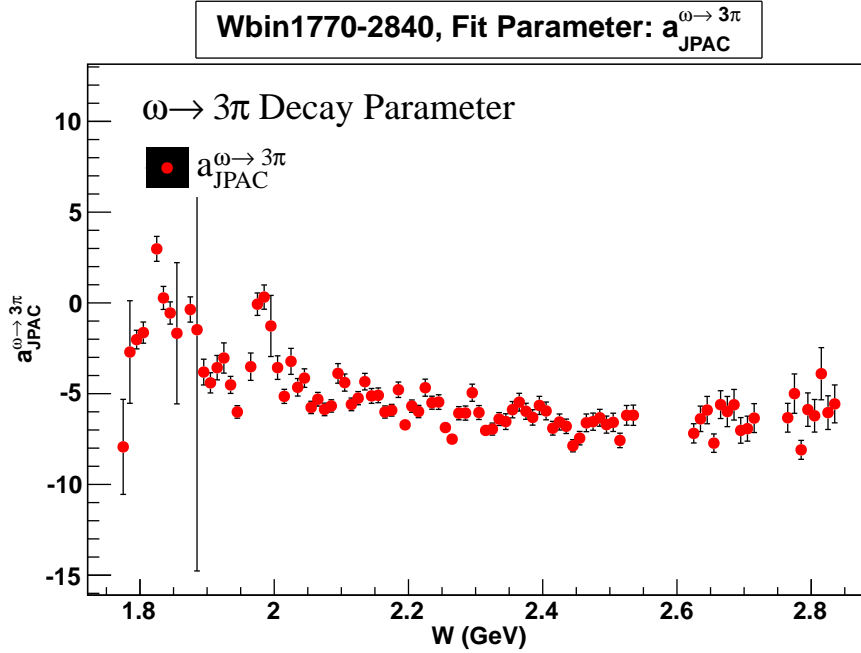


Figure 6.18: JPAC  $\omega \rightarrow 3\pi$  decay parameter,  $a_{JPAC}^{\omega \rightarrow 3\pi}$ , fitted to CLAS-g12 data for  $W : [1770-2840]$  MeV at widths of 10 MeV. The boundary factor used was  $\phi_{physical}$ , Eqn. 6.13

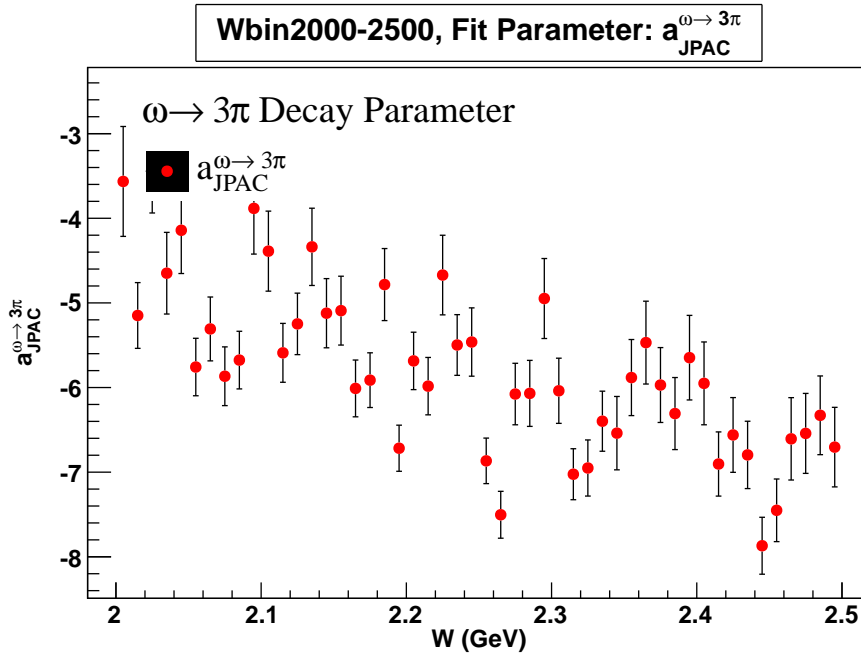


Figure 6.19: JPAC  $\omega \rightarrow 3\pi$  decay parameter,  $a_{JPAC}^{\omega \rightarrow 3\pi}$ , fitted to CLAS-g12 data for  $W : [2000-2500]$  MeV at widths of 10 MeV. The boundary factor used was  $\phi_{physical}$ , Eqn. 6.13

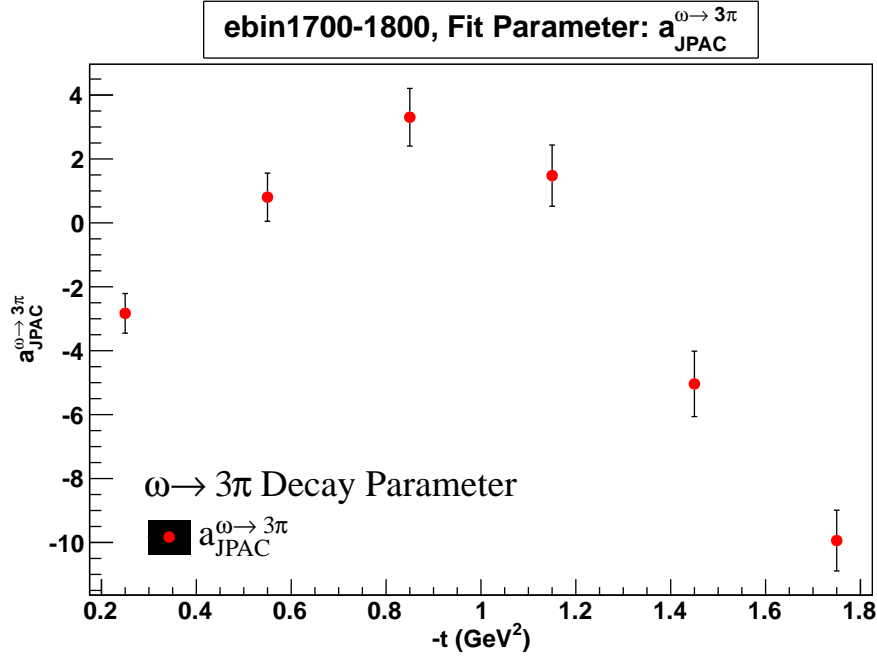


Figure 6.20: JPAC  $\omega \rightarrow 3\pi$  decay parameter,  $a_{JPAC}^{\omega \rightarrow 3\pi}$ , fitted to CLAS-g12 data for  $E_\gamma : [1700 - 1800]$  MeV and  $t : [0.100 - 3.100]$  GeV<sup>2</sup> at widths of 0.100 GeV<sup>2</sup>. The boundary factor used was  $\lambda$ , Eqn. 4.6

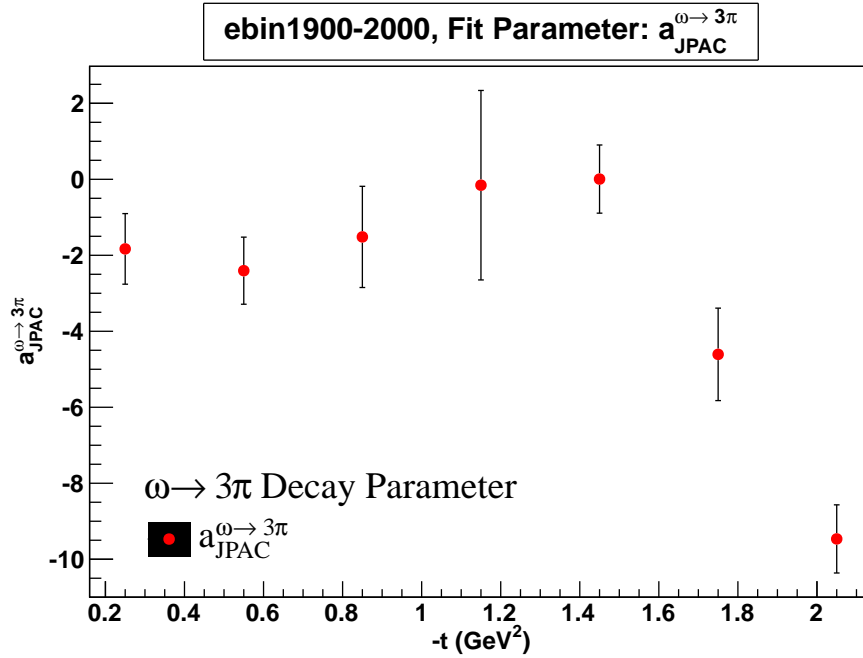


Figure 6.21: JPAC  $\omega \rightarrow 3\pi$  decay parameter,  $a_{JPAC}^{\omega \rightarrow 3\pi}$ , fitted to CLAS-g12 data for  $E_\gamma : [1900 - 2000]$  MeV and  $t : [0.100 - 3.100]$  GeV<sup>2</sup> at widths of 0.100 GeV<sup>2</sup>. The boundary factor used was  $\lambda$ , Eqn. 4.6

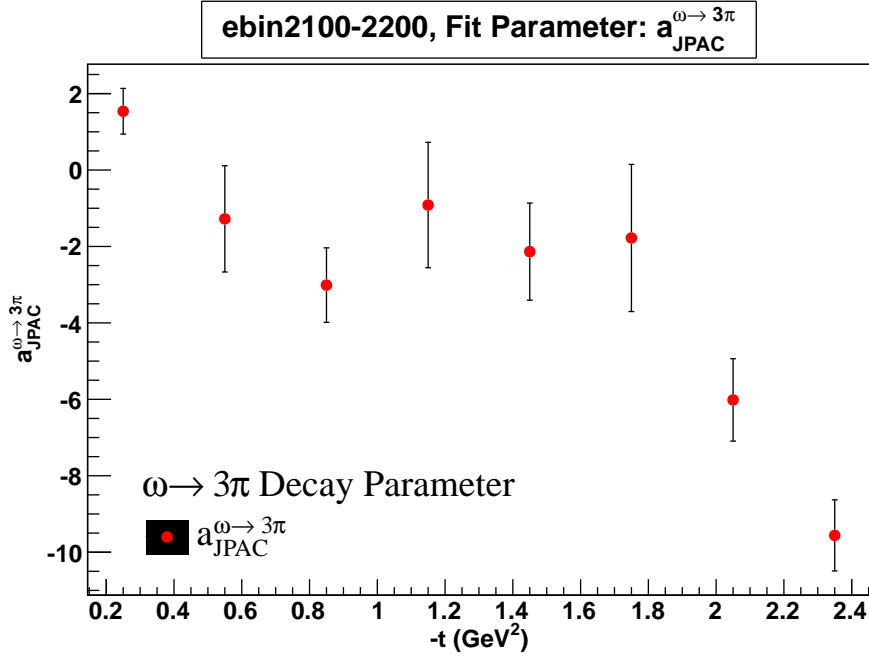


Figure 6.22: JPAC  $\omega \rightarrow 3\pi$  decay parameter,  $a_{JPAC}^{\omega \rightarrow 3\pi}$ , fitted to CLAS-g12 data for  $E_\gamma : [2100 - 2200]$  MeV and  $t : [0.100 - 3.100]$  GeV<sup>2</sup> at widths of 0.100 GeV<sup>2</sup>. The boundary factor used was  $\lambda$ , Eqn. 4.6

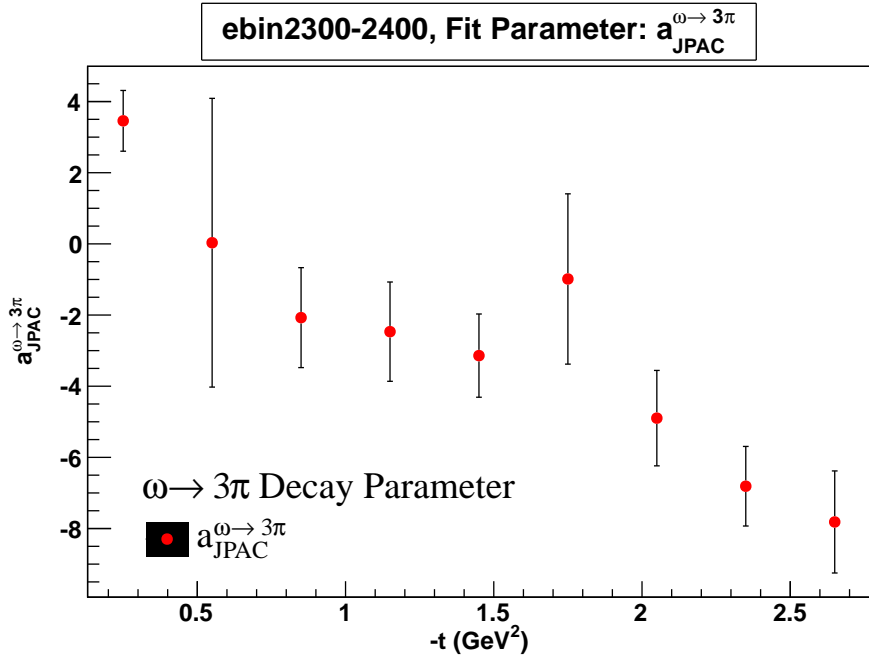


Figure 6.23: JPAC  $\omega \rightarrow 3\pi$  decay parameter,  $a_{JPAC}^{\omega \rightarrow 3\pi}$ , fitted to CLAS-g12 data for  $E_\gamma : [2300 - 2400]$  MeV and  $t : [0.100 - 3.100]$  GeV<sup>2</sup> at widths of 0.100 GeV<sup>2</sup>. The boundary factor used was  $\lambda$ , Eqn. 4.6

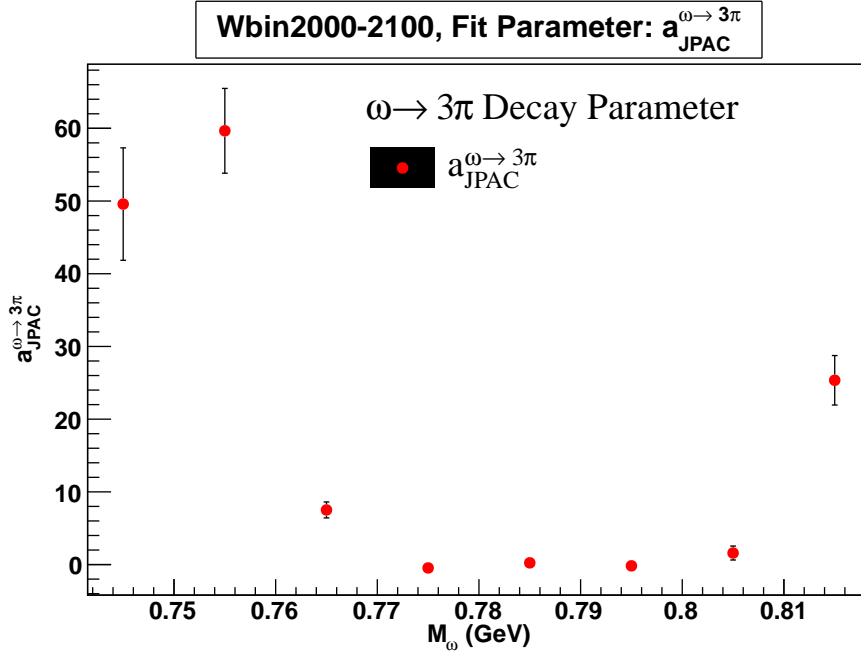


Figure 6.24: JPAC  $\omega \rightarrow 3\pi$  decay parameter,  $a_{JPAC}^{\omega \rightarrow 3\pi}$ , fitted to CLAS-g12 data for  $W : [2000 - 2100]$  MeV and  $M_\omega : [740 - 820]$  MeV at widths of 10 MeV. The boundary factor used was  $\phi_{physical}$ , Eqn. 6.13

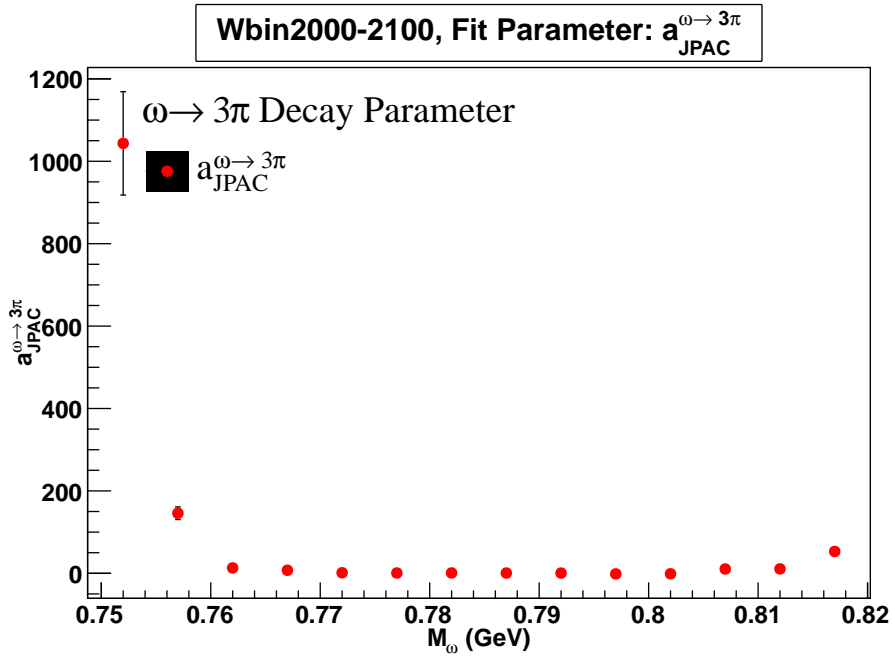


Figure 6.25: JPAC  $\omega \rightarrow 3\pi$  decay parameter,  $a_{JPAC}^{\omega \rightarrow 3\pi}$ , fitted to CLAS-g12 data for  $W : [2000 - 2100]$  MeV and  $M_\omega : [740 - 820]$  MeV at widths of 5 MeV. The boundary factor used was  $\phi_{physical}$ , Eqn. 6.13

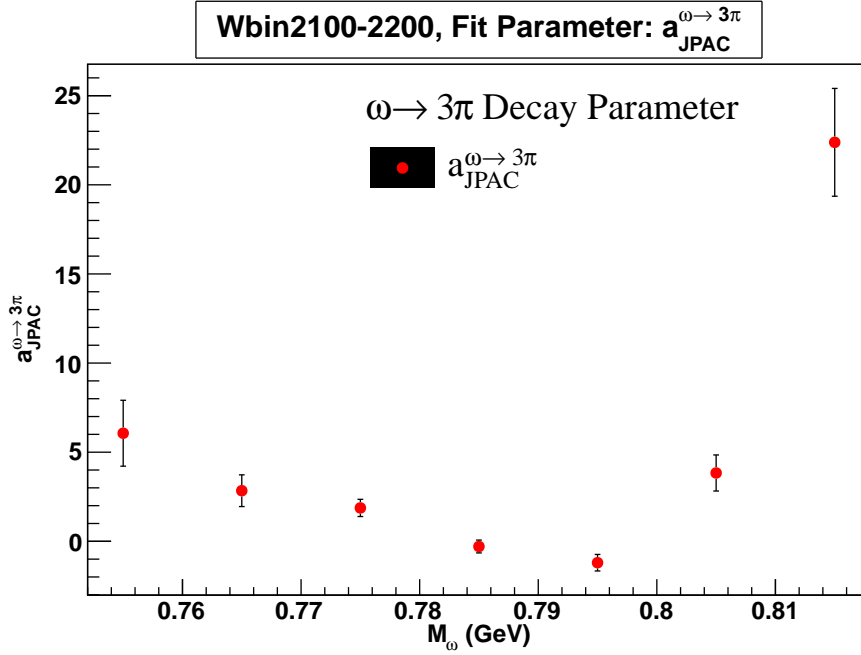


Figure 6.26: JPAC  $\omega \rightarrow 3\pi$  decay parameter,  $a_{JPAC}^{\omega \rightarrow 3\pi}$ , fitted to CLAS-g12 data for  $W : [2100 - 2200]$  MeV and  $M_\omega : [740 - 820]$  MeV at widths of 10 MeV. The boundary factor used was  $\phi_{physical}$ , Eqn. 6.13

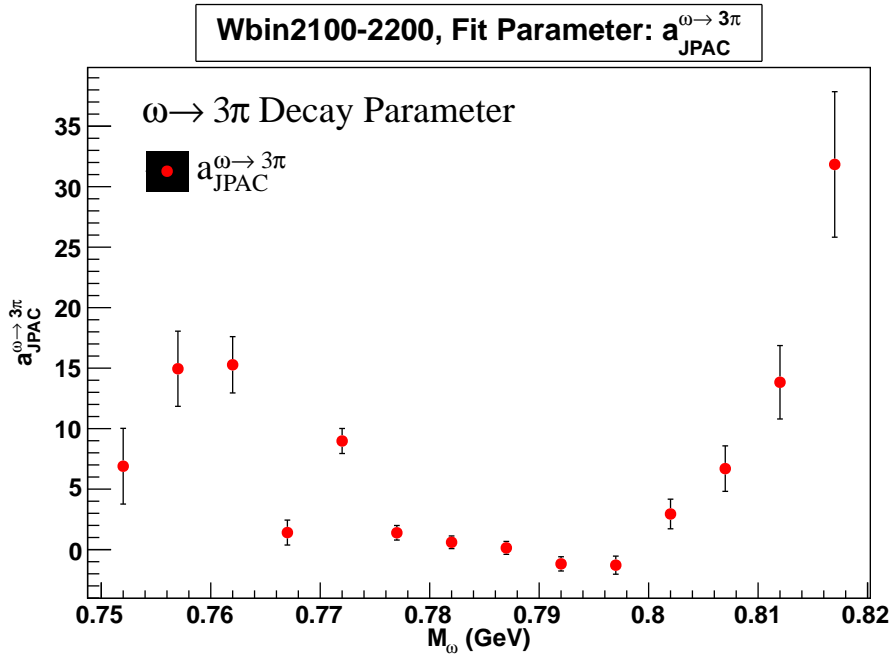


Figure 6.27: JPAC  $\omega \rightarrow 3\pi$  decay parameter,  $a_{JPAC}^{\omega \rightarrow 3\pi}$ , fitted to CLAS-g12 data for  $W : [2100 - 2200]$  MeV and  $M_\omega : [740 - 820]$  MeV at widths of 5 MeV. The boundary factor used was  $\phi_{physical}$ , Eqn. 6.13

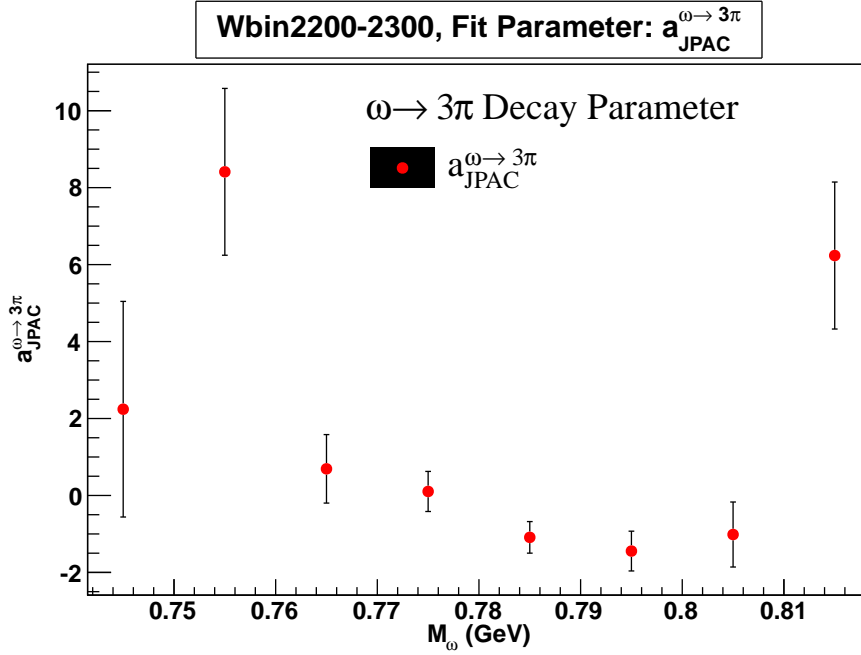


Figure 6.28: JPAC  $\omega \rightarrow 3\pi$  decay parameter,  $a_{JPAC}^{\omega \rightarrow 3\pi}$ , fitted to CLAS-g12 data for  $W : [2200 - 2300]$  MeV and  $M_\omega : [740 - 820]$  MeV at widths of 10 MeV. The boundary factor used was  $\phi_{physical}$ , Eqn. 6.13

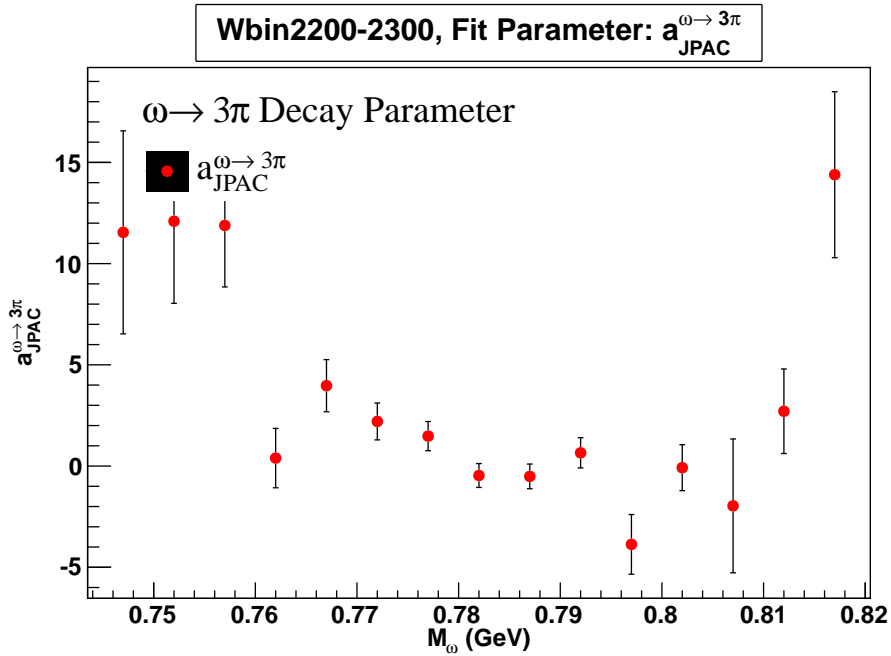


Figure 6.29: JPAC  $\omega \rightarrow 3\pi$  decay parameter,  $a_{JPAC}^{\omega \rightarrow 3\pi}$ , fitted to CLAS-g12 data for  $W : [2200 - 2300]$  MeV and  $M_\omega : [740 - 820]$  MeV at widths of 5 MeV. The boundary factor used was  $\phi_{physical}$ , Eqn. 6.13

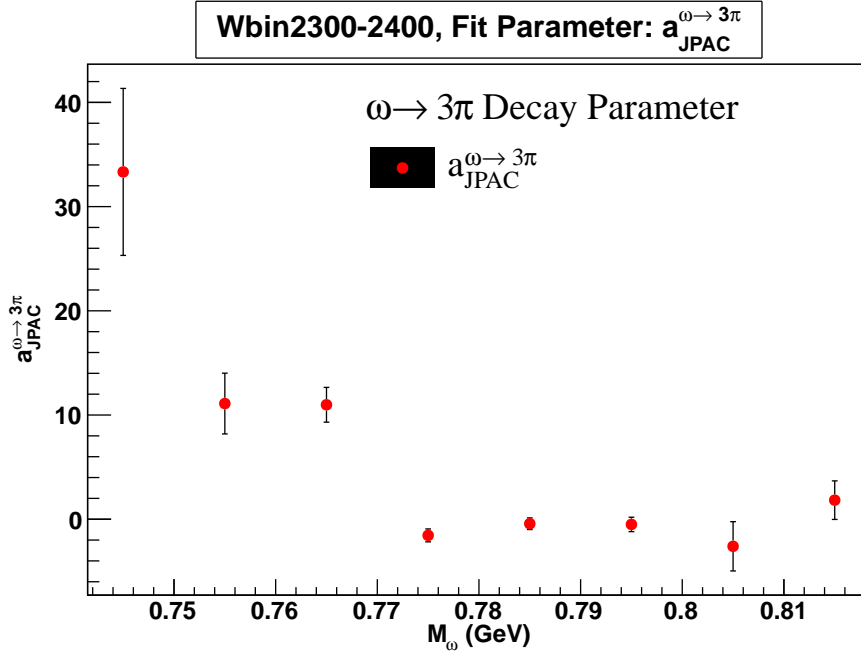


Figure 6.30: JPAC  $\omega \rightarrow 3\pi$  decay parameter,  $a_{JPAC}^{\omega \rightarrow 3\pi}$ , fitted to CLAS-g12 data for  $W : [2300 - 2400]$  MeV and  $M_\omega : [740 - 820]$  MeV at widths of 10 MeV. The boundary factor used was  $\phi_{physical}$ , Eqn. 6.13

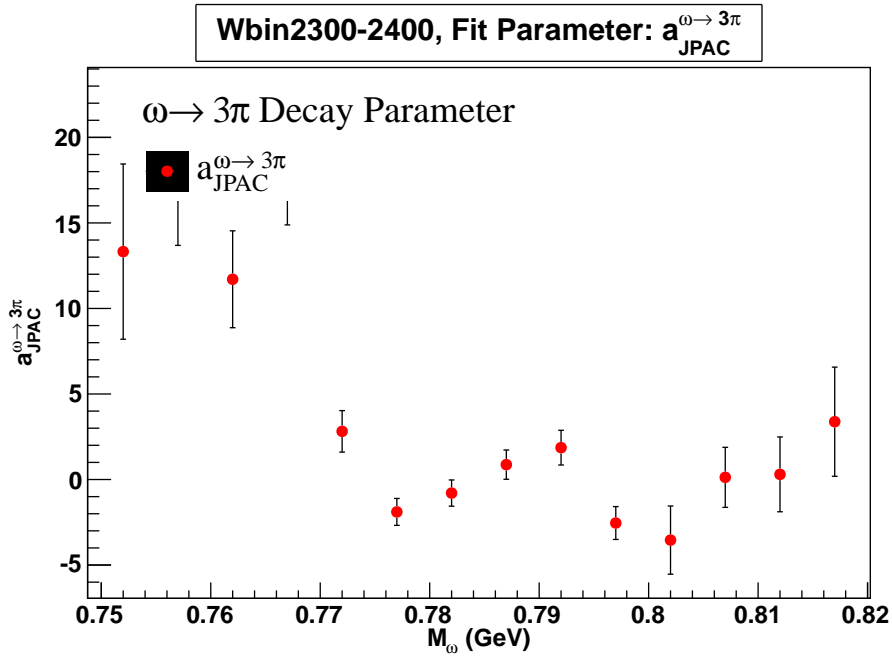


Figure 6.31: JPAC  $\omega \rightarrow 3\pi$  decay parameter,  $a_{JPAC}^{\omega \rightarrow 3\pi}$ , fitted to CLAS-g12 data for  $W : [2300 - 2400]$  MeV and  $M_\omega : [740 - 820]$  MeV at widths of 5 MeV. The boundary factor used was  $\phi_{physical}$ , Eqn. 6.13

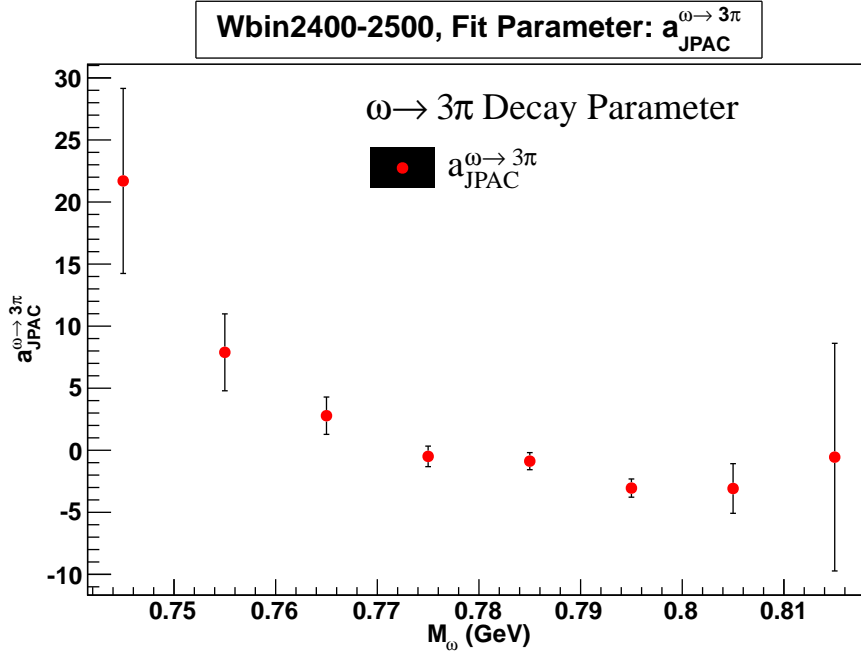


Figure 6.32: JPAC  $\omega \rightarrow 3\pi$  decay parameter,  $a_{JPAC}^{\omega \rightarrow 3\pi}$ , fitted to CLAS-g12 data for  $W : [2400 - 2500]$  MeV and  $M_\omega : [740 - 820]$  MeV at widths of 10 MeV. The boundary factor used was  $\phi_{physical}$ , Eqn. 6.13

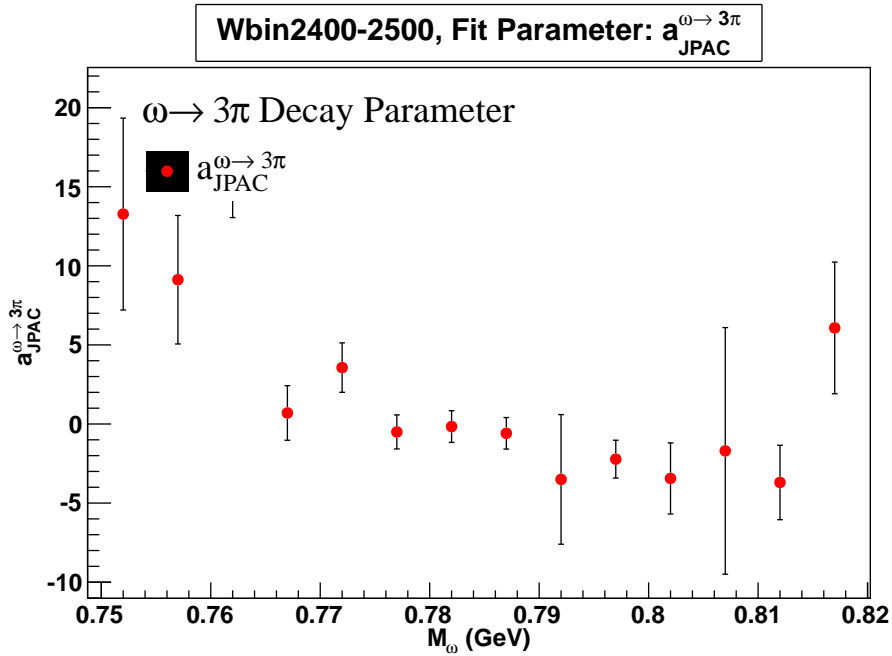


Figure 6.33: JPAC  $\omega \rightarrow 3\pi$  decay parameter,  $a_{JPAC}^{\omega \rightarrow 3\pi}$ , fitted to CLAS-g12 data for  $W : [2400 - 2500]$  MeV and  $M_\omega : [740 - 820]$  MeV at widths of 5 MeV. The boundary factor used was  $\phi_{physical}$ , Eqn. 6.13

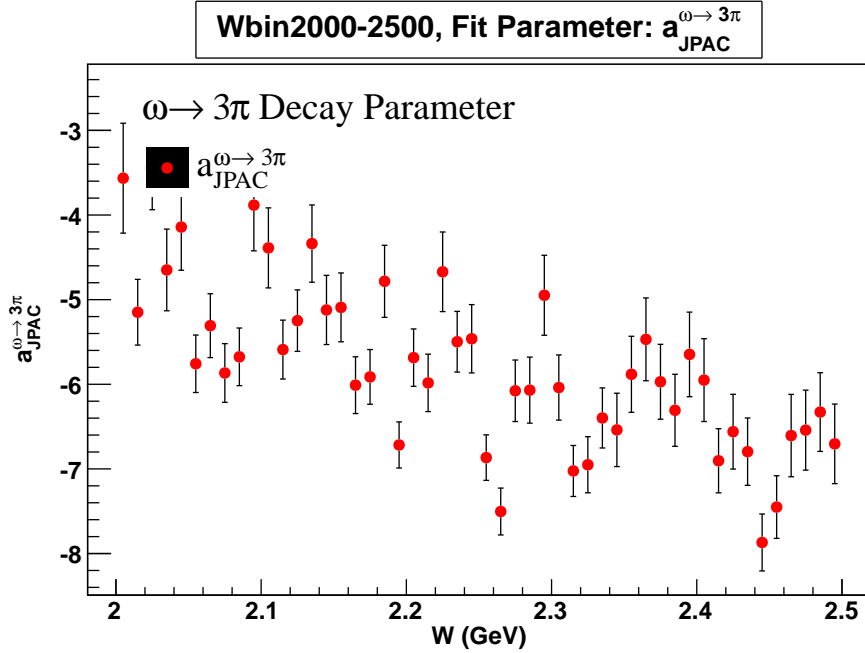


Figure 6.34: JPAC  $\omega \rightarrow 3\pi$  decay parameter,  $a_{JPAC}^{\omega \rightarrow 3\pi}$ , fitted to CLAS-g12 data for  $W : [2000 - 2500]$  MeV at widths of 10 MeV with no cuts about  $M_\omega$ . The boundary factor used was  $\phi_{physical}$ , Eqn. 6.13

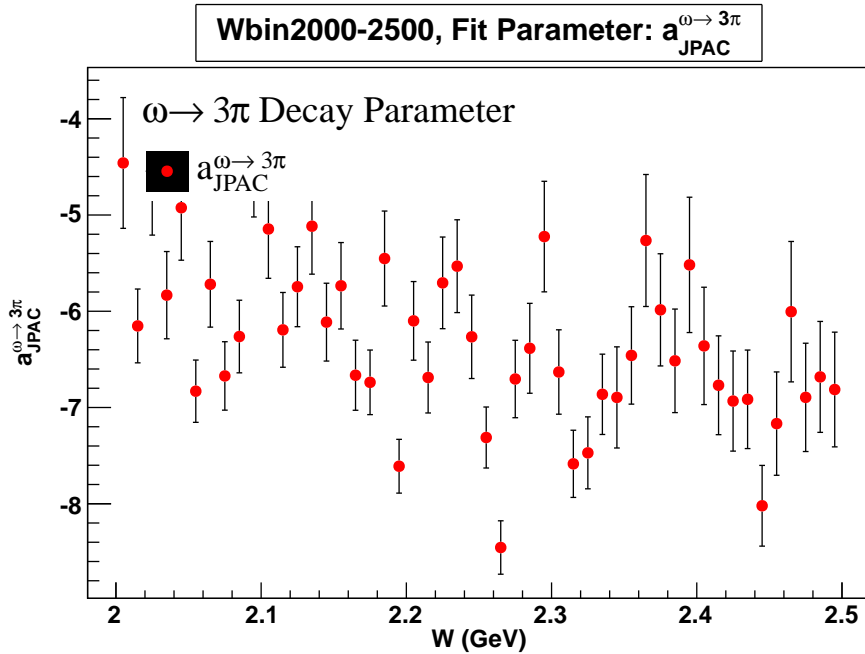


Figure 6.35: JPAC  $\omega \rightarrow 3\pi$  decay parameter,  $a_{JPAC}^{\omega \rightarrow 3\pi}$ , fitted to CLAS-g12 data for  $W : [2000 - 2500]$  MeV at widths of 10 MeV,  $M_\omega \pm 40$  MeV. The boundary factor used was  $\phi_{physical}$ , Eqn. 6.13

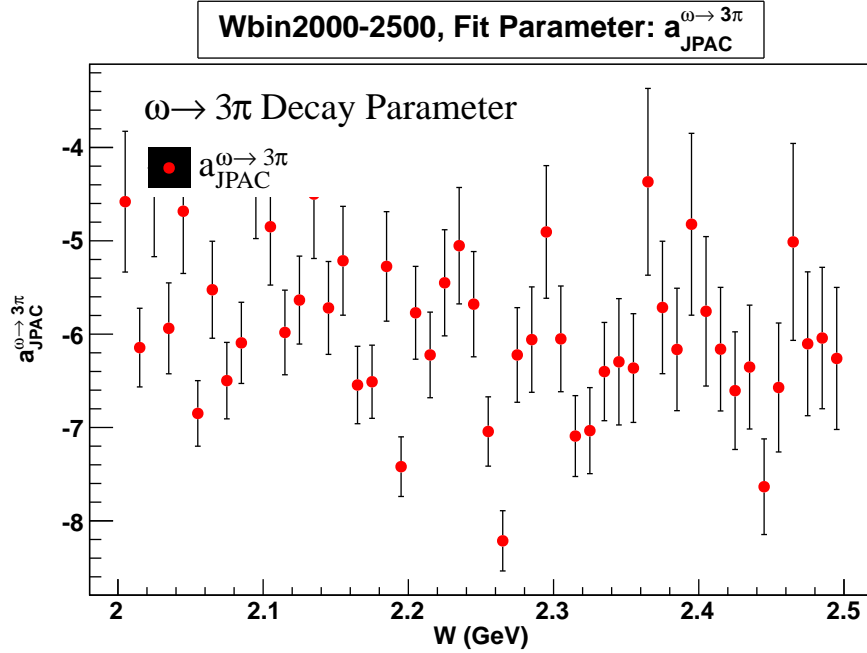


Figure 6.36: JPAc  $\omega \rightarrow 3\pi$  decay parameter,  $a_{JPAC}^{\omega \rightarrow 3\pi}$ , fitted to CLAS-g12 data for  $W : [2000-2500]$  MeV at widths of 10 MeV,  $M_\omega \pm 30$  MeV. The boundary factor used was  $\phi_{physical}$ , Eqn. 6.13

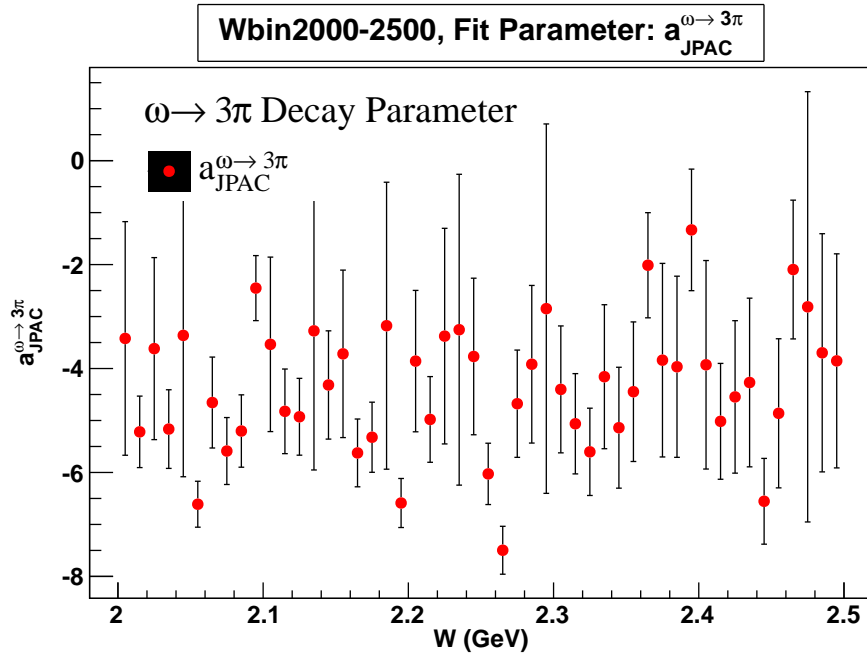


Figure 6.37: JPAc  $\omega \rightarrow 3\pi$  decay parameter,  $a_{JPAC}^{\omega \rightarrow 3\pi}$ , fitted to CLAS-g12 data for  $W : [2000-2500]$  MeV at widths of 10 MeV,  $M_\omega \pm 20$  MeV. The boundary factor used was  $\phi_{physical}$ , Eqn. 6.13

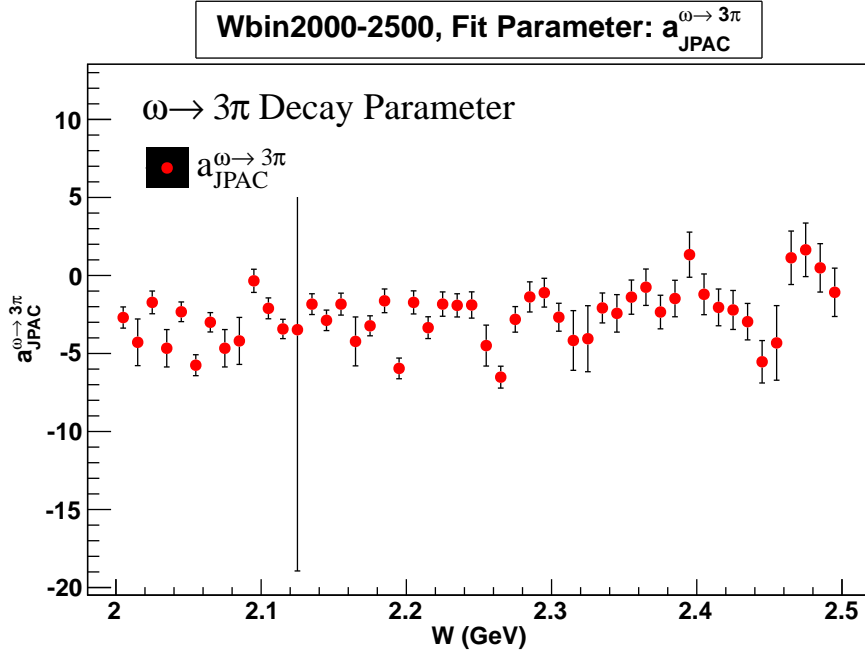


Figure 6.38: JPAC  $\omega \rightarrow 3\pi$  decay parameter,  $a_{JPAC}^{\omega \rightarrow 3\pi}$ , fitted to CLAS-g12 data for  $W : [2000-2500]$  MeV at widths of 10 MeV,  $M_\omega \pm 15$  MeV. The boundary factor used was  $\phi_{physical}$ , Eqn. 6.13

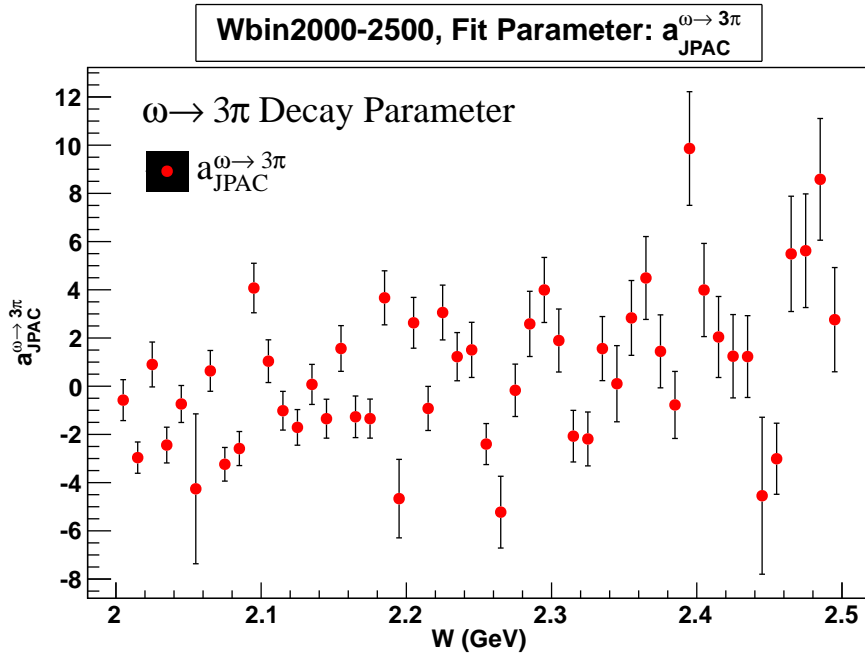


Figure 6.39: JPAC  $\omega \rightarrow 3\pi$  decay parameter,  $a_{JPAC}^{\omega \rightarrow 3\pi}$ , fitted to CLAS-g12 data for  $W : [2000-2500]$  MeV at widths of 10 MeV,  $M_\omega \pm 10$  MeV. The boundary factor used was  $\phi_{physical}$ , Eqn. 6.13

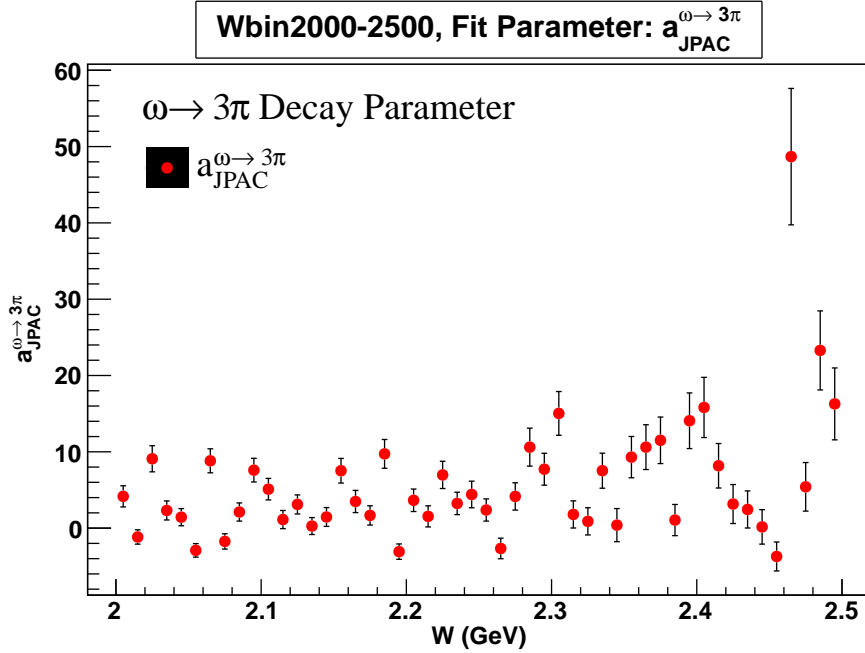


Figure 6.40: JPAC  $\omega \rightarrow 3\pi$  decay parameter,  $a_{JPAC}^{\omega \rightarrow 3\pi}$ , fitted to CLAS-g12 data for  $W : [2000 - 2500]$  MeV at widths of 10 MeV,  $M_\omega \pm 5.0$  MeV. The boundary factor used was  $\phi_{physical}$ , Eqn. 6.13

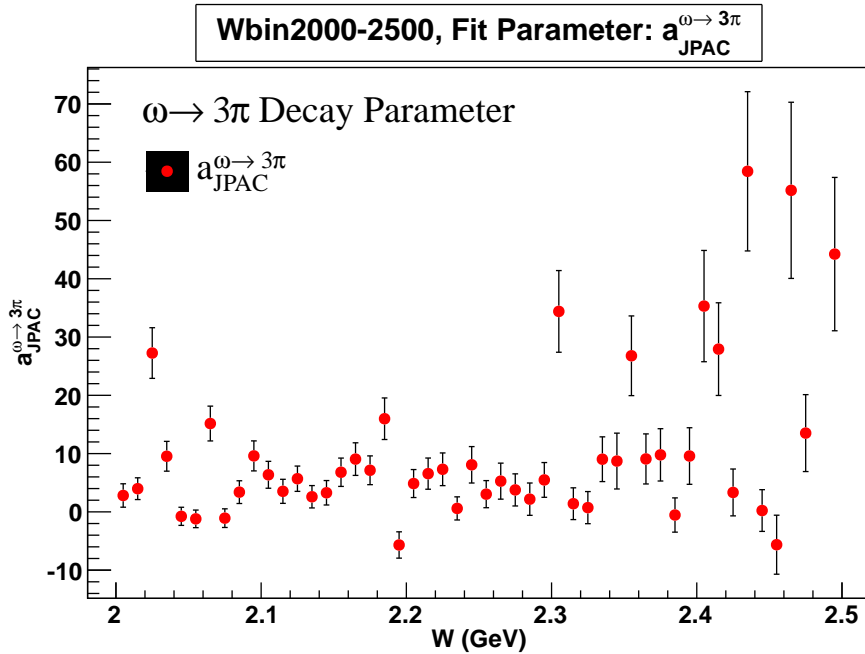


Figure 6.41: JPAC  $\omega \rightarrow 3\pi$  decay parameter,  $a_{JPAC}^{\omega \rightarrow 3\pi}$ , fitted to CLAS-g12 data for  $W : [2000 - 2500]$  MeV at widths of 2.0 MeV,  $M_\omega \pm 2.0$  MeV. The boundary factor used was  $\phi_{physical}$ , Eqn. 6.13

#### 6.4.4 CLAS-g8b JPAC $\omega \rightarrow 3\pi$ Decay Parameter

The following JPAC  $\omega \rightarrow 3\pi$  decay parameter results were extracted from the JPAC decay amplitude,  $\mathcal{F}(s, t, u, a_{JPAC}^{\omega \rightarrow 3\pi})$ , using CLAS-g8b data. The squared production amplitude,  $|\mathcal{T}|^2$ , and angular decay distribution,  $\mathcal{W}$ , of the overall fit function,  $I_{full} \propto |\mathcal{T}|^2 \mathcal{W} |\mathcal{F}|^2$ , were taken into account by weighting the detector simulated MC events with the differential cross section measurements and Schilling equation. Thus, the fit function fitted to the CLAS-g8b data took the reduced form  $I_{full} = |\vec{P}_{\pi^+} \times \vec{P}_{\pi^-}|^2 |\mathcal{F}|^2$  where the prefactor is the (squared decay plane normal) kinematic boundary factor. For these investigatory results of the JPAC decay parameter, it is important to note that the CLAS-g11a differential cross section measurements and SDMEs were used in lieu of those extracted from the CLAS-g8b data. The systematic errors for the CLAS-g8b SDMEs and JPAC decay parameter results remain to be studied and taken into account.

The fit results for the JPAC decay parameter,  $a_{JPAC}^{\omega \rightarrow 3\pi}$ , to CLAS-g8b data are ordered with respect to single and double binned fits as follows: single bins of c.m. production energy,  $W$ ; primary bins of incoming photon energy,  $E_\gamma$  with secondary bins in momentum transfer,  $t$ -Mandelstam; single bins across the  $\omega$  resonance mass,  $M_\omega$ ; and primary bins of c.m. production energy,  $W$ , with secondary bins having symmetric cuts about the omega mass mean, e.g.  $M_\omega \pm 10$  MeV.

For  $W : [1770 - 2340]$  MeV at widths of 10 MeV, Fig. 6.42, the JPAC decay parameter using  $\phi_{physical}$  as the boundary factor had an visible c.m. production energy dependence for the parameter with a spread mostly between  $a_{JPAC}^{\omega \rightarrow 3\pi} : [-10 - 0]$ . The results trend across the energy is fairly similar to that for the CLAS-g12 data, Fig. 6.18. There appear to be two peaks again, but this time located between  $W : [1770 - 1900]$  MeV. The decay parameter values were all lower than the expected  $a_{JPAC}^{\omega \rightarrow 3\pi} = +8$ . They decreased from 0 to  $-10$  with increasing energy. The source of these peaks and the overall downward slope for higher energies are unknown at this time. The latter may be related to slight variations in the omega mean of the omega mass across the c.m. production energy which needs further investigation. Focusing on the more stable region  $W : [1900 - 2300]$  MeV, also Fig. ??, the parameter values have a spread mostly from  $a_{JPAC}^{\omega \rightarrow 3\pi} : [-10 - (-6.2)]$ .

For  $E_\gamma : [1200 - 2400]$  MeV at widths of 100 MeV and  $t : [0.100 - 3.100]$  GeV<sup>2</sup> at widths of 0.100 GeV<sup>2</sup>, the JPAC decay parameter using  $\lambda$  as the boundary factor had a visible momentum transfer dependence, see sample Figs. 6.44 through 6.47. The decay parameter values with the exception of  $E_\gamma : [1700 - 1800]$  and  $t : [0.100 - 0.400]$  GeV<sup>2</sup> were negative. The trends were similar

to those for the CLAS-g12 data but the plateau values in the middle range of  $t$  were more (negative) suppressed.

Coming back to the middle region of  $W : [1900 - 2300]$ , the JPAC decay parameter was extracted using  $\phi_{physical}$  for the boundary parameter for primary bins in  $W$  at widths of 100 MeV and secondary bins in the omega mass for  $M_\omega : [650 - 900]$  MeV at widths of 10 MeV and 5 MeV. The sample results for  $W : [2000 - 2100]$  and  $M_\omega : [650 - 900]$  MeV at widths of 10 MeV and 5 MeV are respectively given in Figs. 6.48 and 6.49. Two remaining 2 pairs of results across  $W$  are given between Figs. 6.50 and 6.53. A clear dependence on both the energy and resonance mass were observed. Parameter values for the mass ranges below and above  $M_\omega : [750 - 820]$  MeV are not present due to low statistics (predominantly low Monte Carlo statistics).

Finally, for  $W : [1900 - 2340]$  at width of 10 MeV and increasingly tighter symmetric cuts about the mean of the resonance mass, i.e.  $M_\omega \pm 40, 30, 20, 15, 10, 5$  MeV, the JPAC decay parameter was extracted using  $\phi_{physical}$  for the boundary parameter, see Figs. 6.54 through 6.60. The decay parameter increases across the energy, again migrating from from negative values towards positive values as the symmetric cuts approach the mean value of the  $\omega$  mass. As the width of the mass approaches zero and the mass itself approaches its mean value (and roughly the PDG value), the JPAC decay parameter shifts from the negative values of Fig. 6.54 towards the expected positive value region. The shift towards positive values is not as pronounced as it was for the CLAS-g12 results; however, the trend is the same.

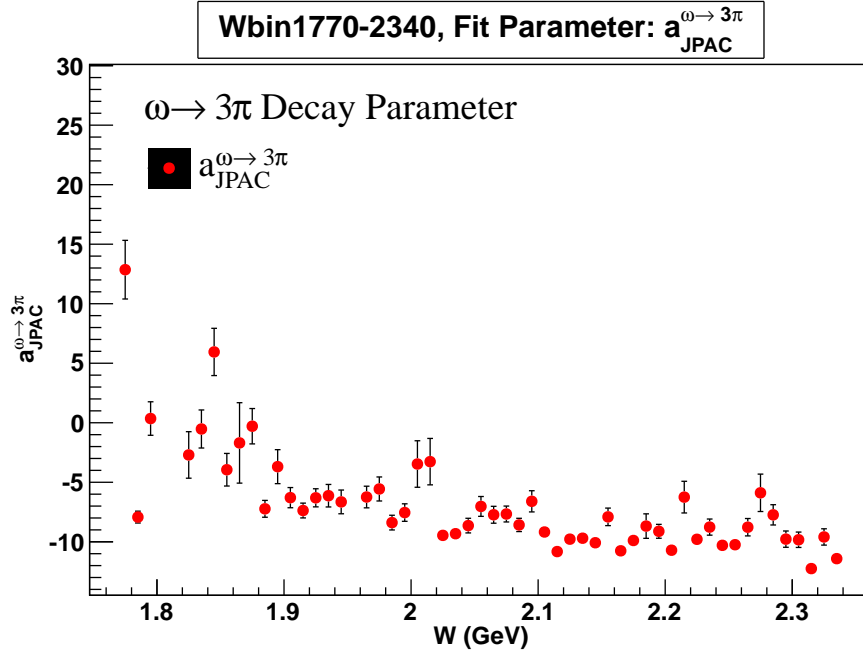


Figure 6.42: JPAC  $\omega \rightarrow 3\pi$  decay parameter,  $a_{JPAC}^{\omega \rightarrow 3\pi}$ , fitted to CLAS-g8b data for  $W : [1770 - 2340]$  MeV at widths of 10 MeV. The boundary factor used was  $\phi_{physical}$ , Eqn. 6.13

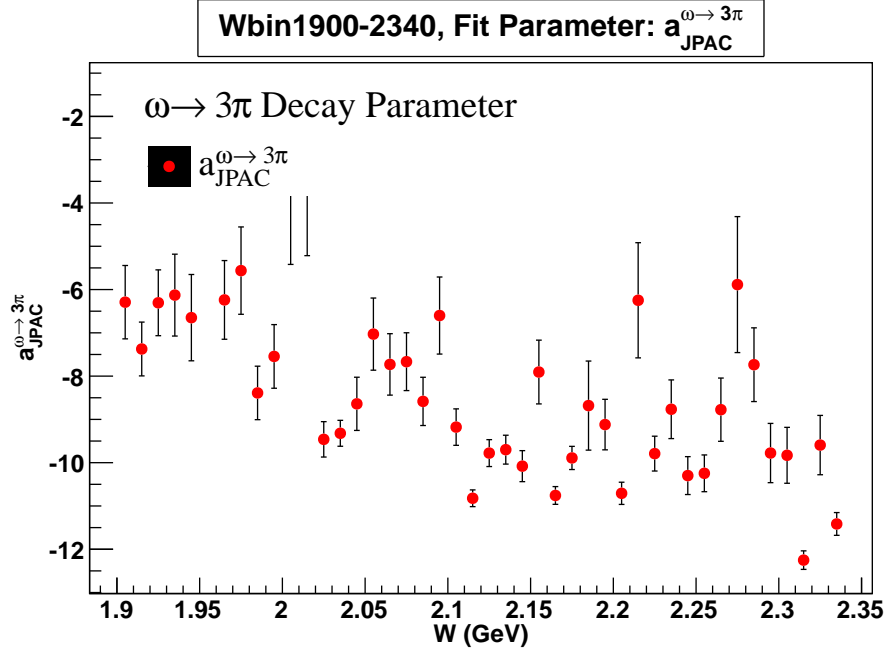


Figure 6.43: JPAC  $\omega \rightarrow 3\pi$  decay parameter,  $a_{JPAC}^{\omega \rightarrow 3\pi}$ , fitted to CLAS-g8b data for  $W : [1900 - 2340]$  MeV at widths of 10 MeV. The boundary factor used was  $\phi_{physical}$ , Eqn. 6.13

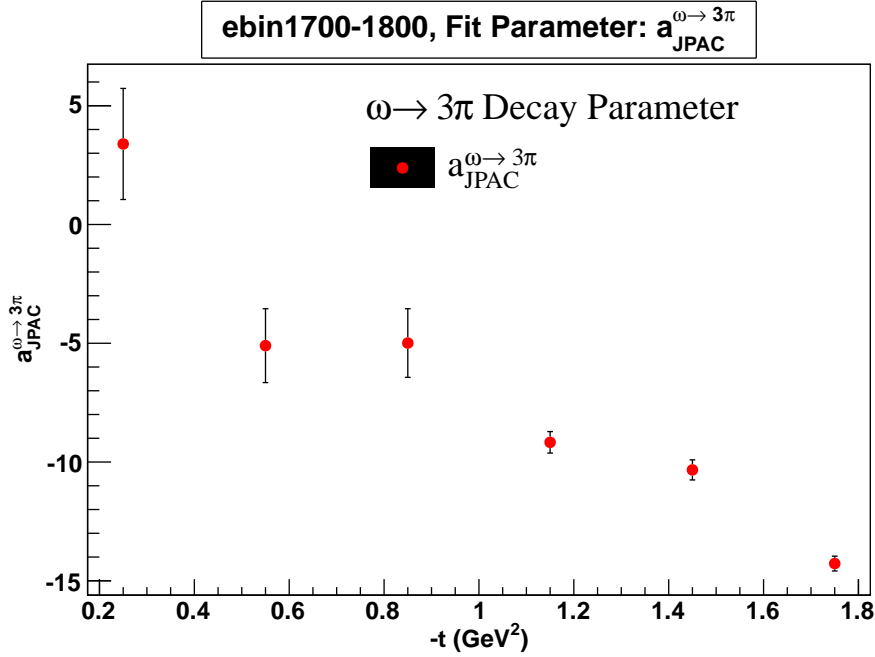


Figure 6.44: JPAC  $\omega \rightarrow 3\pi$  decay parameter,  $a_{JPAC}^{\omega \rightarrow 3\pi}$ , fitted to CLAS-g8b data for  $E_\gamma : [1700 - 1800]$  MeV and  $t : [0.100 - 3.100]$  GeV<sup>2</sup> at widths of 0.100 GeV<sup>2</sup>. The boundary factor used was  $\lambda$ , Eqn. 4.6

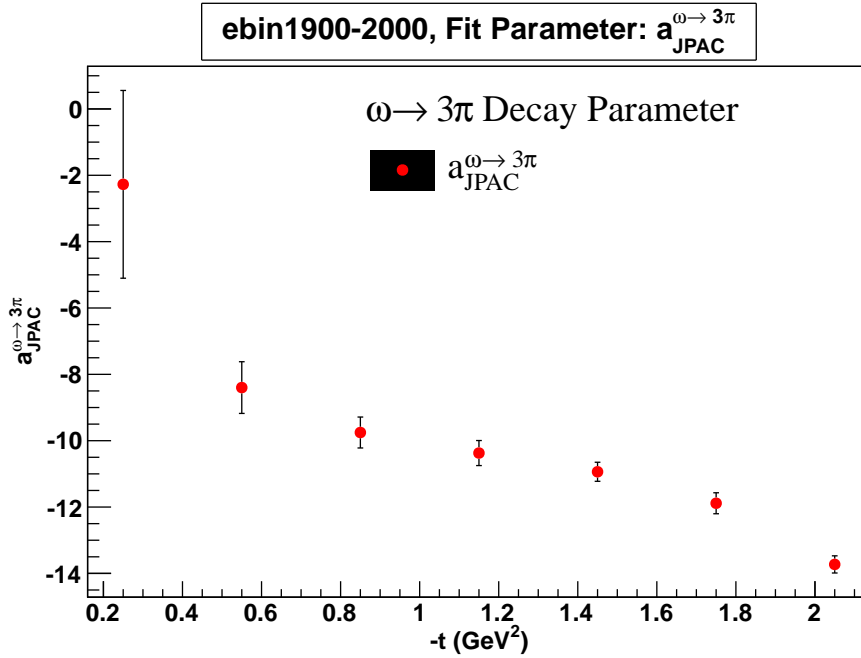


Figure 6.45: JPAC  $\omega \rightarrow 3\pi$  decay parameter,  $a_{JPAC}^{\omega \rightarrow 3\pi}$ , fitted to CLAS-g8b data for  $E_\gamma : [1900 - 2000]$  MeV and  $t : [0.100 - 3.100]$  GeV<sup>2</sup> at widths of 0.100 GeV<sup>2</sup>. The boundary factor used was  $\lambda$ , Eqn. 4.6

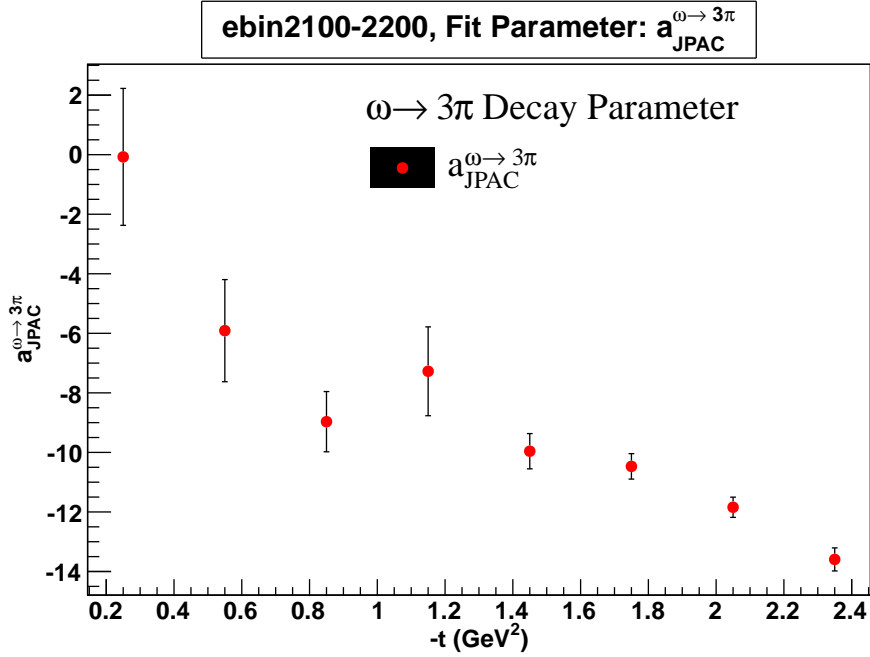


Figure 6.46: JPAC  $\omega \rightarrow 3\pi$  decay parameter,  $a_{JPAC}^{\omega \rightarrow 3\pi}$ , fitted to CLAS-g8b data for  $E_\gamma : [2100 - 2200]$  MeV and  $t : [0.100 - 3.100]$  GeV<sup>2</sup> at widths of 0.100 GeV<sup>2</sup>. The boundary factor used was  $\lambda$ , Eqn. 4.6

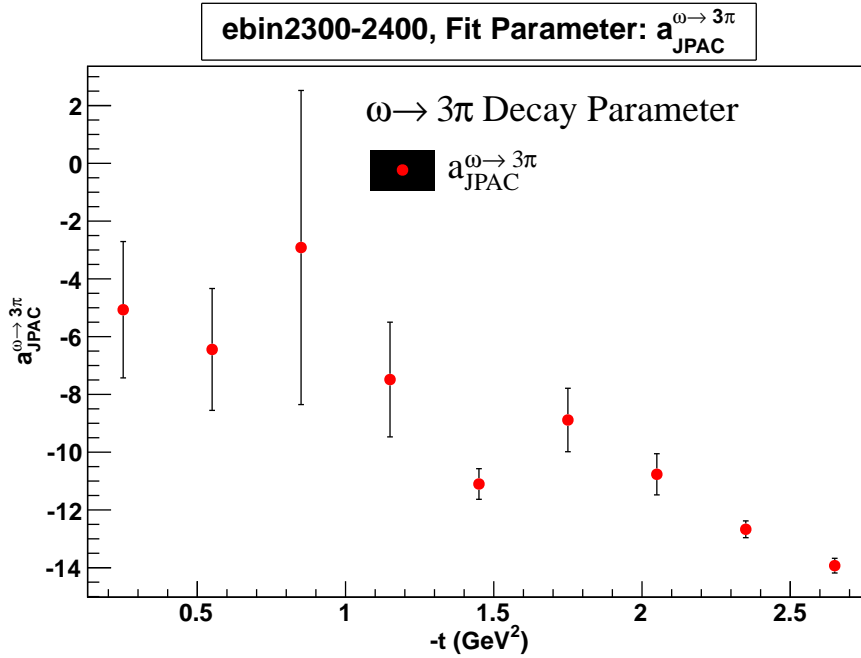


Figure 6.47: JPAC  $\omega \rightarrow 3\pi$  decay parameter,  $a_{JPAC}^{\omega \rightarrow 3\pi}$ , fitted to CLAS-g8b data for  $E_\gamma : [2300 - 2400]$  MeV and  $t : [0.100 - 3.100]$  GeV<sup>2</sup> at widths of 0.100 GeV<sup>2</sup>. The boundary factor used was  $\lambda$ , Eqn. 4.6

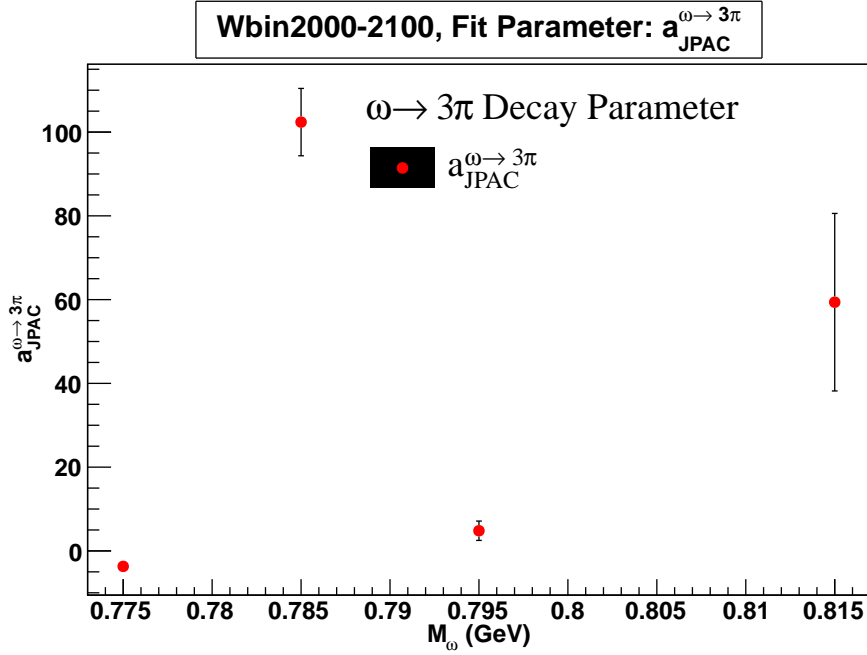


Figure 6.48: JPAC  $\omega \rightarrow 3\pi$  decay parameter,  $a_{JPAC}^{\omega \rightarrow 3\pi}$ , fitted to CLAS-g8b data for  $W : [2000 - 2100]$  MeV and  $M_\omega : [740 - 820]$  MeV at widths of 10 MeV. The boundary factor used was  $\phi_{physical}$ , Eqn. 6.13

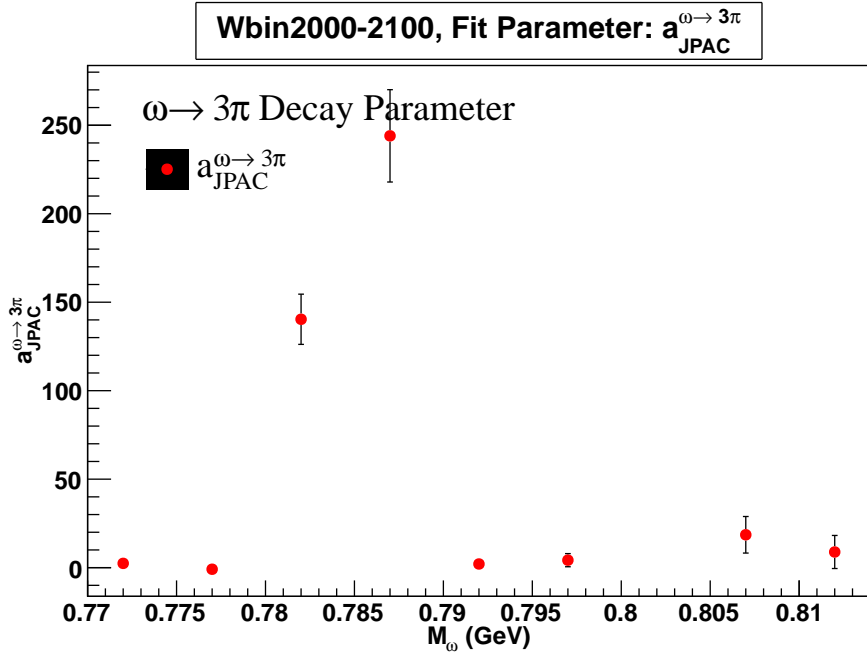


Figure 6.49: JPAC  $\omega \rightarrow 3\pi$  decay parameter,  $a_{JPAC}^{\omega \rightarrow 3\pi}$ , fitted to CLAS-g8b data for  $W : [2000 - 2100]$  MeV and  $M_\omega : [740 - 820]$  MeV at widths of 5 MeV. The boundary factor used was  $\phi_{physical}$ , Eqn. 6.13

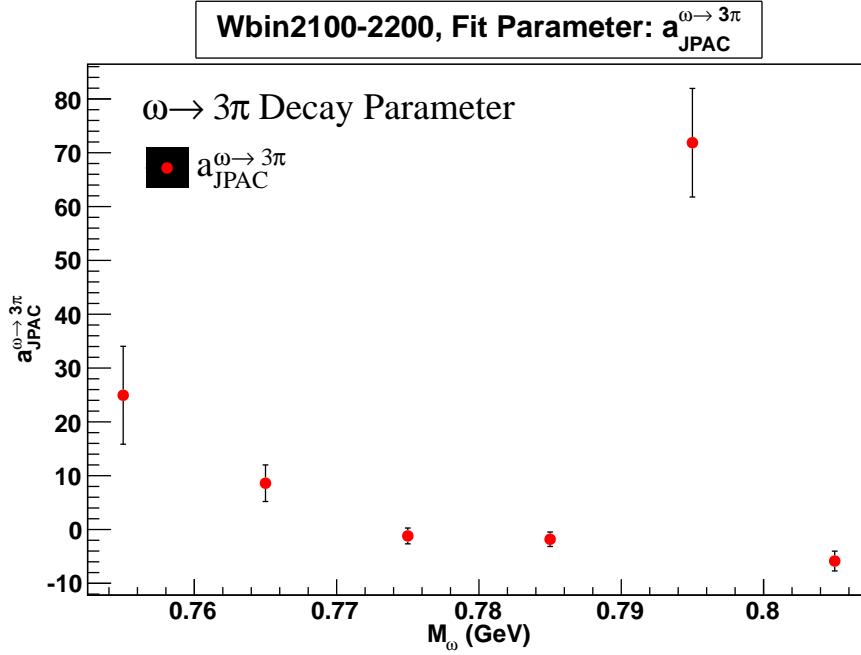


Figure 6.50: JPAC  $\omega \rightarrow 3\pi$  decay parameter,  $a_{JPAC}^{\omega \rightarrow 3\pi}$ , fitted to CLAS-g8b data for  $W : [2100 - 2200]$  MeV and  $M_\omega : [740 - 820]$  MeV at widths of 10 MeV. The boundary factor used was  $\phi_{physical}$ , Eqn. 6.13

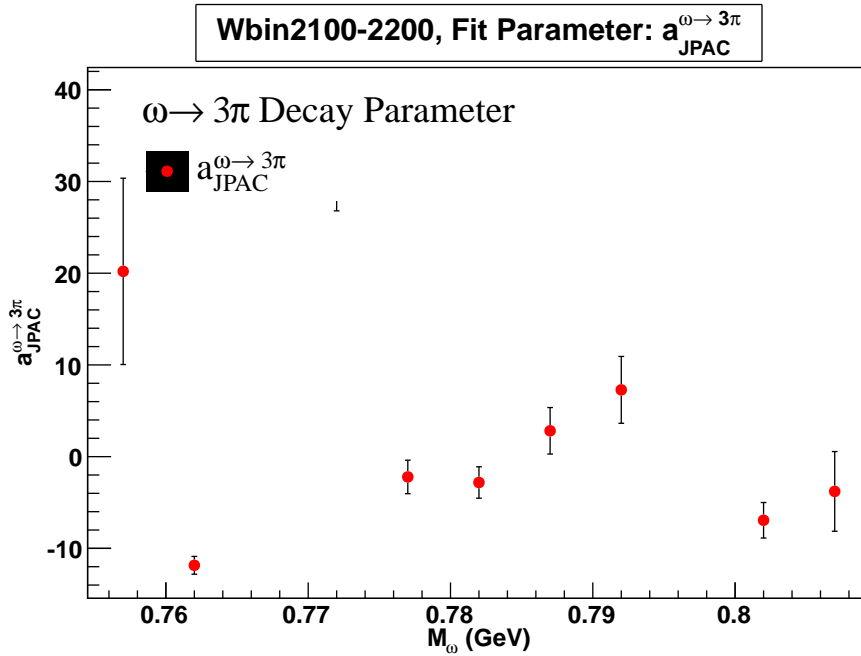


Figure 6.51: JPAC  $\omega \rightarrow 3\pi$  decay parameter,  $a_{JPAC}^{\omega \rightarrow 3\pi}$ , fitted to CLAS-g8b data for  $W : [2100 - 2200]$  MeV and  $M_\omega : [740 - 820]$  MeV at widths of 5 MeV. The boundary factor used was  $\phi_{physical}$ , Eqn. 6.13

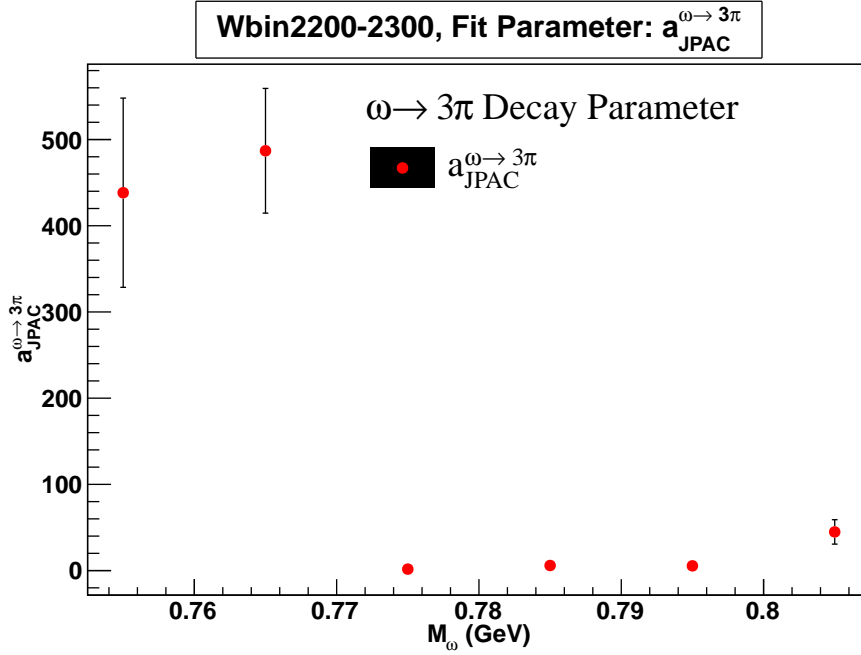


Figure 6.52: JPAC  $\omega \rightarrow 3\pi$  decay parameter,  $a_{JPAC}^{\omega \rightarrow 3\pi}$ , fitted to CLAS-g8b data for  $W : [2200 - 2300]$  MeV and  $M_\omega : [740 - 820]$  MeV at widths of 10 MeV. The boundary factor used was  $\phi_{physical}$ , Eqn. 6.13

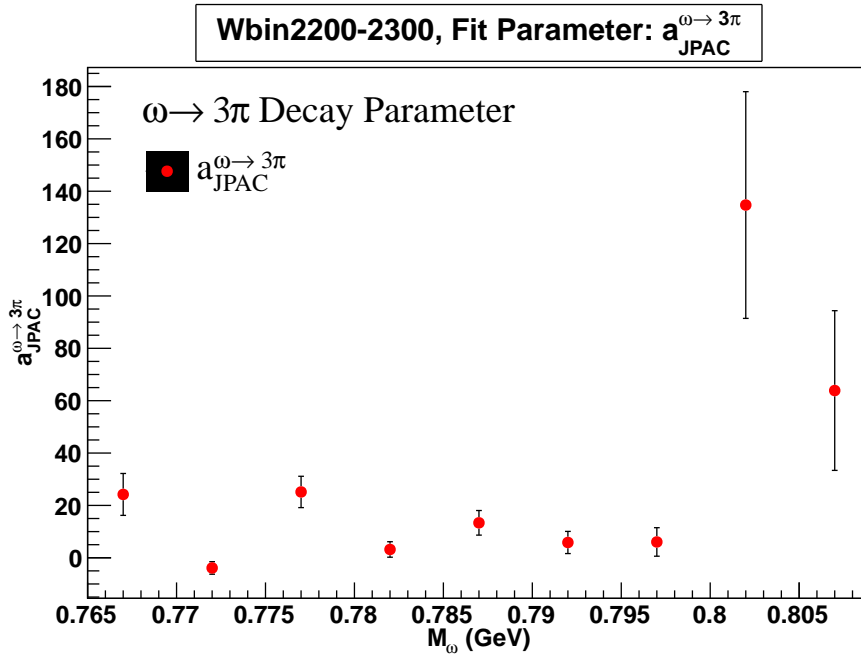


Figure 6.53: JPAC  $\omega \rightarrow 3\pi$  decay parameter,  $a_{JPAC}^{\omega \rightarrow 3\pi}$ , fitted to CLAS-g8b data for  $W : [2200 - 2300]$  MeV and  $M_\omega : [740 - 820]$  MeV at widths of 5 MeV. The boundary factor used was  $\phi_{physical}$ , Eqn. 6.13

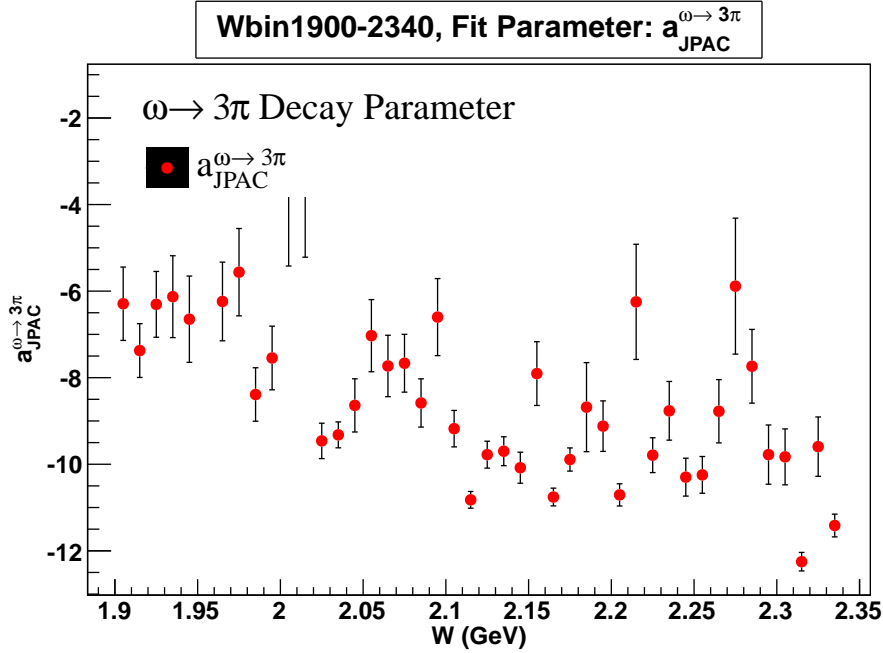


Figure 6.54: JPAC  $\omega \rightarrow 3\pi$  decay parameter,  $a_{JPAC}^{\omega \rightarrow 3\pi}$ , fitted to CLAS-g8b data for  $W : [1900 - 2340]$  MeV at widths of 10 MeV. The boundary factor used was  $\phi_{physical}$ , Eqn. 6.13

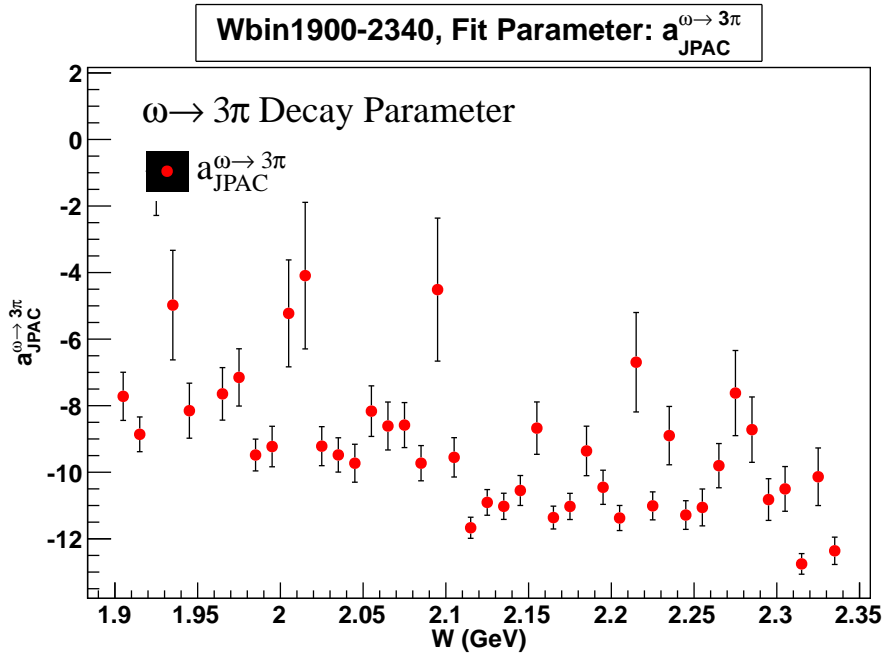


Figure 6.55: JPAC  $\omega \rightarrow 3\pi$  decay parameter,  $a_{JPAC}^{\omega \rightarrow 3\pi}$ , fitted to CLAS-g8b data for  $W : [1900 - 2340]$  MeV at widths of 10 MeV,  $M_\omega \pm 40$  MeV. The boundary factor used was  $\phi_{physical}$ , Eqn. 6.13

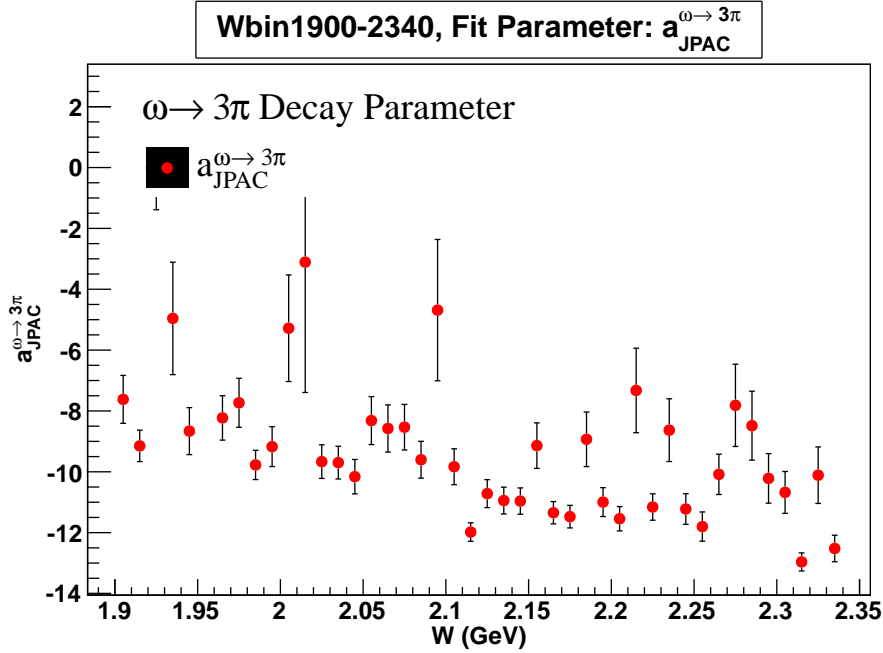


Figure 6.56: JPAC  $\omega \rightarrow 3\pi$  decay parameter,  $a_{JPAC}^{\omega \rightarrow 3\pi}$ , fitted to CLAS-g8b data for  $W : [1900-2340]$  MeV at widths of 10 MeV,  $M_\omega \pm 30$  MeV. The boundary factor used was  $\phi_{physical}$ , Eqn. 6.13

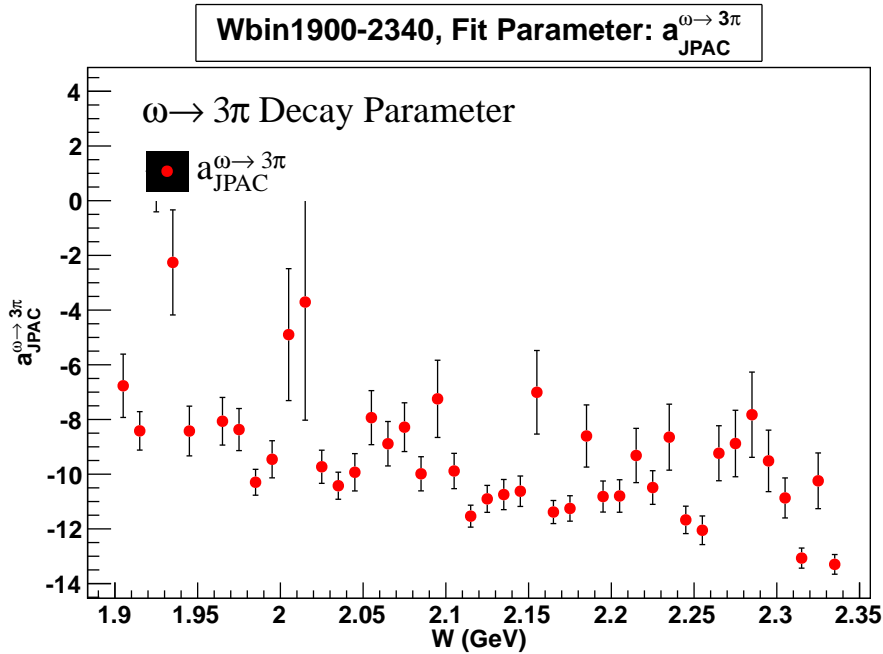


Figure 6.57: JPAC  $\omega \rightarrow 3\pi$  decay parameter,  $a_{JPAC}^{\omega \rightarrow 3\pi}$ , fitted to CLAS-g8b data for  $W : [1900-2340]$  MeV at widths of 10 MeV,  $M_\omega \pm 20$  MeV. The boundary factor used was  $\phi_{physical}$ , Eqn. 6.13

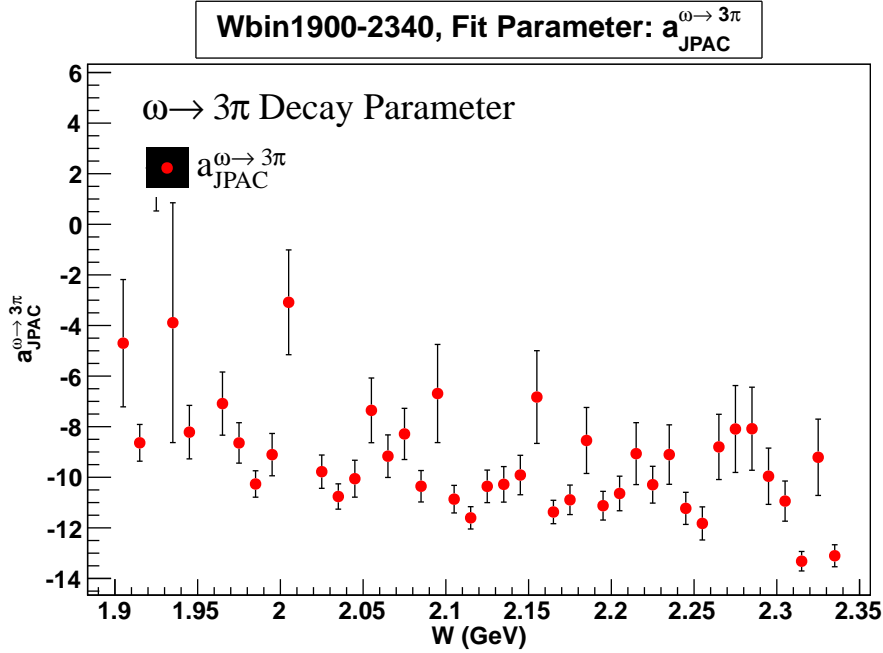


Figure 6.58: JPAC  $\omega \rightarrow 3\pi$  decay parameter,  $a_{JPAC}^{\omega \rightarrow 3\pi}$ , fitted to CLAS-g8b data for  $W : [1900-2340]$  MeV at widths of 10 MeV,  $M_\omega \pm 15$  MeV. The boundary factor used was  $\phi_{physical}$ , Eqn. 6.13

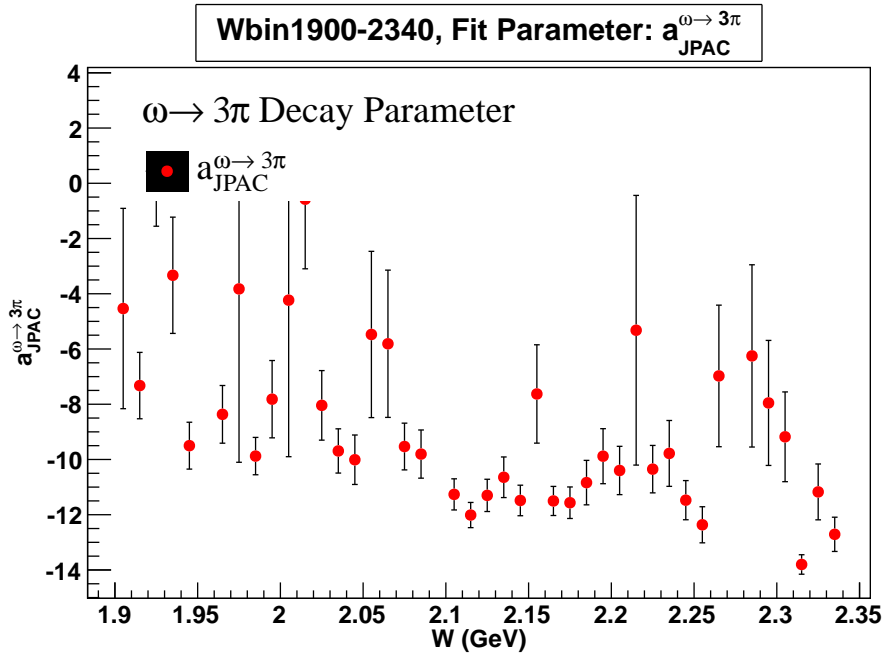


Figure 6.59: JPAC  $\omega \rightarrow 3\pi$  decay parameter,  $a_{JPAC}^{\omega \rightarrow 3\pi}$ , fitted to CLAS-g8b data for  $W : [1900-2340]$  MeV at widths of 10 MeV,  $M_\omega \pm 10$  MeV. The boundary factor used was  $\phi_{physical}$ , Eqn. 6.13

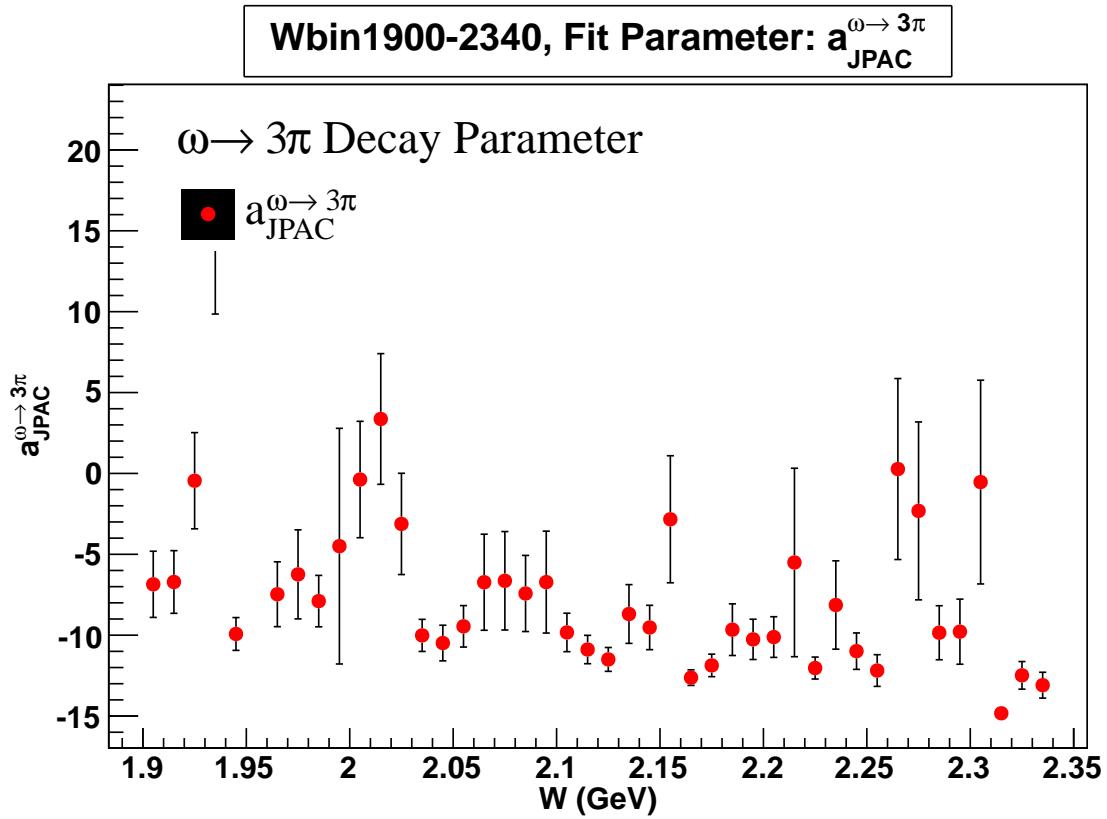


Figure 6.60: JPAC  $\omega \rightarrow 3\pi$  decay parameter,  $a_{JPAC}^{\omega \rightarrow 3\pi}$ , fitted to CLAS-g8b data for  $W$  : [1900 – 2340] MeV at widths of 10 MeV,  $M_\omega \pm 5$  MeV. The boundary factor used was  $\phi_{physical}$ , Eqn. 6.13

# CHAPTER 7

## CONCLUSION

### 7.1 Conclusion

As part of the Experimental Hadronic Nuclear Group at Florida State University and in close cooperation with the Joint Physics Analysis Center (JPAC) at Jefferson National Laboratory, I conducted a Dalitz plot analysis of the  $\omega \rightarrow 3\pi$  decay. Results were presented for the spin density matrix elements (SDMEs) and JPAC decay parameter which were respectively extracted from fitting the Schilling equation and JPAC  $\omega \rightarrow 3\pi$  decay amplitude to two independent sets of data. These were first time fits of the JPAC decay amplitude to real data. The fits were employed using the unbinned, event based, log likelihood method.

The two data sets used in my analysis originated from the CLAS-g8b and CLAS-g12 photoproduction experiments held during the 2005 and 2008 summer run periods, respectively. In both cases,  $\omega$  vector mesons were photoproduced off a fixed, unpolarized, liquid hydrogen target. The reconstructed events,  $\gamma p \rightarrow p\omega \rightarrow p\pi^+\pi^-\{\pi^0\}$ , for both samples were prepared at FSU. While the photon beam polarization for the CLAS-g8b and CLAS-g12 experiments differed, the polarization information of the respectively linearly and circularly polarized events was discarded in order to compare results from the two unpolarized data sets.

The Dalitz distribution was modelled by three factors: a kinematic boundary factor associated with the spin-parity transition of the decay; a helicity dependent distribution associated with the decay angles; and a helicity independent distribution associated with the dynamics of the decay. The latter factors were taken into account by the Schilling equation and an isobar based, covariant decay amplitude supplemented by JPAC.

The CLAS-g8b and CLAS-g12 SDMEs were each compared to those extracted from the CLAS-g11a group [7]. The two comparison were found to be in fair agreement with one another. Although not always the case, deviations in of the CLAS-g8b or CLAS-g12 SDME values with respect to those of CLAS-g11a tend to appear more frequently towards the forward angle region of the detector. Yet, the trends are consistent for all three parameter values across the majority of the c.m. production

energy and the resonance cosine production angle. Further refinement of the CLAS-g8b and CLAS-g12 SDMEs is necessary. Systematic error were not taken into account and need to be addressed. Also, there is a known 5% disagreement between the g12 and g11a cross-sections at this time. The reasons behind this difference, while unknown at the time, may also play a role in the observed differences between the results.

Further work is to be done in terms of investigating the fit results for the JPAC  $\omega \rightarrow 3\pi$  decay parameter,  $a_{JPAC}^{\omega \rightarrow 3\pi}$ . The observed peaks and lift in the results respectively located at the low and high end of center of mass energy,  $W$ , warrant further experimental investigation; however, upon exhaustive investigation of the parameter behavior over various binning and cuts to the data, it is clear that several kinematic dependencies of the decay parameter have been established. Namely, through independent fits to the CLAS-g12 and CLAS-g8b data, we observed an energy, momentum transfer, and resonance mass dependence of the parameter. Despite the lower statistics of the CLAS-g8b data, the results of the two data sets were mostly consistent in terms of trends if not in value.

Also, our investigation of symmetric cuts about the  $\omega$  mass has uncovered that the JPAC decay parameter value increases in value as tighter cuts are imposed about the mean. We suspect that as our cuts approach the nominal PDG value for the  $\omega$  mass, the parameter value approaches most closely towards the theoretically supposed value. This would be consistent with the theory having been fit to the PDG mass value. This observed behavior is most clear from our fits to the CLAS-g12 data; whereas, the effect is quite a bit more suppressed for the lower statistic g8b data set. Finally, systematic error analysis for both of these fit results must be investigated further.

In order to perform my analysis, I set up and established a framework of data analysis and partial-wave analysis tools. The central partial wave fitting framework was the latest AmpTools (v0.9.2) PWA framework developed at Indiana University. Making use of C++, ROOT, and bash scripting, I extended the framework to include data modification routines, an input data comparison routine, a quality checks routine, a fitter consistency routine, a best of  $N$  fits routine, input and output data comparison routine, and double binned fitting options for up to 5 bin types. The user-friendly framework was current and tested.

Lastly, since the  $\phi \rightarrow 3\pi$  decay is a case similar to that of the  $\omega \rightarrow 3\pi$  decay, the current framework in place for the  $\omega$  decay can be readily modified for a partial wave analysis of the

$\phi$  decay. While we do not have g12 data for this reaction, data likely will be obtained for the reaction in the near future from the GlueX experiment held in Hall D at JLAB. It would be quite exciting to see how the two analyses of light meson decays would compare.

## 7.2 Future Prospects

The next steps with the Dalitz plot analysis for the  $\omega \rightarrow 3\pi$  involve searching for the cause(s) of instabilities within the fit results for the JPAC  $\omega \rightarrow 3\pi$  decay parameter,  $a_{JPAC}^{\omega \rightarrow 3\pi}$ . Once the refinement of the g12 cross-section is complete, code is in place to obtain the parameters of the Dalitz expansion amplitude. These parameters provide a means for comparison between other data sets and theorists models. Plus, systematic errors with these fit results will need to be pursued.

In terms of performing another analyses on light vector meson decays, a future research goal may proceed with a Dalitz plot analysis for the  $\phi \rightarrow 3\pi$  decay. For one, GlueX is expected to obtain high statistics data of both  $\omega, \phi \rightarrow 3\pi$  reactions. Should one reconstruct and observe the  $\phi$  resonance for the like decay channel, my current framework is well suited for an immediate Dalitz plot analysis of the  $\phi \rightarrow 3\pi$  decay. Also, a search for any previous analyses on this decay channel which may have been performed by the groups involved with its detection (the KLOE I experiment) and listing in the Particle Data Group (PDG) book [8] would be advisable. In the end, the two analyses together, i.e. the  $\omega, \phi \rightarrow 3\pi$  decays, would be of great comparative interest in terms of Dalitz plot analyses and JPAC decay amplitude fit results. These results would serve as additional tests of the JPAC isobar model's ability to properly account for and render insight into the dynamics underlying these three-body strong decays.

# REFERENCES

- [1] Florida State University, Private Communication with Zulkaida Akbar, (2016)
- [2] K. Schilling, P. Seyboth and G. Wolf, “On The Analysis of Vector-Meson Production By Polarized Photons”, Nucl. Phys. B 15, 397 (1970) [Erratum-ibid. B 18, 332 (1970)]
- [3] I. V. Danilkin, C. Fernández-Ramírez, P. Guo, V. Mathieu, D. Schott, M. Shi and A. P. Szczepaniak, “Dispersive analysis of  $\omega/\phi \rightarrow 3\pi, \pi\gamma^*$ ,” Phys. Rev. D 91, no. 9, 094029 (2015) [arXiv:1409.7708 hep-ph]
- [4] H. Matevosyan, R. Mitchell, M. Shepherd, and L. Gibbons, “AmpTools: A Utility Library for Performing Amplitude Analysis on Particle Physics Data”, version 0.9.2, 25 August 2016, [http://amptools.sourceforge.net/index.php/Main\\_Page](http://amptools.sourceforge.net/index.php/Main_Page)
- [5] S.U. Chung, “Formulas for Partial Wave Analysis: Version II”, BNL preprint BNL-QGS-93-05 (1999)
- [6] F. James, “MINUIT: Functional Minimization and Error Analysis,” Reference Manual v94.1, CERN Program Library Long Writeup D506, (1994)  
<http://seal.web.cern.ch/seal/snapshot/work-packages/mathlibs/minuit/>  
<https://root.cern.ch/sites/d35c7d8c.web.cern.ch/files/minuit.pdf>
- [7] M. Williams, “Measurement of Differential Cross Sections and Spin Density Matrix Elements along with a Partial Wave Analysis for  $\gamma p \rightarrow p\omega$  using CLAS at Jefferson Lab,” Ph.D. Thesis, Carnegie Mellon University, 2007
- [8] K.A. Olive et al. (Particle Data Group), Chin. Phys. C, 38, 090001 (2014)
- [9] SLAC-MIT-CIT Collaboration, “Proposals for Initial Electron Scattering Experiments Using the SLAC Spectrometer Facilities,” SLAC Proposal No. 4 (January 1966)
- [10] E.D. Bloom et. al., Phys. Rev. Lett. 23, 930 (1969)
- [11] M. Breidenbach et. al., Phys. Rev. Lett. 23, 935 (1969)
- [12] M. Gell-Mann. “A Schematic Model of Baryons and Mesons”, Phys. Lett., 8(3):214-215, (1964)
- [13] G. Zweig, “An SU(3) Model for Strong Interaction Symmetry and Its Breaking”, CERN preprint 8182/TH.401, (1964)
- [14] H. Fritzsch, M. Gell-Mann, and H. Leutwyler, Phys. Lett. 47B 365, (1973)

- [15] H. Fritzsch, “The History of QCD”, Cern Courier, International Journal of High-Energy Physics, Sept. 27, 2012
- [16] D. Galbraith, An information graphic of the Standard Model of Particle Physics, 2013, <http://davidgalbraith.org/portfolio/ux-standard-model-of-the-standard-model/>
- [17] F. Englert, R. Brout, “Broken Symmetry and the Mass of Gauge Vector Mesons”, Phys. Rev. Lett. 13 (9): 321-23 (1964)
- [18] P. Higgs, “Broken Symmetries and the Masses of Gauge Bosons”, Phys. Rev. Lett. 13 (16): 508-509 (1964)
- [19] G. Guralnik, C. R. Hagen, T. W. B. Kibble, “Global Conservation Laws and Massless Particles”, Phys. Rev. Lett. 13 (20): 585-587 (1964)
- [20] J. Beringer et. al., Particle Data Group, PRD86, 010001 (2013), <http://pdg.lbl.gov>
- [21] C. N. Yang, R. Mills, “Conservation of Isotopic Spin and Isotopic Gauge Invariance”, Phys. Rev. 96 (1): 191-195 (1954)
- [22] The Rampages Blog of ThoughtVectors, An illustration of hadrons with respective colorless color-charge combinations of quark constituents, July 10, 2014, <https://rampages.us/almahmouda/>
- [23] D. J. Gross and F. Wilczek, “Ultraviolet Behavior of Non-Abelian Gauge Theories”, Phys. Rev. Lett., 30 (26), 1343, (1973)
- [24] S. Bethke, “Experimental Tests of Asymptotic Freedom”, 2008 arXiv:hep-ex/0606035v2
- [25] H. D. Politzer, “Reliable Perturbative Results for Strong Interactions?”, Phys. Rev. Lett., 30 (26), 1346, (1973)
- [26] Clay Mathematics Institute, “Yang-Mills Existence and Mass Gap”, <http://www.claymath.org/millennium-problems/yang-mills-and-mass-gap>
- [27] E. Noether, “Invariante Variationsprobleme”, Nachr. D. König. Gesellsch. D. Wiss. Zu Göttingen, Math-phys. Klasse. 235-257 (1918)
- [28] N. N. Khuri and S. B. Treiman, Phys. Rev. 119, 1115 (1960)
- [29] R. Pasquier and J. Y. Pasquier, Phys. Rev. 177, 2482 (1969)
- [30] I. J. R. Aitcheson, “Unitarity, Analyticity and Crossing Symmetry in Two- and Three-hadron Final State Interactions”, 9 July 2015, arXiv:1507.02697v1

- [31] A. Szczepaniak, “Analytical Improvements to the Breit-Wigner Isobar Models”, 2 October 2015, arXiv:1510.00695v1
- [32] I. J. R. Aitchison and R. J. A. Golding, *J. Phys. G4*, 43 (1978)
- [33] F. Niecknig, B. Kubis, and S. P. Schneider, *Eur. Phys. J. C72*, 2014 (2012)
- [34] PWA 8 / ATHOS 3 Talks, The International Workshop on Partial Wave Analysis for Hadron Spectroscopy, <https://physics.columbian.gwu.edu/pwa-8-athos-3>
- [35] C. Terschlüsen, B. Strandberg, S. Leupold, and F. Eichstädt, *Eur. Phys. J. A49*, 116 (2013)
- [36] K. Peters, “Dalitz Plot Analysis Techniques” Talk, Cornell University, 2004, [http://www.lns.cornell.edu/~journalc/public/talk/040506\\_Peters.pdf](http://www.lns.cornell.edu/~journalc/public/talk/040506_Peters.pdf)
- [37] E. Abboud, “On Viviani’s Theorem and its Extensions”, 12 April 2009, arXiv:0903.0753v3
- [38] C. Zemach, *Phys. Rev.* 133, B1201 (1964); 140, B97 (1965)
- [39] General Photograph Repository for Jefferson Laboratory, <https://www.jlab.org/photos>
- [40] Mission Statement of Jefferson Laboratory, [https://www.jlab.org/sites/default/files/documents/hr/Jefferson Lab Mission Statement.pdf](https://www.jlab.org/sites/default/files/documents/hr/Jefferson%20Lab%20Mission%20Statement.pdf)
- [41] Flickr Site of Jefferson Laboratory, <https://www.flickr.com/photos/jeffersonlab/12599705145>
- [42] R. Kazimi et. al., *Proceedings of EPAC 2004*, 1512 (2004)
- [43] 5 cell Cryostat Cavity Display, Jefferson Lab Site Tour, <http://education.jlab.org/sitetour/ccentercavity.l.html>
- [44] S. Gagnon, LINAC Cryostat Accelerator Animation, Jefferson Lab Site Tour, <http://education.jlab.org/sitetour/guidedtour05.l.alt.gif>
- [45] Schematic Diagram of Hall B with Photon Tagging System and CLAS, [http://faculty.fiu.edu/~baraue/images/BR\\_HallB.gif](http://faculty.fiu.edu/~baraue/images/BR_HallB.gif)
- [46] J. Goetz, “ $\Xi$  Hyperon Photoproduction from Threshold to 5.4 GeV with the CEBAF Large Acceptance Spectrometer”, Ph.D. Thesis, The University of California Los Angeles, (2010)
- [47] D. I. Sober et al. “The Bremsstrahlung Tagged Photon Beam in Hall B at JLab”, *Nucl. Instrum. Meth.*, A440:263-284, (2000)

- [48] S. Christo, The g11a and g12 Target Cell, [http://www.jlab.org/christo/g11a\\_target.html](http://www.jlab.org/christo/g11a_target.html)
- [49] Y. G. Sharabian et. al., “A New Highly Segmented Start Counter for the CLAS Detector”, Nucl. Instr. Meth. A 556, 246 (2006)
- [50] M. D. Mestayer et. al., “The CLAS Drift Chamber System”, Nucl. Instr. and Meth. A, 449:81-111, (2000)
- [51] JLab Hall B Photo Album, The CLAS Toroidal Magnet, <https://www.jlab.org/Hall-B/album/CLAS%20-%20Magnets/index.html>
- [52] A. J. Street et al., “Final Site Assembly and Testing of the Superconducting Toroidal Magnet for the CEBAF Large Acceptance Spectrometer (CLAS)”, IEEE Trans. Mag. 32, No. 4, 2074 (1996)
- [53] E. S. Smith, “The Time-Of-Flight System for CLAS”, Nucl. Instr. and Meth. A, 432:265-298, (1999)
- [54] D. Keller. CLAS-NOTE, Jefferson Lab, 2010-015, (2010)
- [55] E. Pasyuk, “Energy Loss Corrections for Charged Particles in CLAS,” CLAS-NOTE, (2007-016), (2007)
- [56] M. Williams, C. A. Meyers, “Kinematic Fitting in CLAS”, CLAS-NOTE (2003-017), (2003)
- [57] M. Williams, M. Bellis, C. A. Meyers, “Signal Signals from Non-Interfering Backgrounds Using Probabilistic Event Weightings”, [physics-data-an] 21 April 2008, arXiv:0804.3382v1
- [58] g12 Collaboration, “g12 Analysis Procedures, Statistics and Systematics,” (2016)
- [59] M. Jacob and G. C. Wick, “On the General Theory of Collisions for Particles with Spin”, March 23, 1959; Annals of Physics 281, 774 799 (2000)
- [60] S. M. Berman and M. Jacob, “Systematics of Angular and Polarization Distributions in Three Body Decays,” SLAC-PUB-73, January, 1964
- [61] S. M. Berman and M. Jacob, “Spin and Parity in Two-Step Decay Processes,” SLAC-REF-43, May, 1965
- [62] H. E. Haber, “Spin Formalisms and Applications to New Physics Searches,” 25 May 1994 arXiv:hep-ph/9405376v1
- [63] S. U. Chung, “Spin Formalisms: Updated Version,” 29 July 2014

- [64] L. Brits, “Euler Angles Drawn in Inkscape,” Wikipedia,  
[https://en.wikipedia.org/wiki/Euler\\_angles](https://en.wikipedia.org/wiki/Euler_angles)
  
- [65] Joint Physics Analysis Center, “JPAC  $\omega \rightarrow 3\pi$  Decay Amplitude Interactive Online Routine”,  
April 2015, <http://cgl.soic.indiana.edu/jpac/w3pi.php>
  
- [66] M.Williams, “How Good Are Your Fits? Unbinned Multivariate Goodness-of-fit Tests in High  
Energy Physics”, 16 August 2010, arXiv:1006.3019v2
  
- [67] P. Glasserman, “Monte Carlo Methods in Financial Engineering”, Springer, pgs. 58-59, (2003)

# BIOGRAPHICAL SKETCH

## EDUCATION

Ph.D. Candidate, Experimental Hadronic Nuclear Physics, Expected December 2016

Florida State University, Tallahassee FL

GPA: 3.844/4.0

M.S., Physics, Awarded May 2012

Florida State University, Tallahassee FL

GPA: 3.844/4.0

M.S., Theoretical Nuclear Physics, Graduated May 2011

University of Idaho, Moscow ID

GPA: 3.83/4.0

B.S., Physics, Graduated May 2009

University of Idaho, Moscow ID

GPA: Institution 3.63/4.0; Overall 3.42/4.0

## PUBLICATIONS

R. Machleidt, Q. MacPherson, E. Marji, R. Winzer, Ch. Zeoli, D. R. Entem

Proceedings of the 20th International IUPAP Conference on Few-Body

Problems in Physics, 2012, Fukuoka, Japan.

Published in “Recent Progress in the Theory of Nuclear Forces”,

DOI 10.1007/s00601-012-0561-5, Springer, arXiv:1210.0992.

Ch. Zeoli, R. Machleidt, D. R. Entem

Infinite-Cutoff Renormalization of the Chiral NucleonNucleon Interaction up to N<sup>3</sup>LO

DOI 10.1007/s00601-012-0481-4, Springer, arXiv: 1208.2657.

## CONFERENCE CONTRIBUTIONS

R. Machleidt, Q. MacPherson, E. Marji, R. Winzer, Ch. Zeoli, D. R. Entem  
Recent Progress in the Theory of Nuclear Forces  
Few-Body Systems, Vol. 54, No. 7, pp 821-826, August 2013, arXiv:1210.0992v1

R. Machleidt, E. Marji, and Ch. Zeoli,  
Finite-cutoff renormalization of the chiral NN potential,  
2011 April Meeting of the American Physical Society,  
Anaheim, California, April 30 - May 3, 2011,  
Bull. Am. Phys. Soc. Vol. 56, No. 4, 100 (2011).

R. Machleidt, E. Marji, and Ch. Zeoli,  
The nuclear force problem: Have we finally reached the end of the tunnel?,  
Proc. 474th WE-Heraeus-Seminar on “Strong Interactions: From Methods to Structures”,  
Physikzentrum Bad Honnef (Germany), February 2011, arXiv:1104.0847.

R. Machleidt and Ch. Zeoli,  
Infinite-cutoff renormalization of the chiral NN potential up to N<sup>3</sup>LO,  
2010 Fall Meeting of the APS Division of Nuclear Physics,  
Santa Fe, New Mexico, November 2010,  
Bull. Am. Phys. Soc. Vol. 55, No. 14, 128 (2010).

## MILITARY SERVICE

Idaho Army National Guard, Moscow, ID (Jun 2003 Jun 2009)  
Veteran, Sergeant Honorably discharged as a Veteran and Non-Commissioned Officer, Sergeant,  
of the Idaho Army National Guard. Held a high-level security clearance while serving in combat  
under the Plans & Operations Section of the 116th Engineer Battalion during Operation Iraqi  
Freedom III. Lead, directed, supervised, and trained lower enlisted soldiers during time of service.